SunFesT

(www.seas.upenn.edu/~sunfest)

2010

SUMMER UNDERGRADUATE FELLOWSHIPS IN SENSOR TECHNOLOGIES

TECHNICAL REPORT
TR-CST 27AUG 2010
Center for Sensor Technologies
University of Pennsylvania
Philadelphia, PA 19104

Acknowledgement

This material is based upon work supported by the National Science Foundation under Grant No. 0754741.

Disclaimer

Any opinions, findings, and conclusions or recommendations expressed in this material are those of the author(s) and do not necessarily reflect the views of the National Science Foundation.

SUNFEST 2010

SUNFEST 2010

SUMMER UNDERGRADUATE FELLOWSHIP IN SENSOR TECHNOLOGIES
Sponsored by the National Science Foundation (Award no. EEC-0754741)

From June 1 through August 7, 2010 eleven students from Penn and other colleges participated in the SUNFEST program, which is organized by the Center for Sensor Technologies of the School of Engineering and Applied Science at the University of Pennsylvania. This unique "Summer Experience for Undergraduates in Sensor Technologies" program was initiated in 1986 and has grown considerably in size. It is now recognized as one of the most successful summer programs for undergraduates in the country. I would like to express my sincere gratitude to the National Science Foundation for their continued support since 1987 for this REU Site.

The purpose of the SUNFEST program is to provide bright, motivated undergraduate students with the opportunity to become involved in active research projects under the supervision of a faculty member and his graduate student(s). The general area of research concentrates on sensor technologies and includes projects such as materials and technology for sensors, nanotechnology and microstructures, smart imagers, sensors for biomedical applications and robotics. By providing the students with hands-on experience and integrating them with a larger research group where they can work together with other students, the program intends to guide them in their career choices. By exposing the students to the world of research, we hope they will be more inclined to go on for advanced degrees in science and engineering, as many have done.

The students participated in a variety of hands-on workshops in order to give them the tools to do first-rate research or enhance their communication skills. These included "Ethics in Science and Engineering", "Information Retrieval and Evaluation", "Applying to Graduate School", "Giving Presentations", and "Writing Technical Reports". Students also had plenty of opportunity for social interactions among themselves or with faculty and graduate student advisors.

For the first time this year a group of judges selected the top project and two honorable mentions. The projects were selected based on the technical quality of the results, the quality of the slides and presentation, and answering questions. The choices were very hard since all projects were first rate. The first prize went to Brian Helfer (University of Connecticut) for his the project "Characterization and Design of Organic Field-Effect Transistor Circuits for Sensing Bioelectromagnetism." The two honorable mentions went to Nathalia Garcia-Acosta (Temple University) for her project on "Nanoelectronic Sensor for Detection of Prostate Cancer Biomarkers"; and to Logan Osgood-Jacobs (Swarthmore College) for her project on "Pediatric Dynamometer Using Piezoresistance Sensor."

This booklet contains reports from this year's projects, the quality of which testifies to the high level of research and commitment by these students and their supervisors. I would like to express my sincere thanks to the students for their enthusiastic participation; the help of the faculty members, graduate students and support staff is very much appreciated. I would also like to thank Necole Rasul, Sherri Butler, Valerie Lundy-Wagner, Sid Deliwala, and the rest of the ESE staff for their invaluable help in making this program run smoothly.

Jan Van der Spiegel, Director
Center for Sensor Technologies

FINAL REPORT

2010 SUMMER UNDERGRADUATE FELLOWSHIP
IN SENSOR TECHNOLOGIES
Sponsored by the National Science Foundation

http://www.ese.upenn.edu/~sunfest/pastProjects/Projects10.html

TABLE OF CONTENTS

LIST OF STUDENT PARTICIPANTS
IN THE SUNFEST PROGRAM SINCE 1986

Summer 2010

Noah Tovares	Occidental College
Nathalia Garcia Acosta	Temple University
Sarena Horava	University of Massachusetts Amherst
Brett Kuprel	University of Michigan
Logan Osgood-Jacobs	Swarthmore College
Sriram Radkrishnan	University of Pennsylvania
Johary Rivera	University of Puerto Rico, Río Piedras Campus
Jennifer L. Smith	North Carolina State University
Jason C. Carter	Morgan State University
Carlos Torres Casiano	University of Puerto Rico, at Mayagüez
Brian Helfer	University of Connecticut

Summer 2009

Bink Hank	Lafayette College
Connolly Allison	Johns Hopkin
Dupree Phillip	Columbia University
Gerasimowicz Katherine	University of Pennsylvania
Gonzalez Willie	Univ. of Puerto Rico, Mayaguez
Koehler Sarah	Cornell University
Mclaughlin Linda	Community College of Philadelphia
Narkeviciute Ieva	Univ. of Massachusetts Amherst
Perreira Jeffrey	Lehigh University
Townley Andrew	University of Pennsylvania
Velazquez Desiree	Univ. of Puerto Rico at Humacao)
Walters Valerie	Virginia Polytechnic Institute and State University

Summer, 2008

Clarence Agbi	Yale University
Uchenna Anyanwu	San Jose State University
Christopher Baldassano	Princeton University
Alta Berger	George Washington University
Ramon Luis Figueroa	University of Puerto Rico
David Joffe	Carnegie Mellon University
Erika Martinez	University of Puerto Rico
Alexei Matyushov	Arizona State University
Kamruzzaman Rony	Stony Brook University

Anil Venkatesh	University of Pennsylvania
Emily Wible	University of Pennsylvania

Summer, 2007

Mulutsga Bereketab	Virginia Polytechnic Institute
Sonia A. Bhaskar	Princeton University
Patrick Duggan	Providence College
Nataliya Kilevskaya	University of Florida
Ryan Li	Case Western Reserve University
Viktor L. Orekhov	Tennessee Technological University
Andrew Potter	Brown University
Pamela Tsing	University of Pennsylvania
Victor Uriarte	Florida International University
Adriane Wotawa-Bergen	University at Buffalo
Arelys Rosado Gomez	University of Puerto Rico

Summer, 2006

Sam Burden	University of Washington
Jose M. Castillo Colon	University of Puerto Rico Alexsandra
Fridshtand	Lehigh University
Shakera Guess	Lincoln University
Journee Isip	Columbia University
Nathan Lazarus	University of Pennsylvania
Armand O'Donnell	University of Pennsylvania
William Peeples	Lincoln University
Raúl Pérez Martínez	University of Puerto Rico
Helen Schwerdt	Johns Hopkins University
Xiaoning Yuan	Duke University

Summer, 2005

Robert Callan	University of Pennsylvania
David Cohen	University of Pennsylvania
Louie Huang	University of Pennsylvania
Roman Geykhman	University of Pennsylvania
An Nguyen	University of Pennsylvania
Olga Paley	University of California at Berkeley
Miguel Perez Tolentino	University of Puerto Rico
Ebenge Usip	University of Southern California
Adam Wang	University of Texas, Austin
Kejia Wu	University of Pennsylvania

Summer, 2004

Benjamin Bau	Massachusetts Institute of
TechnologyAlexander H. Chang	University of Pennsylvania
Seth Charlip-Blumlein	University of Pennsylvania
Ling Dong	University of Rochester
David Jamison	Johns Hopkins University
Dominique Low	University of Pennsylvania
Emmanuel U. Onyegam	University of Texas, Dallas
J. Miguel Ortigosa	Florida Atlantic University
William Rivera	University of Puerto Rico, Mayaguez
Matthew Sauceda	Texas A&M University, Kingsville
Olivia Tsai	Carnegie Mellon University

Summer, 2003

Emily Blem	Swarthmore College
Brian Corwin	University of Pennsylvania
Vinayak Deshpande	University of Virginia
Nicole DiLello	Princeton University
Jennifer Geinzer	University of Pittsburgh
Jonathan Goulet	University of Pennsylvania
Mpitulo Kala-Lufulwabo	University of Pittsburgh
Emery Ku	Swarthmore College
Greg Kuperman	University of Pennsylvania
Linda Lamptey	University of Pennsylvania
Prasheel Lillaney	University of Pennsylvania
Enrique Rojas	University of Pennsylvania

Summer, 2002

Christopher Bremer	Colorado School of Mines
Aslan Ettehadien	Morgan State University
April Harper	Hampton University
Catherine Lachance	University of Pennsylvania
Adrian Lau	University of Pennsylvania
Cynthia Moreno	University of Miami
Yao Hua Ooi	University of Pennsylvania
Amber Sallerson	University of Maryland/Baltimore
Jiong Shen	University of California-Berkeley
Kamela Watson	Cornell University
John Zelena	Wilkes University

Summer, 2001

Gregory Barlow	North Carolina State University
Yale Chang	University of Pennsylvania
Luo Chen	University of Rochester
Karla Conn	University of Kentucky
Charisma Edwards	Clark Atlanta University
EunSik Kim	University of Pennsylvania
Mary Kutteruf	Bryn Mawr College
Vito Sabella	University of Pennsylvania
William Sacks	Williams College
Santiago Serrano	Drexel University
Kiran Thadani	University of Pennsylvania
Dorci Lee Torres	University of Puerto Rico

Summer, 2000

Lauren Berryman	University of Pennsylvania
Salme DeAnna Burns	University of Pennsylvania
Frederick Diaz	University of Pennsylvania (AMPS)
Hector Dimas	University of Pennsylvania (AMPS)
Xiomara Feliciano	University of Turabo (Puerto Rico)
Jason Gillman	University of Pennsylvania
Tamara Knutsen	Harvard University
Heather Marandola	Swarthmore College
Charlotte Martinez	University of Pennsylvania
Julie Neiling	University of Evansville, Indiana
Shiva Portonova	University of Pennsylvania

Summer, 1999

David Auerbach	Swarthmore College
Darnel Degand	University of Pennsylvania
Hector E. Dimas	University of Pennsylvania
Ian Gelfand	University of Pennsylvania
Jason Gillman	University of Pennsylvania
Jolymar Gonzalez	University of Puerto Rico
Kapil Kedia	University of Pennsylvania
Patrick Lu	Princeton University
Catherine Reynoso	Hampton University
Philip Schwartz	University of Pennsylvania

Summer, 1998

Tarem Ozair Ahmed	Middlebury University
Jeffrey Berman	University of Pennsylvania

Alexis Diaz	Turabo University, Puerto Rico
Clara E. Dimas	University of Pennsylvania
David Friedman	University of Pennsylvania
Christin Lundgren	Bucknell University
Heather Anne Lynch	Villanova University
Sancho Pinto	University of Pennsylvania
Andrew Utada	Emory University
Edain (Eddie) Velazquez	University of Pennsylvania

Summer, 1997

Francis Chew	University of Pennsylvania
Gavin Haentjens	University of Pennsylvania
Ali Hussain	University of Pennsylvania
Timothy Moulton	University of Pennsylvania
Joseph Murray	Oklahoma University
O'Neil Palmer	University of Pennsylvania
Kelum Pinnaduwage	University of Pennsylvania
John Rieffel	Swarthmore College
Juan Carlos Saez	University of Puerto Rico, Cayey

Summer, 1996

Rachel Branson	Lincoln University
Corinne Bright	Swarthmore College
Alison Davis	Harvard University
Rachel Green	Lincoln University
George Koch	University of Pennsylvania
Sandro Molina	University of Puerto Rico-Cayey
Brian Tyrrell	University of Pennsylvania
Joshua Vatsky	University of Pennsylvania
Eric Ward	Lincoln University

Summer, 1995

Maya Lynne Avent	Lincoln University
Tyson S. Clark	Utah State University
Ryan Peter Di Sabella	University of Pittsburgh
Osvaldo L. Figueroa	University of Puerto Rico-Humacao
Colleen P. Halfpenny	Georgetown University
Brandeis Marquette	Johns Hopkins
Andreas Olofsson	University of Pennsylvania
Benjamin A. Santos	University of Puerto Rico-Mayaguez
Kwame Ulmer	Lincoln University

Summer, 1994

Alyssa Apsel	Swarthmore College
Everton Gibson	Temple University
Jennifer Healy-McKinney	Widener University
Peter Jacobs	Swarthmore College
Sang Yoon Lee	University of Pennsylvania
Paul Longo	University of Pennsylvania
Laura Sivitz	Bryn Mawr College
Zachary Walton	Harvard University

Summer, 1993

Adam Cole	Swarthmore College
James Collins	University of Pennsylvania
Brandon Collings	Hamilton University
Alex Garcia	University of Puerto Rico
Todd Kerner	Haverford College
Naomi Takahashi	University of Pennsylvania
Christopher Rothey	University of Pennsylvania
Michael Thompson	University of Pennsylvania
Kara Ko	University of Pennsylvania
David Williams	Cornell University
Vassil Shtonov	University of Pennsylvania

Summer, 1992

James Collins	University of Pennsylvania
Tabbetha Dobbins	Lincoln University
Robert G. Hathaway	University of Pennsylvania
Jason Kinner	University of Pennsylvania
Brenelly Lozada	University of Puerto Rico
P. Mark Montana	University of Pennsylvania
Dominic Napolitano	University of Pennsylvania
Marie Rocelie Santiago	Cayey University College

Summer, 1991

Gwendolyn Baretto	Swarthmore College
Jaimie Castro	University of Puerto Rico
James Collins	University of Pennsylvania
Philip Chen	University of Pennsylvania
Sanath Fernando	University of Pennsylvania
Zaven Kalayjian	University of Pennsylvania
Patrick Montana	University of Pennsylvania

Mahesh Prakriya	Temple University
Sean Slepner	University of Pennsylvania
Min Xiao	University of Pennsylvania

Summer, 1990

Angel Diaz	University of Puerto Rico
David Feenan	University of Pennsylvana
Jacques Ip Yam	University of Pennsylvania
Zaven Kalayjian	University of Pennsylvania
Jill Kawalec	University of Pennsylvania
Karl Kennedy	Geneva
Jinsoo Kim	University of Pennsylvania
Colleen McCloskey	Temple University
Faisal Mian	University of Pennsylvania
Elizabeth Penadés	University of Pennsylvania

Summer, 1989

Peter Kinget	Katholiek University of Leuven
Chris Gerdes	University of Pennsylvania
Zuhair Khan	University of Pennsylvania
Reuven Meth	Temple
Steven Powell	University of Pennsylvania
Aldo Salzberg	University of Puerto Rico
Ari M. Solow	University of Maryland
Arel Weisberg	University of Pennsylvania
Jane Xin	University of Pennsylvania

Summer, 1988

Lixin Cao	University of Pennsylvania
Adnan Choudhury	University of Pennsylvania
D. Alicea-Rosario	University of Puerto Rico
Chris Donham	University of Pennsylvania
Angela Lee	University of Pennsylvania
Donald Smith	Geneva
Tracey Wolfsdorf	Northwestern University
Chai Wah Wu	Lehigh University
Lisa Jones	University of Pennsylvania

Summer, 1987

Salman Ahsan	University of Pennsylvania
Joseph Dao	University of Pennsylvania
Frank DiMeo	University of Pennsylvania
Brian Fletcher	University of Pennsylvania
Marc Loinaz	University of Pennsylvania
Rudy Rivera	University of Puerto Rico
Wolfram Urbanek	University of Pennsylvania
Philip Avelino	University of Pennsylvania
Lisa Jones	University of Pennsylvania

Summer, 1986

Lisa Yost	University of Pennsylvania
Greg Kreider	University of Pennsylvania
Mark Helsel	University of Pennsylvania

Reducing Anchor Loss in AlN Contour Mode Resonators

NSF Summer Undergraduate Fellowship in Sensor Technologies
Noah Tovares (Physics) – Occidental College
Advisor: Gianluca Piazza

Abstract

Many researchers have devoted money and effort toward developing of MEMS resonators. Much of this effort has been devoted to increasing the quality factor, a measure of the energy lost by the resonator. Fabricating new resonators for testing is costly and time consuming. Methods for accurately simulating the quality factor of MEMS resonators would increase development efficiency. By design, the resonator body is attached to the substrate via tethers. Due to the immense size of the substrate with respect to the resonator, any energy traveling from the resonator to the substrate is lost. In order to accurately simulate the resonator it is necessary to have a semi-infinite domain that behaves like the substrate. The perfectly matched layer (PML) feature of COMSOL FEM software serves as an artificial medium: surrounding the smaller simulation-substrate and absorbing any radiation escaping from the resonator. Before resonator designs can be simulated, though, it must be confirmed that the PML does not affect the quality factor or resonant frequency of the resonator. In order to determine the conditions for accurate simulations a resonator is modeled in COMSOL and simulations are performed while varying the PML width, maximum mesh element size in the PML sub-domain, substrate size, maximum mesh element size in the substrate sub-domain, and tether location. The quality factor is determined by calculating the admittance and using 3dB bandwidth. The predicted results are that the quality factor will decrease with mesh density and will converge around 5-micron mesh size. These results will allow accurate simulation of tether designs meant to reduce anchor loss, the biggest problem facing the development of MEMS resonators.

1. Introduction

Microscale devices have become a major trend in the consumer electronics market. In order for devices to become smaller, though, their components must also become smaller and more integrated. This has propelled many researchers to focus their efforts on developing microelectromechanical systems (MEMS). MEMS can be used, for example, to make mechanical switches, resonators, accelerometers, and sensors. Their compact size leads to many advantages such as system-on-a-chip (SoC) and power efficiency. These advantages are especially important when dealing with MEMS resonators for RF filters applications.

MEMS resonators for RF filters applications are implemented as band pass filters, and allow signals of selected frequencies to be transmitted and received. Recently a novel type of RF MEMS filter has emerged with many advantages over competing technologies. This paper focuses on the aluminum nitride (AlN) piezoelectric contour-mode (CM) MEMS resonators [1] for RF filter applications introduced by Piazza in his paper, Piezoelectric Aluminum Nitride Vibrating Contour-Mode MEMS Resonators.

The AlN CM resonator consists of an AlN film sandwiched between metal fingers. This geometry utilizes the lateral piezoelectric coefficient (d_{31}) to generate a horizontal displacement when an electric field is applied in the vertical direction. The resonant frequency is determined by the width of each finger, allowing for an array of resonators each with a different resonant frequency on one chip. In a world where mobile phones require at least four modes of wireless communication, an all-inclusive on chip solutions is very appealing.

Before AlN CM MEMS Resonators can be implemented, though, a few hurdles must be overcome, the most pressing of which is the improvement of the quality factor: a measure of the energy lost by the resonator. There are several mechanisms that can be responsible for the energy loss. Amongst them, the most important are air damping, thermo-elastic dissipation, material loss, phonon-phonon interactions, and anchor loss. Anchor loss, the escape of energy via the tether, is likely to be the dominant energy loss mechanism [2] in AlN CM resonators.

This paper examines the reduction of anchor loss in AlN CM resonators by simulating novel designs in COMSOL® finite element method (FEM) software and analyzing the quality factor and frequency response of the resonator. A significant portion of this work will be devoted to the determining the how COMSOL's parameters affect the simulations of the resonators.

2. Background

2.1 Piezoelectric MEMS Resonators for RF filter applications

Piezoelectricity, discovered in the 1880's by the Curie brothers, describes the behavior of crystals belonging to certain classes. Piezoelectric materials have the unique property whereby mechanical strain in the crystals induces electric polarization. Conversely, piezoelectric materials exposed to an electric field will be subject to mechanical strain.

Piezoelectric MEMS resonators for RF filter applications are implemented as band pass filters to allow signals of selected frequencies to be transmitted and received. These devices work by exploiting the reverse piezoelectric effect. The MEMS resonator is designed to resonate at a certain resonant frequency and have a certain impedance by properly dimensioning its geometrical parameters. When the resonator is exposed to a signal at the resonant frequency it amplifies its vibrations [5]. These vibrations induce the reverse piezoelectric effect and an electric potential arises across the piezoelectric material. The electrodes placed on the resonators are subject to the induced electric potential, allowing the routing of the signal to the external circuitries.

2.2 AlN Contour-Mode MEMS Resonators

The AlN vibrating Contour-Mode MEMS resonators introduced by Piazza *et al.* have great potential to become a widely implemented technology [1]. The PMANS lab at the University of Pennsylvania, under the direction of Professor Gianluca Piazza, has done much work developing AlN vibrating Contour-Mode resonators [9]. This sections outlines the previous work done by Piazza.

2.2.1 Introduction

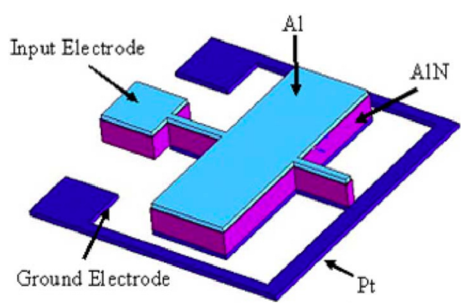

Figure 1 – Rectangular AlN Resonator with Al and Pt Electrodes

The current designs being tested are rectangular plate and ring (circular and square) resonators. A Pt electrode on bottom and an Al electrode on top surround the resonator's AlN body [1]. The physical dimensions (lateral features) of the resonator determine the resonant frequency. For further analysis Piazza *et al.* derived the equivalent electromechanical parameters.

2.2.2 Frequency Settings

While the in-plane dimensions have the greatest effect on the resonant frequency electrode thickness, sidewall angle, and anchor size also have an effect. When high-density materials are being used the electrode thickness becomes an issue, lowering the resonant frequency significantly. The effect of sidewall angle becomes significant when the difference between the size of the top and bottom portions of the resonators are on the order of one wavelength of the resonant frequency. The effect of temperature is considered negligible in AlN resonators.

2.2.3 Experimental Results

The quality factors of the rectangular and ring resonators were calculated by dividing the center frequency by the 3dB bandwidth. For rectangular plate resonators [1] it was found that an aspect ratio of 4:1 resulted in higher quality factors. This previous work also obtained Q's between 2000 and 3000 for the rectangular resonators at standard temperature and pressure (STP). For ring resonators notched supports were introduced in several structures in an attempt to reduce anchor interference, but were found to have little effect on the quality factor. The highest Q of 2900 was recorded for a circular ring resonator at 472.7 MHz.

2.2.4 Quality Factor

The quality factor is defined by the equation

$$Q = \frac{2\pi \cdot \text{EnergyStoredPerCycle}}{\text{EnergyLostPerCycle}} \quad (3)$$

In order to maximize the quality factor energy loss must be minimized. Air damping, thermo-elastic dissipation, phonon-phonon interactions, material loss, and anchor loss have all been identified as energy loss mechanisms [2]. Piazza examined these mechanisms and determined that anchor size, material losses in the electrodes, and trapping energy in the resonators were worth investigating.

2.3 Anchor Loss

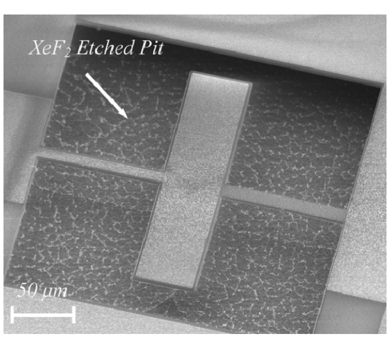

Figure 2 – SEM of AlN Rectangular Resonator [1]

Anchor loss describes the escape of energy from the resonator to the substrate through the anchor. Because there is no acoustic mismatch between the resonator body and the substrate, acoustic waves that travel to the substrate via the tether are considered lost energy. In order to improve the quality factor of the resonators this energy must not be allowed to go into the substrate. This paper describes some of the current methods being tested in the PMANS lab as an effort to reduce anchor loss.

2.4 COMSOL Finite Element Method and Perfectly Matched Layers

COMSOL (Finite Element Method) software was utilized to perform the simulations in the following sections. The AlN CM resonator was modeled and studied using the piezo-solid model. In order to more accurately simulate the energy lost via the tether a perfectly matched layer (PML) is employed. The PML, in the solid stress-strain module, serves as an artificial medium designed to absorb all incoming radiation. The main goal of these simulations is to explore PML parameters and determine how each of them affects the quality factor of the resonator under test.

3. Novel Designs for Reducing Anchor Loss in AlN Contour-Mode Resonators

The tether has been identified as the conduit through which the majority of energy escapes from the resonator. Knowing this, several parameters were investigated in order to explore whether the design of the tether can be manipulated in order to minimize energy loss. First, the width of the tether is fixed and the length is varied. Next, the length is fixed and the width is varied. Lastly, both the length and width are fixed and “branching” is explored. Tethers with one and two branches are explored. Figures 3 through 5 show the different branch models.

Figure 3 – Single tether design

Figure 4 – Single branch design

Figure 5 – Double branch design

These designs, being investigated by Songbin Gong [8], utilize transmission line modeling and impedance matching to maximize the wave reflection and minimize energy loss.

When the tethers are thin enough their behavior can be compared to that of a transmission line. A transmission line is a medium that directs the flow of energy. The transmission line model allows for the use of impedance matching.

Impedance, a term most commonly used when discussing electronics, is often thought of as the AC equivalent of resistance. When designing electronics it is essential to match impedances in order to maximize the transfer of power between components and minimize the reflections from the source. In the case of our MEMS resonators, though, it is ideal to minimize the transfer of power between the tether and the substrate and maximize the reflection from the source. This is accomplished by creating a mismatch between the impedances of the body, tether, and substrate. For our purposes, the parameter that affects the impedance is the cross-section area of the tether.

$$Z = A\sqrt{E\rho} \quad (4)$$

Equation 4 says that Z, the impedance, is equal to the cross-sectional area of the wire multiplied by the square root of the product of the wire's young's modulus and density.

Figure 6 shows a stepped transmission line. In this model there are three segments that each have an impedance mismatch with the segment(s) next to it.

(a)

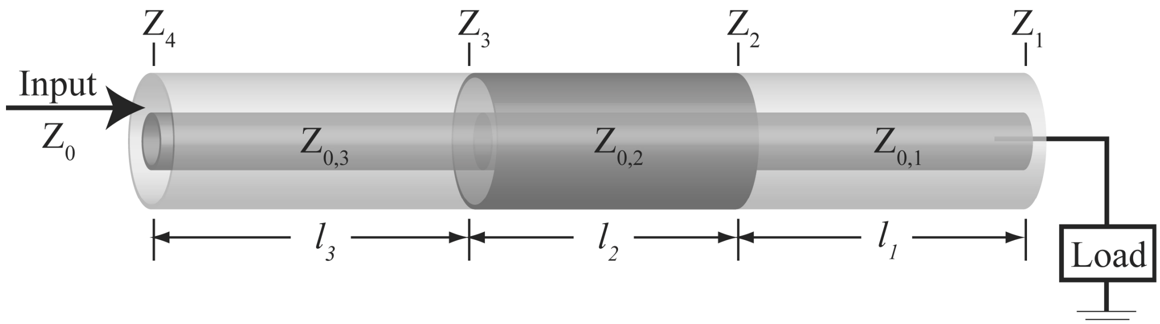

Figure 6 – Stepped transmission line

4. Methods

The use of COMSOL's PML feature is essential to the accurate simulation of resonators. When testing actual resonators, any energy that escapes through the tether into the silicon substrate is considered lost. The silicon substrate is so large in comparison to the resonators that it is essentially an infinite domain. When simulating resonator results, though, it is impossible to have an infinite domain. When used with the correct parameters, the PML acts as an infinite domain: fully absorbing radiation from any angle.

In order to determine the ideal situation for the simulations several parameters will be investigated. The effect of the PML mesh-density, substrate mesh-density, PML size, substrate size, and tether location on the quality factor is yet unknown.

The base model used for these simulations is a three finger inter-digitated resonator with finger widths of 20 microns. The width of the fingers determines the wavelength to be 40 microns. The tether width and height are 2 microns and the length is 10 microns. The silicon substrate is a 40 micronx40micronx40micron cube, surrounded on 4 sides by the PML of 20 micron width. The PML used in these simulations utilizes a Cartesian coordinate system. The model uses planar symmetry in order to reduce the number of mesh elements. Once the simulation is completed, the admittance is calculated using equation 5 and the quality factor is determined by utilizing the 3dB bandwidth.

$$20 * \log 10(abs(I / V)) \quad (5)$$

The following sections outline the various parameters being investigated.

5. Methods and Results

After each simulation was performed the data was exported in a text file and imported into Origin. The resonant frequency was determined and the quality factor calculated by using the 3db bandwidth. Graphs were made of the frequency response and quality factor.

5.1 PML Width Simulations

PML width is varied between 5 and 40 microns, while all other parameters kept constant. Maximum mesh element size is kept constant at 10 microns. This set of simulations was performed once for a tether width of 2 micron and once for a tether width of 5 micron.

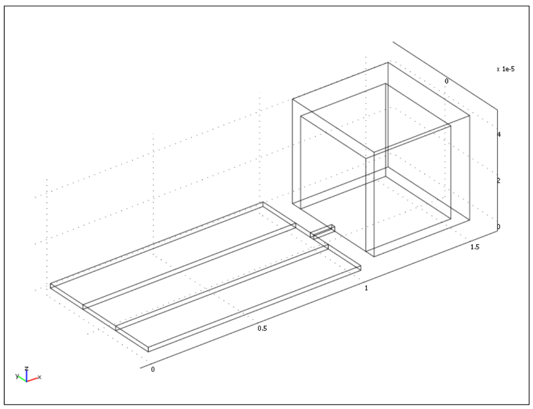

Figure 7 – PML Width of 5 Micron

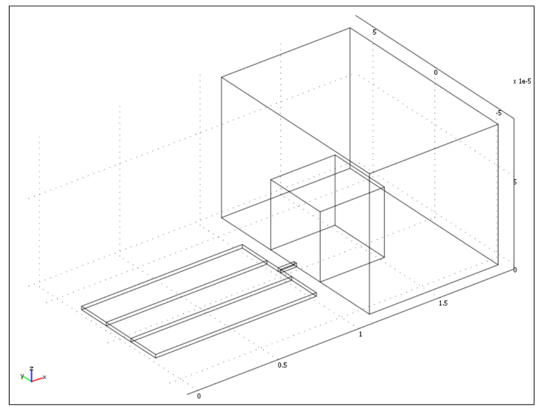

Figure 8 – PML Width of 40 Micron

5.1.1 PML Width Simulation Results (5 Micron Tether width)

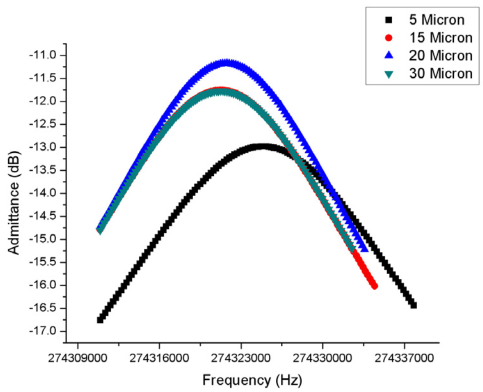

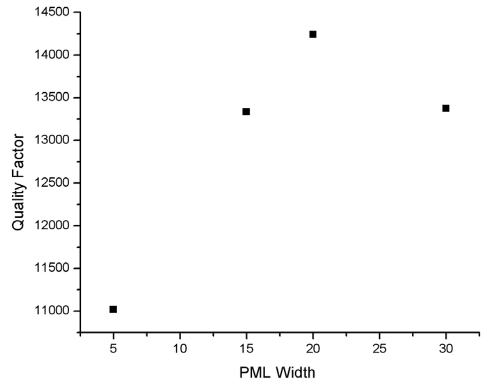

Figure 9 – Frequency Response for various PML widths

Figure 10 – Quality Factor vs. PML width

Figure 9 shows the frequency response of the resonators as the PML width is varied. The quality factor does not seem to depend on the PML width. The average quality factor is 12991.1 with a standard deviation of 1379.9.

5.1.2 PML Width Simulation Results (2 Micron Tether Width)

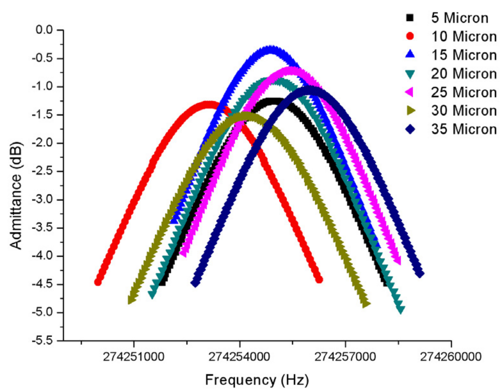

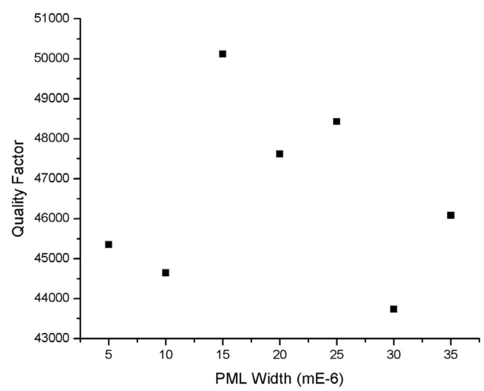

Figure 11 – Frequency Response for various PML Mesh Densities

Figure 12 – Quality Factor vs. PML width

The previous simulations were repeated with a tether width of 2 microns. The average quality factor was 46563.2 with a standard deviation of 2260.9. The quality factor is affected little by the PML width.

5.2 PML Sub-domain Mesh Density Simulations

The only parameter being changed is the maximum mesh element size in the PML sub-domain. The smaller the maximum mesh element size the denser the mesh will be. This maximum mesh element size is varied from 6 microns to 15 microns.

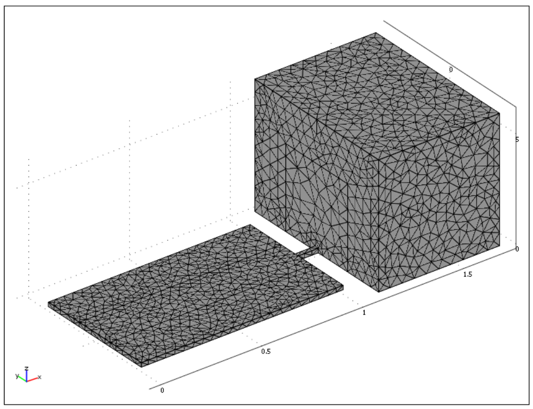

Figure 13 – PML Mesh Size of 6 Micron

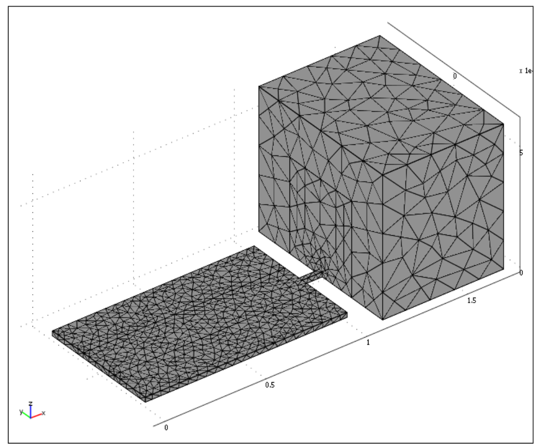

Figure 14 – PML Mesh Size of 15 Micron

5.2.1 PML Sub-domain Mesh Density Simulation Results

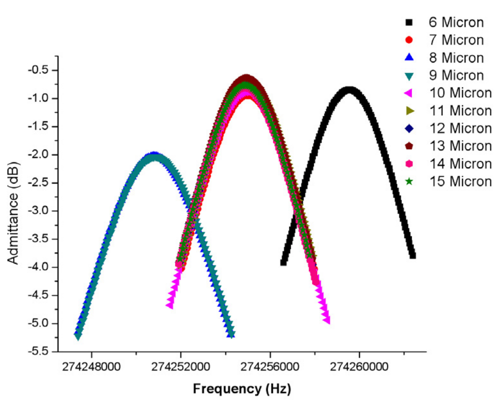

Figure 15– Frequency Response for various Max Mesh Element Sizes

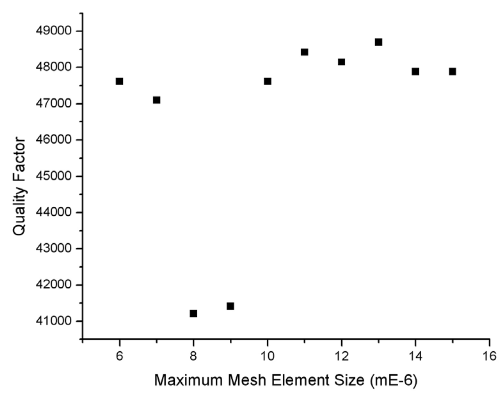

Figure 16 – Quality Factor vs. Max Mesh Element Size

The average quality factor was 46594.9 with a standard deviation of 2824.7. This deviation leads to the conclusion that the quality factor is not greatly affected by the mesh density in the PML sub-domain.

5.3 Substrate Size Simulations

The substrate size is varied from 10 micron^3 to 40 micron^3 while the PML width is kept constant at 20 microns.

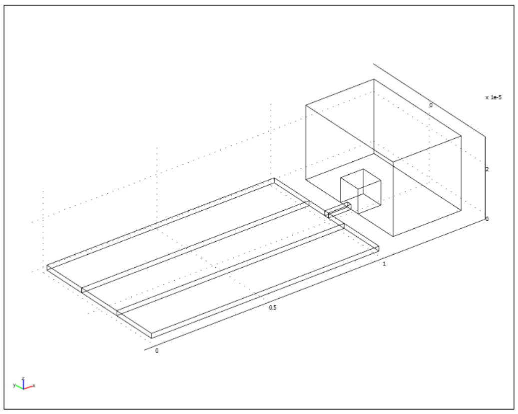

Figure 17 – Substrate Size of 10^3 microns

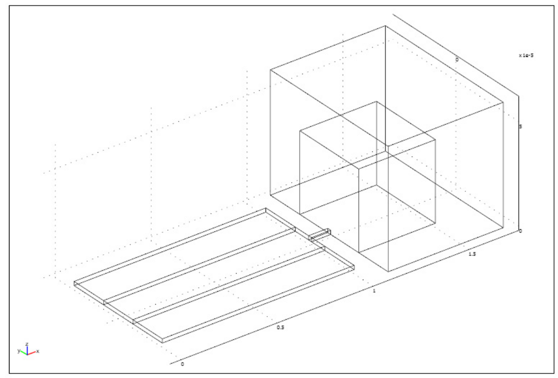

Figure 18 – Substrate Size of 40^3 microns

5.3.1 Substrate Size Simulation Results

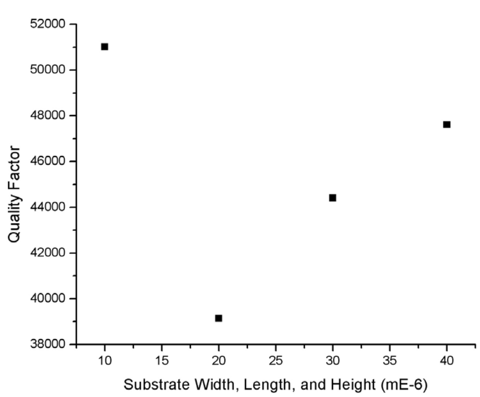

Figure 19– Quality Factor vs. Substrate Size (Max Mesh element Size of 10 in PML and Substrate)

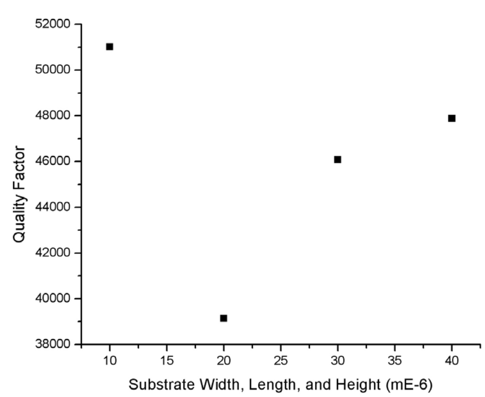

Figure 20– Quality Factor vs. Substrate Size (Max Mesh element Size of 15 in PML and Substrate)

For the simulation with the maximum mesh element size of 10 micron the average quality factor was 45542.1 with a standard deviation of 5052.0. For the simulation with the maximum mesh element size of 15 micron the average quality factor was 46026.4 with a standard deviation of 5026.5. Although the standard deviations were slightly higher in this case they do not indicate a significant dependence of the quality factor on substrate size.

5.4 Substrate Sub-domain Mesh Density

This maximum mesh element size in the substrate sub-domain is varied from 5 microns to 10 microns while all other parameters are held constant.

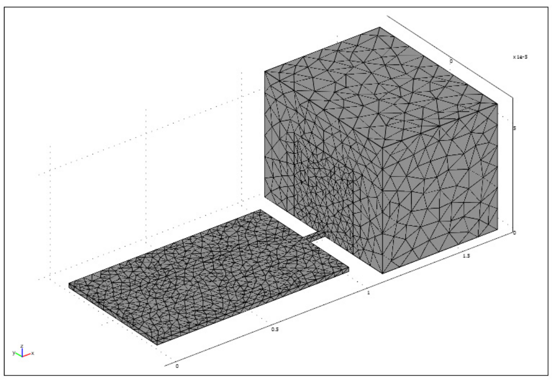

Figure 21 – Substrate Mesh Size of 5 Micron

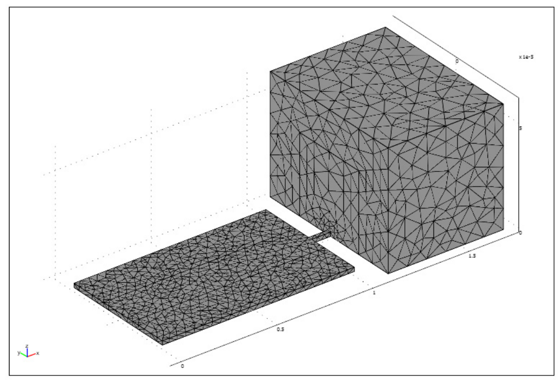

Figure 22 – Substrate Mesh Size of 10 Micron

5.4.1 Substrate Sub-domain Mesh Density Simulation Results

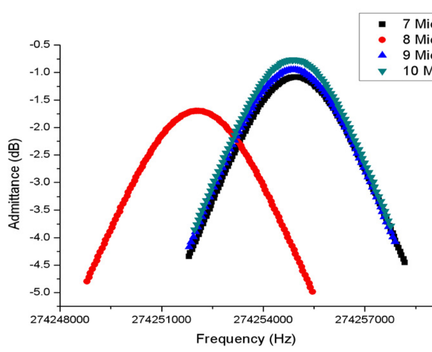

Figure 23– Frequency Response for various Max Mesh Element Sizes

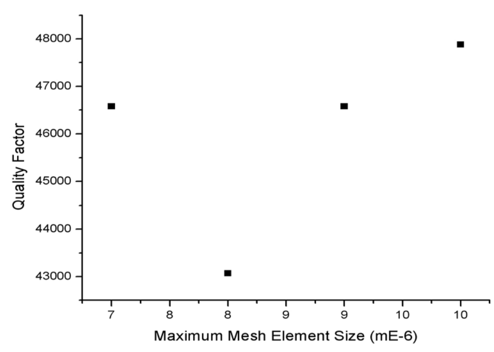

Figure 24 – Quality Factor vs. Max Mesh Element Size

The average quality factor was 46026.0 with a standard deviation of 2065.7. This low deviation leads to the conclusion that the mesh density in the substrate sub-domain does not greatly affect the quality factor.

5.5 Tether location

First the PML is removed, but the tether is not moved. A second simulation is done with the tether moved to the center of the PML. Although the second simulation represents a physically impossible situation it is nonetheless interesting.

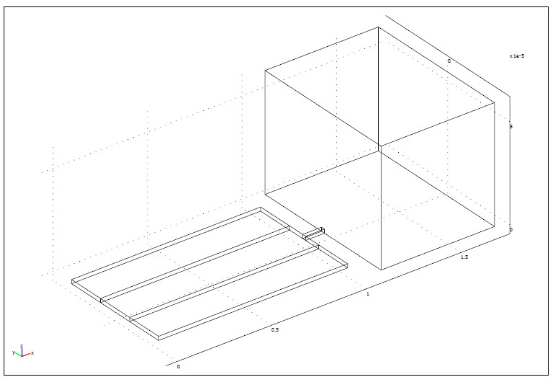

Figure 25 – Tether Attached Directly to PML

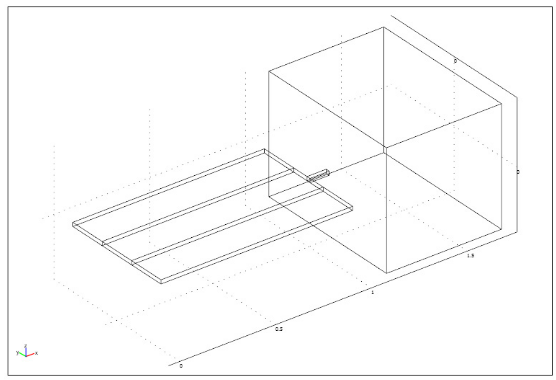

Figure 26 – Tether Attached Directly to PML at Midpoint

5.5.1 Tether Locations Simulation Results

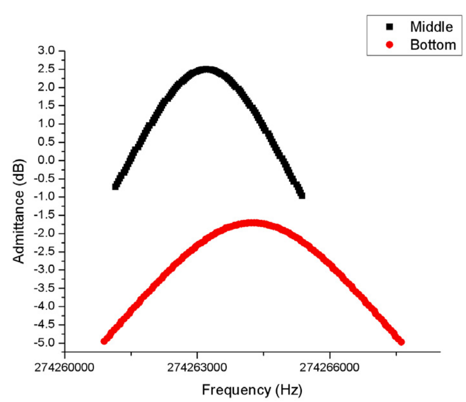

Figure 27 – Frequency Response for Alternate Tether Locations

When removing the substrate, but keeping the tether in the usual position the quality factor was found to be 42853. With the substrate of size 40^3 microns the quality factor was found to be 47613. When removing the substrate and moving the tether to the middle of the PML sub-domain the quality factor was found to be 70251. The difference between the two quality factors is 27,398. The resonant frequency also shifted, but the difference was negligible.

5.6 Tether Lengths and Widths

The base model was modified to examine the effect of the tether on the quality factor. Tether lengths of 1/8 λ, 1/4 λ, and 3/8 λ were explored along with tether widths of 2 and 5 microns.

5.6.1 Tether Lengths and Widths Simulation Results

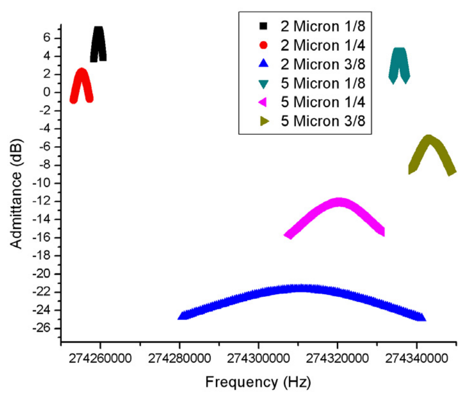

Figure 28 – Frequency Response for Various Tether Widths and Lengths

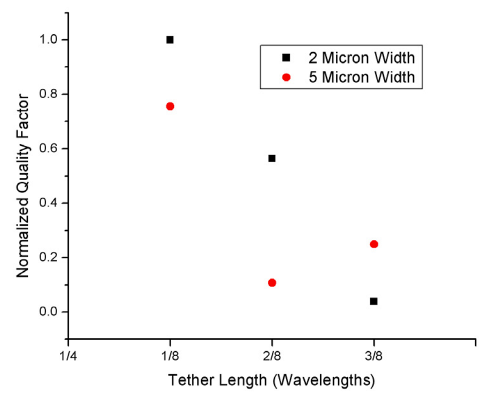

Figure 29 – Quality Factors for Various Tether Widths and Lengths

For the 1/8 and 1/4 wavelength tethers, there was a significant drop in the quality factor when moving from the 2 micron wide tether to the 5 micron wide tether. This was expected as more energy is able to escape from the resonator when the tether is wider.

For the 3/8 wavelength tether there was in increase in the quality factor when moving from the 2 micron wide tether to the 5 micron wide tether. The reason behind this is unknown and should be explored in future research.

5.7 Novel tether designs

The branch designs outlined in section 3 were tested using tether widths of 2 and five microns. The branches were all designed to be quarter λ and in order to ensure that the branches were of the current length their length was measured from the middle of the main tether. For the 2 micron tether width simulations the branches were 9 microns long, and for the 5 micron tether width simulations the branches were 7.5 microns long.

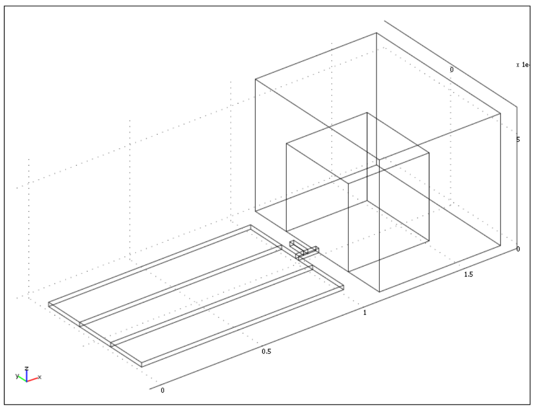

Figure 30 – One-branch Design for 2 Micron Tether Width

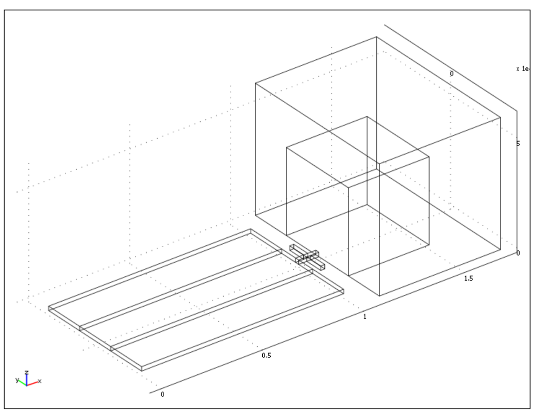

Figure 31 – Two-branch Design for 2 Micron Tether Width

5.7.1 Novel Tether Design Simulation Results

Due to time constraints simulations of the novel tether designs were not completed.

6. Discussions and Conclusion

The goal of the simulations was to determine the COMSOL parameters required to accurately simulate MEMS resonators. The effects of the PML mesh-density, substrate mesh-density, PML size, substrate size, and tether location on the quality factor were unknown at the beginning of this work. After examining the quality factors for the simulations it was determined that none of these parameters have a great effect on the quality factor. If the quality factor had exhibited a strong dependence on the any of the examined parameters the base model would be unusable. As a result of the independence from these parameters, simulations of novel resonator designs can now be performed in order to analyze quality factor trends.

The tether length and width simulations led to the conclusion that shorter and thinner tethers would lead to the best quality factors. This is intuitive given that a wider tether would allow more energy to escape. The reason why there was an increase in the quality factor for the 3/8-wavelength tether when going from 2 to 5 microns is unknown. More data is necessary before these trends can be fully understood.

7. Further Work

This research has led to the creation of a base model that can be modified to accurately simulate novel tethers designs. The following parameters have been identified as adequate.

PML width: 20 microns
PML max mesh element size: 10 microns
Substrate size: 40 microns x 40 microns x 40 microns
Substrate max mesh element size: 10 microns

Models for Gong's novel tether branching designs can be created using this base model. The data from the simulations will allow for accurate analysis of trends.

Acknowledgements

I would like to thank Dr. Gianluca Piazza for choosing me to do research this past summer in his lab. This opportunity has been invaluable in helping me determine my future career path. I was also able to see the thought process behind engineering research. I was able to see how an initial questions leads to a set of experiments that then lead to a conclusion. I would also like to thank Dr. Songbin Gong and Nick Kuo who helped me on a daily basis understand my results and determine the next step in my research. Lastly I would like to thank Dr. Jan Van der Spiegel for organizing the SUNFEST program. This is truly a unique experience that I would not have been able to have without the generous help from the SUNFEST program and the National Science Foundation.

References

[1] G. Piazza; P.J. Stephanou; A.P. Pisano, "Piezoelectric Aluminum Nitride Vibrating Contour-Mode MEMS Resonators," *Microelectromechanical Systems, Journal of* , vol.15, no.6, pp.1406-1418, Dec. 2006

[2] S.A. Chandorkar; M. Agarwal; R. Melamud; R.N. Candler; K.E. Goodson; T.W. Kenny, "Limits of quality factor in bulk-mode micromechanical resonators," *Micro Electro Mechanical Systems, 2008. MEMS 2008. IEEE 21st International Conference on* , vol., no., pp.74-77, 13-17 Jan. 2008

[3] D. S. Bindel and S. Govindjee, "Elastic PMLs for Resonator Anchor Loss Simulation," Department Paper, University of California, Berkeley, 2005.

[4] V. Bottom, Introduction to Quartz Crystal Unit Design. New York: Van Nostrand Reinhold, 1982,

[5] J. Taylor, Classical Mechanics. Sausalito, Calif. Palgrave, 2003,

[6] G. Piazza, “Piezoelectric Aluminum Nitride Vibrating RF MEMS for Radio Front-End Technology,” Ph.D. dissertation, Electrical Engineering and Computer Sciences, Univ. of Cal. Berkeley, Berkeley, CA, 2005

[7] B. Sjodin, private communication, June 2010.

[8] S. Gong, “UPenn Lo-Bar CSSA,” unpublished

[9] C. Zuo, N. Sinha, J. Van der Spiegel, and G. Piazza, "Multi-Frequency Pierce Oscillators Based On Piezoelectric AlN Contour-Mode MEMS Resonators," Departmental Papers, 2008.

NANOELECTRONIC SENSOR FOR DETECTION OF PROSTATE CANCER BIOMAKERS

SUNFEST Summer Undergraduate Fellowship in Sensor Technologies
Nathalia Garcia Acosta (Electrical Engineering) – Temple University
Advisor: Dr. A.T Johnson

ABSTRACT

Prostate cancer is the second cause of cancer death in American men; it is known that early detection of the disease is one of the most important tools for successful treatments. Unfortunately, current methods of diagnosis are either invasive or require high concentrations of prostate cancer biomarkers in order to detect the disease accurately. Here, we present an improved method for early detection, a nano electronic sensor for prostate cancer. This device relies on electrical sensing using a field effect transistor where the semiconducting channel is a functionalized single-walled carbon nanotube. These novel carbon structures have unique electronic and chemical properties that allowed us to fabricate a highly specific and highly sensitive nano sensor. Moreover, we designed a channel that allowed us to controllably deliver small amount of samples to the devices. This will allow real time detection since electrical measurements can be taken at same time the device is exposed to the biomarker. It is believed that this project could set up the platform to eventually have an array of these devices to detect several biomarkers in one step.

1. INTRODUCTION

According to the American Cancer Society, from 1999-2005 only 68% of cancer patients survived. After heart disease, cancer is the second most common cause of death in the United States [1]. One of the most effective tools against cancer is early detection since successful treatments depend on how advanced the cancer is when diagnosed. Particular attention is drawn to prostate cancer since it is the second most common cause of cancer death in American men.

Unfortunately, the American Cancer Society anticipates 217,730 new cases of prostate cancer in 2010; therefore current research is focused on alternative ways for screening this disease [1]. Current methods of early detection such as prostate cancer specific-antigen (PSA) screening and digital rectal exam are either invasive or in the case of PSA screening, it requires high concentration of PSA in order to detect accurately. Clearly, there is a need for a detection method that is fast, reliable, non-invasive, and able to detect PSA at lower levels. For that reason, this project takes advantage of the semiconducting properties of carbon nanotubes to make a device that meets those needs.

The proposed device is a nano electronic sensor that relies on electronic readout from a single-walled nanotube field effect transistor that after functionalization is highly sensitive to PSA. Since this sensor is a molecular device, it will be able to detect PSA at lower levels than current detection methods. In addition, alternative prostate cancer markers are being researched by our collaborators, which will allow us to make the device more specific. This project is believed could be the platform to have an array of hundreds of these devices that will test for various biomarkers, all in one step.

This macro project consists of four major areas: Fabrication, Liquid Handling, Functionalization, and Final Testing. Due to time limitations, this paper will discuss only Fabrication, Functionalization and Liquid Handling in Sections 3, 4 and 5 respectively while Section 2, Background, reviews the main points about carbon nanotubes, synthesis of carbon nanotubes, single-walled carbon nanotube field effect transistors, biological underpinnings of the device, and microfluidics. The Fabrication, Functionalization and Fluid Handling steps will set up a platform for future work on the design of the nano electronic prostate cancer sensor. Finally, Section 6 is dedicated to discussion and conclusions of the project.

2. BACKGROUND

2.1 Carbon Nanotubes

Nanomaterials have drawn particular attention due to their various applications in a wide range of disciplines. Carbon nanotubes (CNTs) were discovered in 1991 and since then, research in their applications has grown significantly [2]. They are great tools for sensor technologies due to their exceptional electronic and chemical properties. These carbon structures can be thought of as highly ordered sheets of carbon atoms rolled into seamless cylinders [3]. Carbon nanotube dimensions vary; their diameter can be as small as 1-nm for single walled nanotubes and as large as hundreds of nanometers for multiple-walled tubes, and in each case still can have lengths up to several millimeters [4]. Depending on their chirality (twists in the exact crystal structure) CNTs have different electrical properties from metallic to semiconducting [3]. Our focus is on single-walled, semiconducting carbon nanotubes, which make excellent electrical sensing devices.

2.2 Synthesis of Single-Walled Carbon Nanotubes

Synthesis of carbon nanotubes is a process that is still being improved given that current techniques provide only uncontrolled results. It would be ideal to be able to have control over the length, amount, and type of carbon nanotubes grown, but though some techniques are more advanced than others, synthesis of carbon nanotubes is still a challenging task. For this project, synthesis is done by chemical vapor deposition (CVD) since it is a simple and inexpensive method that provides high yield of single-walled carbon nanotubes [4]. The steps of the chemical vapor deposition process will be explained in Section 3.

2.3 Single-Walled Carbon Nanotube Field Effect Transistor

Single-walled carbon nanotubes (SWCNTs) are an excellent tool for sensing devices because due to their cylindrical geometry, every carbon atom is exposed to its surroundings. This characteristic makes CNTs very susceptible to nearby bio-molecules; this trait can be employed to fabricate a highly-sensitive device. Moreover, the small size of CNTs facilitates sensing at the molecular level, which is desirable in many fields, but particularly in biomedical applications.

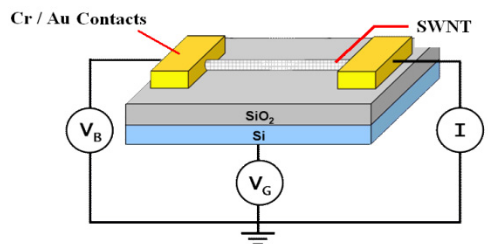

Figure2.3.1 Schematics of a single-walled carbon nanotube field effect transistor. [1]

In order to make use of the SWCNTs properties for a sensor device we are interested in semiconducting SWCNTs since these can be used as the semiconducting channel in a field effect transistor (FET) (Figure1.) Transistors have been the focus of attention for the microelectronics industry with miniaturization being one of the limits that the semiconductor industry has encountered due to the intrinsic quantum effects of semiconductors at a small scale [4]. Nano-electronic devices such as, carbon nanotube FETs, have given optimism that a solution can be found to miniaturization limits [6.] However, the fabrication of these devices is not a simple task because, as explained previously, synthesis of carbon nanotubes yields a mixture of metallic, semiconducting, single-walled, and multi-walled CNTs.

2.4 Biological Underpinnings

One of the important biological aspects for this project is the specificity by which antigens and antibodies attach. Antigens are foreign molecules that when entering the body stimulate the production of antibodies. Examples of antigens are toxins, viruses and

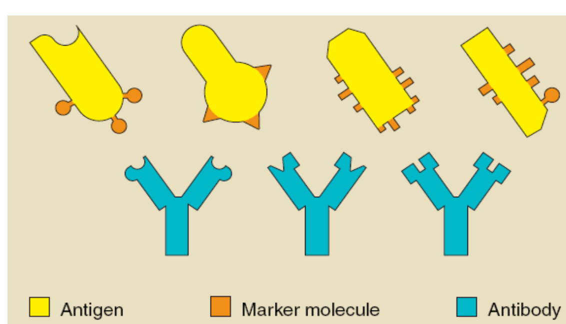

Figure 2. 4.1 Schematics of the antibodies and antigens key/lock system. [2]

bacteria. Antibodies are proteins that have, at the tip of their structure, an antigen site. This site is specific for only one type of antigen (Figure2.4.1) This biological trait is desirable for advancements in sensor technology since it could be use as a highly-specific detection method. However, there are a few concerns about this technique such as the biological-electronic interface. Specifically, we are concerned about the hydrophobic characteristics between proteins (antibodies) and carbon nanotubes [6]. In addition, the device must have the capability to test complex fluids such as a blood sample, which could compromise the device's electronic characteristics.

2.5 Microfluidics

The field of microfluidics has to do with the control of small volumes of liquids in a channel of dimensions on the micron scale. The promising ground of microfluidics has been used as an interface among subsystems in devices that require measurement or control of complex fluids [7]. This, of course, is ideal because it would allow a multi-step process to be done in one step, all within one device. Moreover, microfluidics techniques are ideal for disease diagnosis because they provide straightforward analysis of complex fluids such as glucose and DNA. Common methods of detection that involve microfluidics rely on optical detection after the fluid has been marked (usually with dyes.) However, here we are dealing with a more complicated set up since the sensing relies on electronic readout, which could be hindered by the liquid environment on the device.

3. FABRICATION OF FIELD EFFECT TRANSISTOR

3.1 Wafer Preparation

Minimal contamination during this process is extremely critical to obtain reliable nano-devices. We started with a 4-inch diameter silicon/silicon dioxide wafer, which was cleaned by oxygen plasma and then covered with a metal catalyst. For this experiment, the catalyst used is iron nitrate dissolved in isopropanol, which is then spun onto the wafer (Recipe 1). The catalyst step provides control over the synthesis CNTs since the diameter of CNTs is proportional to the size of the catalyst particles. However, there are many other variables that affect the random process of carbon nanotubes self-assembly and not always we obtained the desired results.

3.2 Synthesis of Carbon Nanotubes

The CVD process consists of heating up the furnace to 900° C where the wafer is kept inside a quartz tube. At this temperature a process

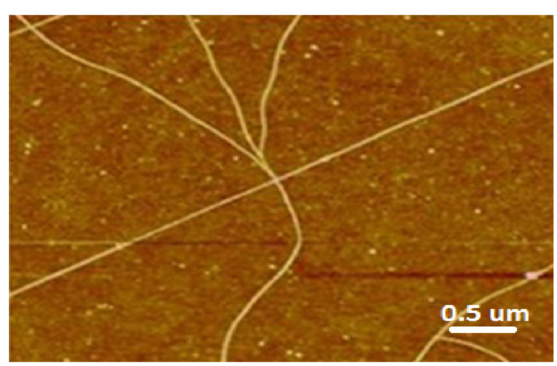

Figure 3.2.1 AFM image of CNTs on wafer after CVD growth. Image obtained by lab member.

gas, nitrogen, and a carbon-containing gas, methane, are flowed into the tube (Recipe 2). The flow of these two gases is done for two minutes, time in which CNTs will grow at the catalyst sites. After the synthesis is completed, we examined the wafer by atomic force microscope (AFM) in order to find CNTs (Figure 3.2.1)

3.3 Patterning and Deposition of Electrodes

Subsequently, the electrode sites were patterned by photolithography using a chrome mask (Recipe 3.) After that, the metal deposition of the electrodes was done by evaporating a layer of 5 nm thick of chrome, and a 40 nm thick layer of gold (Recipe4). After evaporation a lift of process was performed to remove the unwanted metal from the wafer (Recipe 5.)

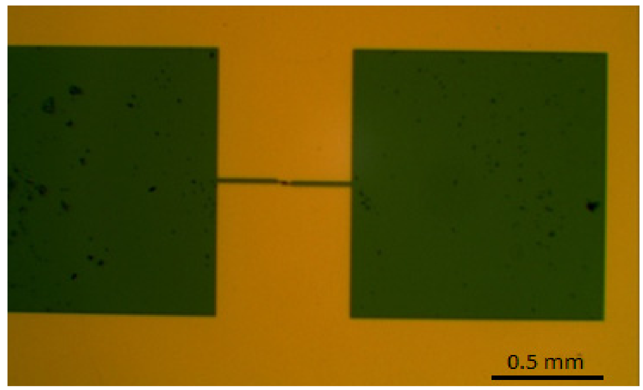

Figure 3.3.1. Pair of electrodes trenches formed by photolithography. Image obtained by lab member

Keep in mind that the whole wafer is patterned with several pairs of electrodes without knowing the location of the CNTs. Figure 3.3.1 shows a pair of electrode trenches after photolithography.

3.4 Current vs. Voltage measurements

The final step of fabrication is to measure the current through each pair of electrodes of each device when a 10 mV voltage is applied to the gate. As explained previously, we are looking for semiconducting SWCNTs with an IVg curve (current vs. Gate voltage) as shown in Figure 3.4.2. The probing set up used is shown in Figure 3.4.1. After probing all the devices, we determined the yield of carbon nanotube FETs.

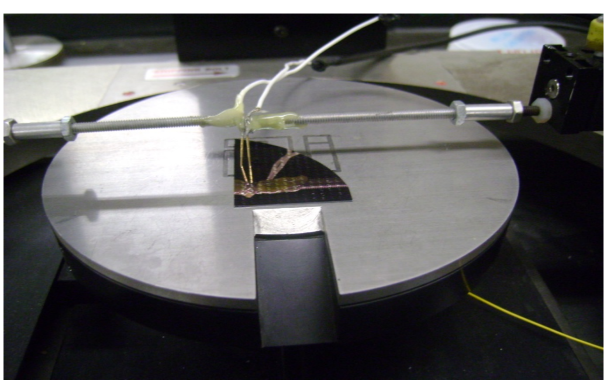
Figure 3.4.1. Probing set up at the Johnson's lab. Picture taken by lab member

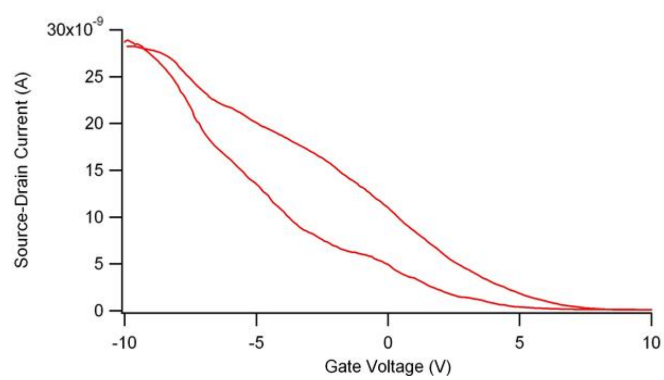

4 FUNCTIONALIZATION

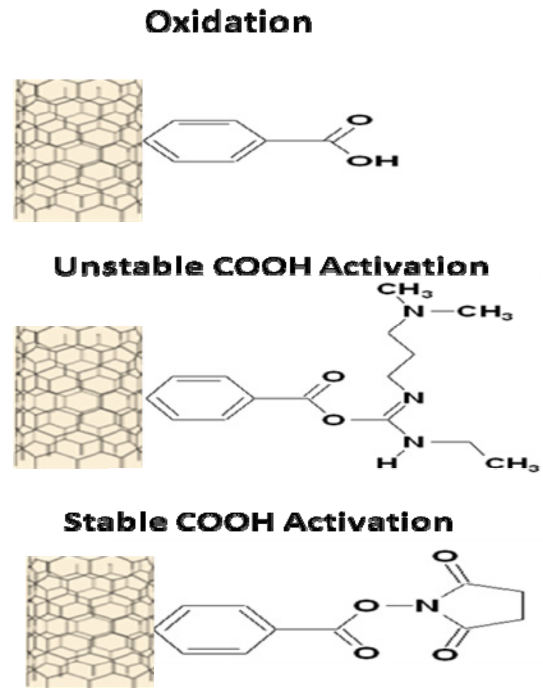

The devices were then functionalized to detect prostate cancer. The carbon nanotubes were chemically processed, first with an oxidation step done by diazonium, followed with a bath in a solution of EDC, NHS and MES buffer (Recipe 6.) As shown on Figure 4.1, this process generates a chemical bonding site for the prostate cancer antibody. The devices were exposed to the prostate cancer antibody for 45 minutes in a moist environment to mimic in vivo conditions. After that, the functionalized devices were exposed to the prostate cancer biomarker for 10 minutes, again mimicking humid conditions. Throughout this process electronic measurements were taken before and after functionalization, and after antigen contact. Results are shown in Figure 4.2.

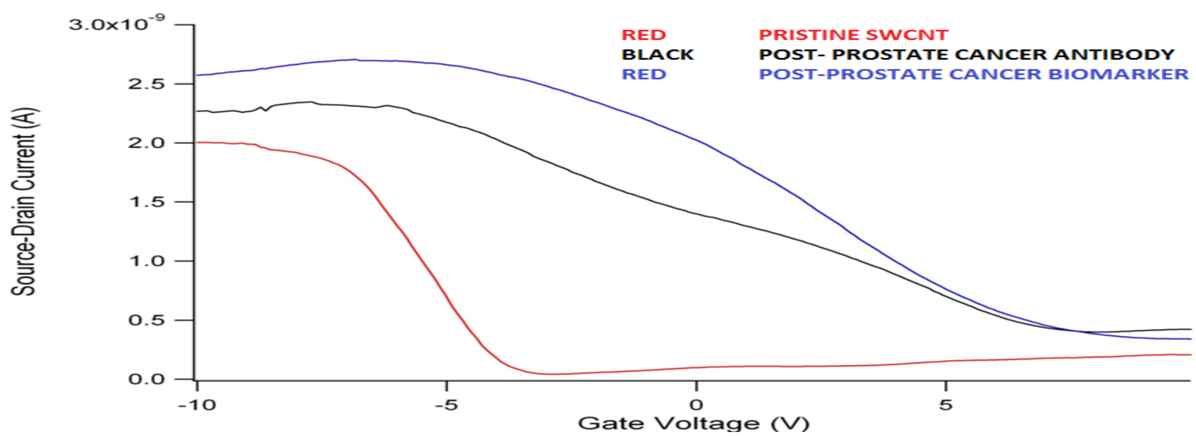

Figure 4.2.Electrical data taken during the functionalization steps Image obtained by lab member

5. FLUID HANDLING

The purpose of this step was to design a channel that allowed us to take electrical measurements while the fluid being tested is passing through the semiconducting channel (CNT) of the device. This is, of course, important for a real time detection, which will provide faster diagnosis than current methods. In addition, having this whole process happening within a channel prevents contamination or any effects that having the devices exposed to ambience, which happens during functionalization, could cause. Also, the channel eventually will allow us to test complex fluids such as blood instead of purified proteins, which is what we are using currently. The initial experiments were performed on non-functionalized devices since the first step is to flow fluid through the semiconducting channel while being able to acquire electrical data. That is, a fluid needs to pass through the small area (2.5 mm) between the electrode pads of the FET so that the electrical data is not hindered by surrounding liquids. The schematics of the proposed channel are shown in Figure 5.1.

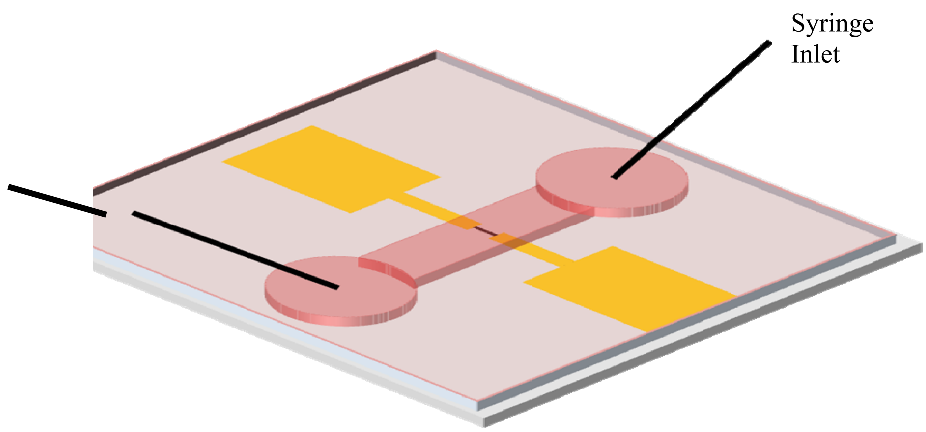

5.1 Channel Mold Design

Experimentally, we decided that the channel should have the following characteristics:

Proposed Channel for Fluid Handling			
Physical Dimensions			
	Material	**Dimensions**	**Height**
Petri Dish	Plastic	80 mm diameter	10 mm
Channel Pattern	Teflon tube	4 mm length, 1 mm diameter	1 mm
Inlet/Outlet	Epoxy	~1.5 mm diameter	~1.2 mm

Table 5.1.1 Details of the proposed channel.

Figure 5.1.1 shows the end result of the proposed PDMS channel placed between electrode pads. The method used to make this channel is explained below. Keep in mind that this is an inexpensive and fast method of making a microfluidics channel that did not require the use of a clean room. Though there are more advance techniques to fabricate a microfluidics channel, our main focus was to have small-metered amount of fluids through the CNT without affecting the electronic readout, which we believed can initially be tested with this channel.

Figure 5.1.1 Results of the proposed channel. Picture taken by a lab member.

The channel fabrication started with a mold made on a plastic Petri dish. A 1 mm diameter and 4 mm length Teflon tube was placed on the Petri dish; the tube served as the mold for the channel walls. For the inlet and outlet wells, a sphere profile was desired since we needed enough space to penetrate the syringe needle to pump the liquid through the channel. This profile was achieved by dispensing ~1.5 mm diameter drops of epoxy; this material was used because in addition to hardening as a drop, epoxy serves as glue between the Teflon tube and the Petri dish. (Figure 5.1.2 and 5.1.3)

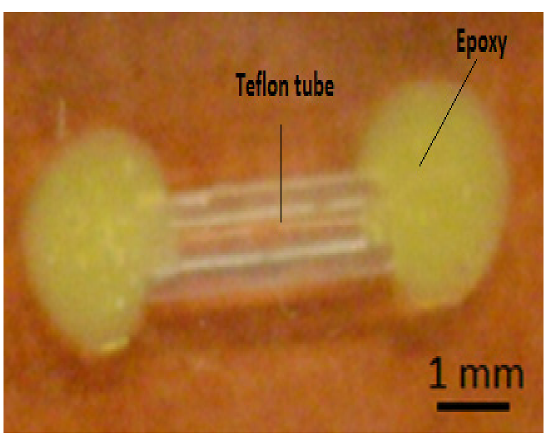

Figure5.1.2 Picture of a single channel taken by lab member.

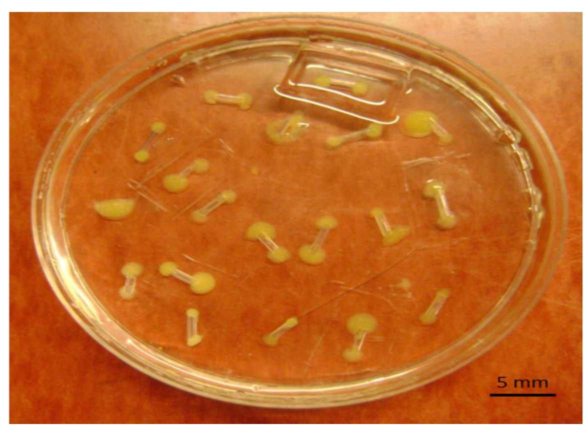

Figure 5.1.3 Channel mold showing 16 channels. Picture taken by lab member

5.2 Elastomeric Channel

After the channel mold was done, we needed an elastomeric material to conform around the shape of the channel (Figure 5.1.2) to form the channel walls. The elastomeric used is polydimethylsiloxane (PDMS) for several reasons as shown in Table 5.2.1

Advantages and Disadvantages of PDMS	
Advantages	**Disadvantages**
Low cost	Collapsing of channels
Low surface tension	Shrink 1% during curing
Transparent	Sagging of structures
Pliant	
Reliable	
Easy and Fast manufacture	
Biocompatible	
Permeable to oxygen	
Chemically inert	
Homogeneous	
Low water absorption	
Variable hydrophobicity	

Table 5.2.1. Benefits of PDMS material

Figure 5.2.1 PDMS Materials. Picture taken by lab member

There are various ratios for PDMS mixture. After various experiments, we concluded that 10:1.1 ratio produced the necessary properties for this task (Figure 5.2.1.) The PDMS mixture was poured onto the channel mold, and then it went through a degassing and curing process (Recipe 7.) After that, we cut around the channel, making sure that there was enough surrounding area (~ 10 mm) and carefully peeled the PDMS from the Petri dish. The PDMS channel was placed directly onto the wafer between the two electrodes of the device. It was critical to keep the PDMS surface clean because any contaminants or moisture would hinder its adherence properties.

5.3 Channel Testing

At this point we tested the channel with the set up shown in Figure 5.3.1.

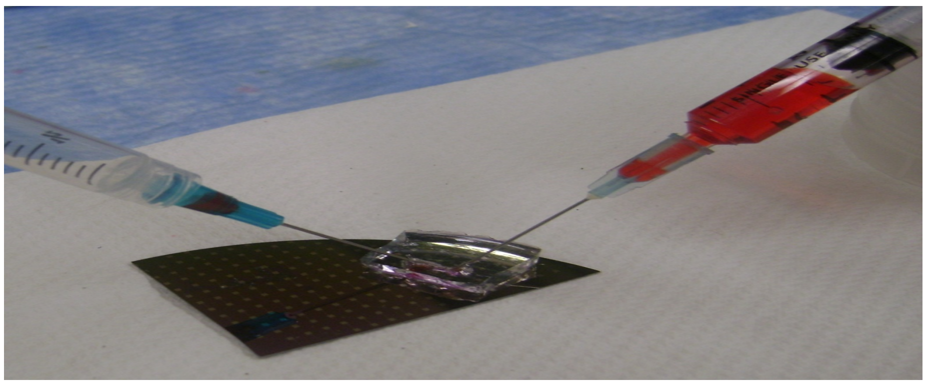

Figure 5.3.1 Set up that was created to test the channel. Picture taken by lab member

We introduced fluid to the channel with a syringe. We observed that the fluid went through the channel and it came out on outlet syringe without leaking.

6. DISCUSSION AND CONCLUSIONS

We were able to fabricate SWCNT field effect transistors successfully. When we probed each device we ended up with approximate 10-20% yield of devices, which is good considering that the growth of CNTs is an uncontrolled process, which yields a mixture of metallic, semiconducting, single-walled, and multi-walled CNTs. Then, we functionalized these devices by attaching prostate cancer antibody and exposed them to the prostate cancer biomarker. After that, we probed the devices to see if we could electrically sense the presence of prostate cancer biomarkers. This step is still in progress, but as we can see in Figure 4.2 there is a change from the measurement pre-prostate cancer biomarker exposure to post-prostate cancer biomarker, but more experiments need to be performed to characterize and understand this change. Finally, we designed a PDMS channel, which was placed between the two electrodes of the SWCNT FET (Figure 5.1). This channel passed fluid through the CNT without any leakage (Figure 5.3.1); eventually this will allow us to take electrical measurements while fluid was passing through the CNT. Future work will be focused on bringing the functionalization and fluid handling parts together in order to have real time, highly sensitive and highly specific detection method.

7. METHODS

Recipe 1. Wafer preparation

- Turn on plasma etcher
- Turn on nitrogen and oxygen tanks
- Vent the chamber with nitrogen and open
- Place silicon wafer inside
- Turn vacuum on to evacuate the air from chamber
- Set up voltage to 60 Watts
- As the pressure in the chamber is going down flow oxygen twice
- Once the chamber has reached low pressure the processing gas, oxygen is introduced, power is turn on at the same time to excite plasma, maintain for 5 minutes
- Turn off power and oxygen
- Vent the chamber with nitrogen
- Open and take wafer out
- Prepare the catalyst solution by mixing iron nitrate and isopropanol to form a 50 mg/L concentration
- Place silicon wafer on spinner
- Dispense the catalyst on the silicon wafer
- Spin the wafer at 3000 rpm for 1 minute (until wafer is visible dry)

Recipe 2. Carbon Nanotube Synthesis

- Cleave the silicon wafer so that they are smaller than 2-inch
- Place wafer in a 2inch diameter tube
- Close the seals on each end (ensure everything is tightly closed)
- Place tube in the furnace
- Set up furnace to heat up to 900°C
- Flow 320 sccm of hydrogen, 600 sccm of argon, and 300 sccm of methane for 10 minutes
- Turn off the methane and flow hydrogen and argon for 5 minutes
- Turn on furnace and wait until it reaches 900°C (approximately 1 hour)

- When it reaches 900°C turn on 2500-sscm for 2 minutes
- Turn off furnace
- Turn off methane
- Wait until the furnace temperature goes down to 400°C
- Open furnace and turn off hydrogen
- When furnace temperature reaches 100°C turn off argon and take sample out

Recipe 3. Lithography

- Pre-bake at 200 °C for 2 minutes
- Spin PMGI at 4000 rpm for 45 seconds
- Bake at 150° C for 5 minutes
- Spin 1813 photo resist at 5000 rpm for 45 seconds
- Bake 130° C for 2 minute
- Expose to 405 nm light at 15 mW/cm^2 for 3.3 sec
- Develop in MF-319 as needed, usually about 2 min
- Rinse with DI water
- Dry wafer with nitrogen gun

Recipe 4. Evaporation-Deposition of Electrodes

- Using double sided tape attach the wafer to the evaporator stage
- Vent the chamber and open
- Place the chrome and gold pellets on the designated boats
- Place the stage in chamber and close
- Turn on rough pump
- Wait until chamber reaches 30 mT pressure
- Turn off rough pump
- Turn on high vacuum
- Wait until chamber reaches 8x10^-7 mT pressure
- Turn on power so current starts flowing
- Wait until the reading stays at 0.100 nm
- Open the shutter and hit "process"
- Monitor thickness that is being deposited to 40-nm
- Turn off power
- Wait for ~5 minutes to cool down
- Turn off high vacuum
- Vent chamber

Recipe 5. Liftoff

- Prepare a four bath system with acetone, CD-26 developer, isopropanol, and DI water
- Immerse chip in glass container filled with acetone, shake constantly until visually the metal has come off.
- Change chip to the second bath, CD-26 developer, inspecting that all the residue from the first bath has left the chip
- Change chip to the acetone bath just for a few seconds
- Immerse the chip in DI- water, at this point very little residue should be visible in the DI-water
- Dry with nitrogen gun

Recipe 6. Functionalization

- Immerse the devices in a solution of 25mg/L of diazonium and DI water
- Heat up device in diazonium solution for one hour at 45°C
- Take the chip out of the diazonium and perform a three bath system with acetone, methanol, and DI water
- Dip chip in a solution of 16 mg of NHS, 6 mg of EDC and 15 mL of MES buffer for 15 minutes
- Perform bath with MES buffer and DI water
- Blow dry with nitrogen
- Pipette a drop of prostate cancer antibody on the device and keep chip in a moist environment for 45 minutes
- Wash chip with DI water and blow dry with nitrogen
- Pipette a drop of the prostate cancer biomarker for 10 minute
- Wash chip with DI water and blow dry with nitrogen

Recipe 7. PDMS

- Mixed the PDMS base curing agent 10:1.1 ratio respectively
- Degas PDMS by placing in a desiccator connected to a rough pump to create vacuum.
- Cure PDMS for 2.5 hours at 75°C

ACKNOWLEDGEMENTS

A.T Johnson Group
Jan Van der Spiegel
National Science Foundation

REFERENCES

1. American Cancer Society, Cancer Facts & Figures 2010. Atlanta: American Cancer Society, 2010.
2. S.Ijima, “Helical Microtubules of Graphitic,” *Nature*, vol.354, pp. 56-58, Nov. 1991.
3. T. Kuzma “Nanofabrication Manufacturing Technology Manual,” PennState University NanoManufacturing Technology program, Jun. 2008.
4. C.N.R. Rao, FRS and A. Govindaraj, *Nanotubes and Nanowires,* Cambridge: The Royal Society of Chemistry, 2005, pp.16.
5. A.S Sedra and K.C Smith, *Microelectronic Circuits,* 5th ed. New York: Oxford University Press, 2004
6. A. Star, J.C.P Gabriel, K. Bradley, G. Gruner, “Electronic Detection of Specific Protein Binding Using Nanotube FET Devices,” *Nano Letters,* vol.3, No.4, pp 459-463, Mar. 2003.
7. D.A. Rutenberg and M.A. Reed, “Microfluidic Probe: A New Tool for Integrating Microfluidic Environments and Electronic Wafer-Probing,” *Lab Chip,* vol.10, pp.123-127, 2010.

IN VITRO INVESTIGATION OF CYTOKINE-MEDIATED NUCLEUS PULPOSUS DEGENERATION

NSF Summer Undergraduate Fellowship in Sensor Technologies
Sarena Horava (Chemical Engineering) - University of Massachusetts Amherst
Advisor: Dawn Elliott
Post-Doctoral Fellow: Lachlan Smith

ABSTRACT

Degeneration of the lumbar intervertebral discs is strongly implicated as a cause of low back pain, and may also lead to impaired mobility. A lack of understanding of the pathomechanisms that underlie degeneration limits our ability to develop biological treatments that both alleviate painful symptoms and restore function. The process of degeneration is characterized by up-regulation of pro-inflammatory cytokines—particularly interleukin 1 beta (IL1β) and tumor necrosis factor alpha (TNFα)—within the central nucleus pulposus. Furthermore, the increased production of these cytokines is not matched by increasing amounts of their inhibitory regulators, resulting in an imbalance of catabolic and anabolic activity. In this study, we developed an in-vitro model of the nucleus pulposus that was used to investigate the effects of IL1β and TNFα on composition and mechanical function. In addition, we examined the capacity of IL1 receptor antagonist (IL1ra) and soluble TNF receptor 1 (sTNFR1), inhibitors of IL1β and TNFα respectively, to mitigate cytokine-mediated functional and compositional changes. Our results demonstrated that short-term exposure to IL1β, but not TNFα, causes loss of matrix components that significantly compromises mechanical function, suggesting that IL1β plays a more direct role than TNFα in driving matrix degradation in the nucleus pulposus. Our results also demonstrated that IL1ra can effectively prevent compositional and functional changes induced by IL1β, highlighting its therapeutic potential.

1. INTRODUCTION

Disorders of the lower back impact our society, both physically through individual impairment and financially through medical expenses. The most common cause of musculoskeletal impairment is low back pain. The prevalence of low back pain among the general U.S. population is very high, reaching 25 percent [1]. From a financial viewpoint, back disorders result in lost productivity and increased health care costs. Since low back pain is a common disorder negatively affecting society, much medical research has focused on the causes and treatment of low back pain.

Intervertebral discs (IVDs) are a critical component of the spine. These discs are pads of fibrocartilage that both transfer and distribute compressive loads between vertebral bodies, and permit spinal movement. Intervertebral disc degeneration is strongly implicated as a cause of low back pain [4-7]. Current treatments for painful disc degeneration, such as spinal fusion, are aimed at allaying painful symptoms, without restoring function. The limit of these treatment options is in part due to an incomplete understanding of the biological mechanisms involved. The central nucleus pulposus (NP) is crucial to disc function and health, and is the focus of this research [8,9]. Our objective was to investigate the initiation and progression of IVD degeneration and potential therapies using a new in vitro NP model. A complete understanding of the fundamental mechanisms associated with disc degeneration is necessary for developing novel treatments of low back pain.

2. BACKGROUND

2.2 Intervertebral Discs

2.2.1 Disc Anatomy

The spine consists of vertebral bones interconnected with intervertebral discs. The discs are soft tissue structures that provide flexibility and integrity to the spine. IVDs both transfer and distribute compressive loads between vertebrae, and permit spinal movement. Proper function is based on IVD structure. Three regions comprise each disc: an outer anulus fibrosus (AF); superior and inferior cartilaginous end plates; and the central NP [8, 9] (Figure 1).

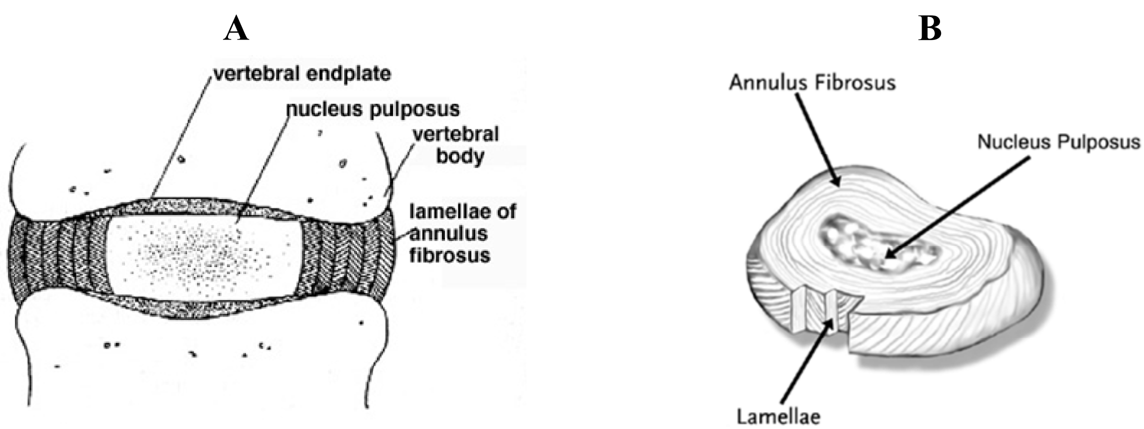

Figure 1. The structure of the intervertebral disc: (**A**) sagittal and (**B**) transverse sections. (Sources: http://www.medscape.com/viewarticle/405642_2 and http://www.chiropractic-help.com/L4-Lumbar-Spine.html)

2.2.2 Nucleus Pulposus

The NP is a pressurized gel of randomly distributed collagen II fibrils in a hydrated extrafibrillar matrix rich in proteoglycans [10, 11] (Figure 2). In compression under spinal axial loads, the NP is confined peripherally by the AF, which generates a region of uniform hydrostatic pressure in the disc. The NP pressure further enables the even distribution of the axial compressive loads between vertebral bodies [8, 9].

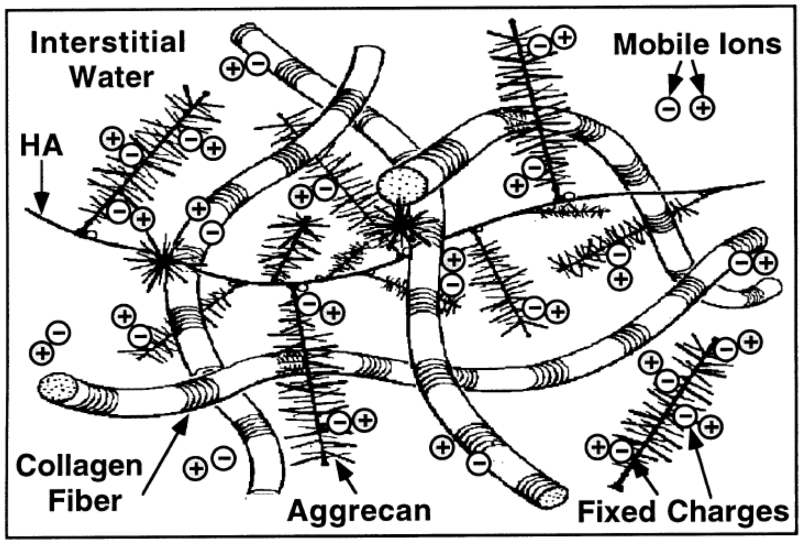

Figure 2. This NP matrix schematic shows collagen fibers interwoven with proteoglycans. GAG are the side chains found on proteoglycans. The negative charges are associated with GAG amd the positive charges are the sodium ions in water. (Source: Mow et al, 1998, Int. J. Solids Structures)

2.3 Human Disc Degeneration

2.3.1 Alterations in NP Structure, Composition, and Mechanics

Human disc degeneration starts in the NP with associated alterations in structure, composition, and mechanics. One of the earliest indicators of disc degeneration is loss of glycosaminoglycan (GAG) content in the NP, followed by water loss [14-16]. Changes in matrix composition impair mechanical function. Such comprised functional changes result in reduction in NP pressure and alterations in motion segment stiffness, predisposing the tissue to injury and stress [12, 13]. These NP changes initiate a cascade expanding to other disc structures, particularly the AF. The reduced NP pressure causes an inward bulging of the AF, which is distinctly visible in the middle image of Figure 3 [12]. A loss of distinction between the nucleus pulposus and anulus fibrosus is also characteristic of disc degeneration, as seen in Figure 4. As degeneration proceeds, progressive alterations in mechanics and composition occurs in the IVD structures, including decreased disc height decreases and the formation of tears [17] (Figure 3).

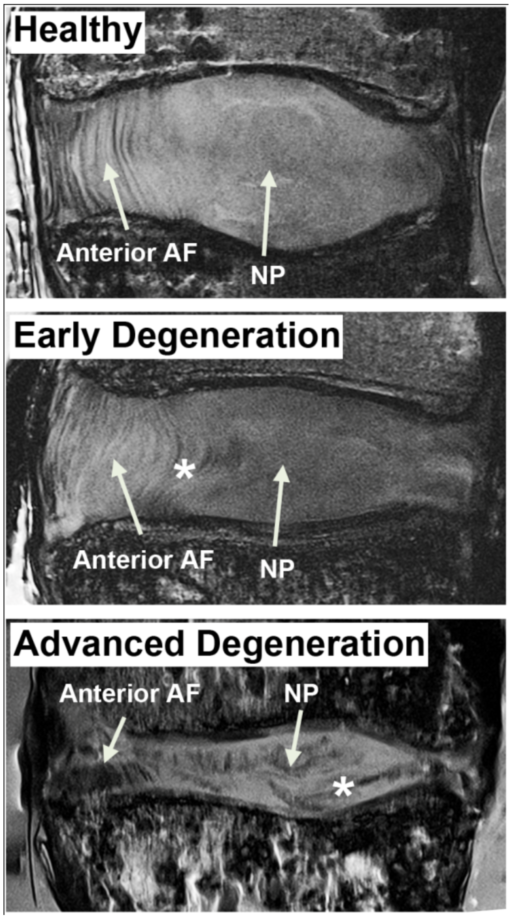

Figure 3. The MRI images of human IVDs shows the contrast between a healthy disc and the progressive effects of degeneration. (Source: Smith et al, 2010, Dis. Model. Mech.)

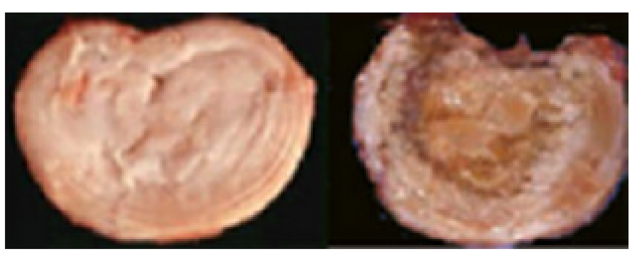

Figure 4. Intervertebral disc degeneration: healthy disc (left) and degenerate disc (right). (Source: http://www.physiol.ox.ac.uk/EURODISC/)

2.3.2 Cytokine-Mediated Matrix Degradation

Human disc degeneration is also associated with alterations in cellularity and biology. A lack sufficient nutrient supply to the NP affects the normal biological cellular pathways, beginning the degeneration process. As degeneration progresses, overall cell density decreases primarily due to apoptotic response [18]. Consequently, the compositional and functional NP changes occur in an increasingly inflammatory microenvironment, characterized by the up-regulation of cytokines [19, 20]. The two key pro-inflammatory cytokines associated with disc degeneration are interleukin-1β (IL1β) and tumor necrosis factor α (TNFα). The expression of IL1β is significantly greater in degenerate discs and TNFα is also increased but to a lesser extent [19]. In healthy IVDs, naturally occurring inhibitory proteins—interleukin-1 antagonist receptor (IL1ra) and soluble TNF receptor 1 (sTNFR1)—block the activity of catabolic cytokines—IL1β and TNFα—respectively [19, 21, 22]. However, in disc degeneration, the increased cytokine levels occur without a concomitant increase in their associated inhibitors. The unmatched production of cytokines and inhibitors causes an imbalance in catabolic and anabolic events. Secondarily, increased levels of catabolic enzymes, specifically MMP3, MMP13, and ADAMTS4, are characteristic of human disc degeneration [23]. The increases in both cytokines have been demonstrated to significantly increase MMP3, MMP13, and ADAMTS4 expression and decrease expression of NP matrix proteins including aggrecan and collagen II [24, 25]. Matrix degradation of the NP is a key event in IVD degeneration [24].

The up-regulated cytokines are targeted in ordered prevent the cascading effects of NP matrix degradation. Therefore, inhibitors IL1ra and TNFR1 have promising therapeutic potential in preventing cytokine-mediated NP degradation and reducing further catabolic activity found in disc degeneration.

2.4 Pro-Inflammatory Cytokines

2.4.1 Association of IL1 with IVD

As a key event in IVD degeneration, matrix degradation in the nucleus pulposus has been the focus of many investigations. The first evidence of the possible involvement of IL1 in matrix degradation in degenerate discs was found in 1988 in in-vitro experiments using rabbit AF cells [26]. A 1997 study extended these observations of IL1 into human IVDs without fully localizing enzymes in the AF and NP [27]. According to more recent evidence, normal IVD cells show an expression of both isoforms—IL1α and IL1β—with a matched expression of the natural IL1 inhibitor, IL1ra [21]. In degeneration, IL1β is up-regulated without increased IL1ra, leading to localized increased catabolic activity. A 2008 in-situ zymography investigation further showed that IL1 up-regulates enzyme activity and IL1ra inhibitor reduces induced catabolic enzyme activity [24].

2.4.2 Association of TNFα with IVD

TNFα was first described in IVDs in relation to sciatic pain [24]. Other studies have found that TNFα is present in both normal and degenerate IVDs [28]. However, the role of TNFα in disc degeneration is under debate with conflicting evidence. According to an in-vitro NP model study, using normal bovine NP cells on a porous calcium-based substrate, TNFα induced a loss of matrix molecules and decreased matrix synthesis [29]. However, a recent in-situ study of human IVDs reported no effect of TNFα on matrix-degrading activity. In this study, gene and protein expression data indicated TNFα up-regulation, and further evidence showing an absence of TNF receptor expression [24].

2.4.3 Roles of Cytokines

Previous studies have established an association of both cytokines IL1β and TNFα in normal and degenerate IVDs. However, the roles of these cytokines in initiating NP matrix changes in under debate. Previous studies have also shown matrix changes due to increases in these cytokines, but not the functional significance of NP compositional changes.

3. METHODS

3.1 Cell Isolation and Preculture

Mature NP cells were isolated from bovine caudal discs. Isolated cells were expanded in monolayer, in Dulbeccos Modified Eagly Medium (DMEM) containing 10% fetal bovine serum and 1% penicillin/streptomycin/Fungizone (PSF). Cells were expanded through two passages for this study.

3.2 NP Constructs and Treatment

NP cells were suspended in chemically defined media (CM) and combined 1:1 with sterile type VII agarose in phosphate buffered saline (PBS) at room temperature. Chemically defined media consisted of DMEM supplemented with 1x PSF; 0.1µM dexamethasone; 50mg/mL ascorbate 2-phosphate; 40mg/mL L-proline; 100mg/mL sodium pyruvate; and 1X6.25µg/mL insulin, 6.25µg/mL transferring, 6.25ng/mL selenious acid, 1.25mg/mL bovine serum albumin (BSA), and 5.35µg/mL linoleic acid. NP Cells were seeded in agarose gels (4mm diameter X 2.254mm thick) at a density of $20X10^6$/ml and allowed to gel for 20 minutes. NP constructs were precultured for 6 weeks in CM containing 10ng/ml transforming growth factor beta 3 (TGFβ3). The preculture period allowed for the development of a functional matrix. Samples were then removed and cultured for an additional two weeks in media without TGFβ3. Samples were divided into treatment groups (n=7) designated for IL1 treatment or TNF treatment (Table 1). After 3 days of treatment, samples were evaluated for histology, mechanics, and biochemistry.

IL1 Treatment Groups (n=7)	**TNF Treatment Groups (n=7)**
rh IL1β, 10ng/ml	rh TNFα, 10ng/ml
rh IL1β, 10ng/ml + rh IL1ra, 100ng/ml	rh TNFα, 10ng/ml + rh TNFR1, 100ng/ml
rh IL1ra, 100ng/ml	rh TNFR1, 100ng/ml
Control (no treatment)	Control (no treatment)

Table 1. Treatment groups for both IL1 and TNF with dosages of cytokine and/or inhibitor.

3.3 Histology

For histology, samples were fixed in 4% paraformaldehyde, dehydrated in a graded series of ethanol, and embedded in paraffin. Samples were sectioned at 7 μm-thickness from the middle of the construct. Sections were stained with Alcian Blue (pH 1.0) for sulfated proteoglycans and Picrosirius Red (0.1% w/v in saturated picric acid) for collagens.

3.4 Mechanics

Samples from each treatment group were mechanically tested in confined compression (n=5). The confined compression test was used to replicate the physiological conditions of the NP. The mechanical testing device consisted of an acrylic chamber fixed above a porous platen, in a bath filled with culture medium. The in-vitro NP construct was peripherally confined by the chamber in order to model the in-vivo NP confined by the AF. An impermeable ceramic indenter attached to a mechanical testing device applied compression. First, samples were equilibrated under a static preload of 0.02 N held for 500 seconds. Samples were subjected to a stress relaxation test, consisting of 10% strain (calculated from post-creep thickness values) applied at 0.05%/s, followed by relaxation to equilibrium for 10 minutes. Aggregate modulus, H_A, was calculated as the final equilibrium stress divided by the applied strain. The aggregate modulus was used as a measure of stiffness of the tissue at equilibrium. Hydraulic permeability, k_0, was calculated using a linear biphasic theory, assuming material isotropy [30]. The hydraulic permeability models the rate at which fluid flows out of the construct.

3.5 Biochemical Analysis

For the biochemical analysis, the glycosaminoglycans, collagen, and DNA content were determined using three assays. First, the samples were weighed for wet weight, dried overnight, and weighed again for dry weight. Dried samples were digested for 16 hours in papain (0.56U/mL in 0.1M sodium acetate, 10M cysteine hydrochloric acid, 0.05M ethylenediaminetetraacetic acid, pH 6.0) at 60C. After digestion, the PicoGreen dsDNA assay was used to determine the DNA content. Digested samples were evaluated for GAG content using the 1,9-dimethylmethylene blue dye-binding (DMMB) assay against a standard curve of chondroitin-6-sulfate. After acid hydrolysis of the sample digests, the collagen content was determined using the orthohydroxyproline (OHP) assay. DNA content was reported as amount per construct, and GAG and collagen values are reported as percentages of wet weight.

3.6 Statistical Analysis

Differences in mechanics and composition between groups were assessed using ANOVAs and Student Newman-Keuls pair-wise post-hoc tests, with significance considered for $p<0.05$.

4. RESULTS

4.1 Histology

Histological staining results were used to confirm the uniform distribution, particularly of GAG, in the extracellular matrix. Functionally mature constructs are shown in Figure 3. Alcian Blue staining for GAG was uniformly distributed and intense. Picrosirius Red staining for collagen was a more diffuse distribution, showing both pericellular and intercellular staining.

A **B**

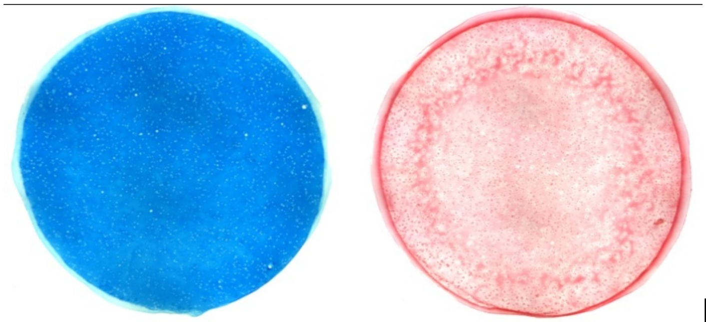

Figure 3. Histology staining of functionally mature constructs for (**A**) GAG using Alcian Blue and (**B**) collagen using Picrosirius Red. (Images taken by author)

4.2 Mechanics

Treatment with IL1β resulted in a significant decrease of 33% in aggregate modulus, H_A, and a significant increase of 41% in hydraulic permeability, k_0, compared with untreated controls (Figure 4, *p<0.05). For groups treated with IL1β +IL1ra or IL1ra only, aggregate modulus, H_A, and hydraulic permeability, k_0, did not differ significantly from controls. For all samples in the TNF treatment groups, no changes in H_A and k_0 were found.

A **B**

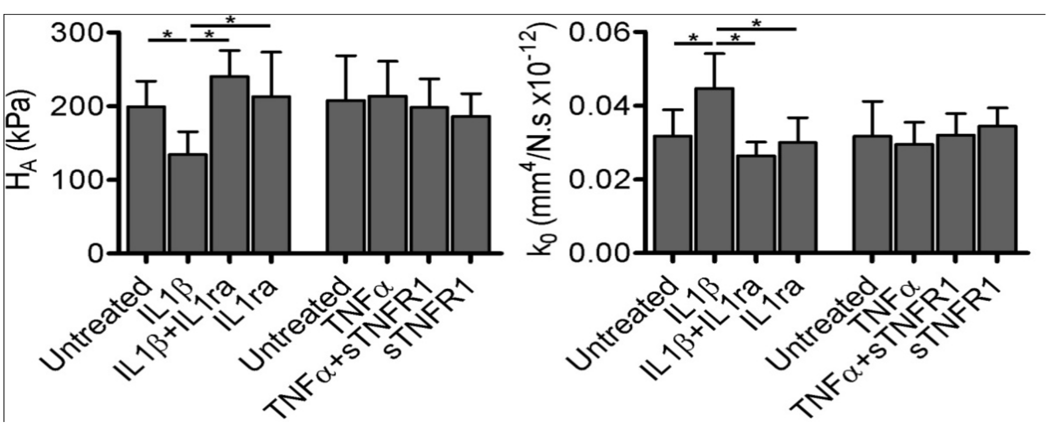

Figure 4. Mechanical testing results: (**A**) aggregate modulus and (**B**) hydraulic permeability.

4.3 Biochemical Analysis

For all treatment groups, no significant changes in DNA content were found. Samples treated with IL1β showed a significant decrease in GAG (27%) relative to untreated controls. For samples treated with IL1β + IL1ra or IL1ra alone, GAG was not significantly different from controls, but was significantly greater than IL1β only group. In comparison to controls, there were no differences in GAG for all TNF treatment groups. Collagen followed a similar trend as for GAG, but no significant differences between treatment groups were found.

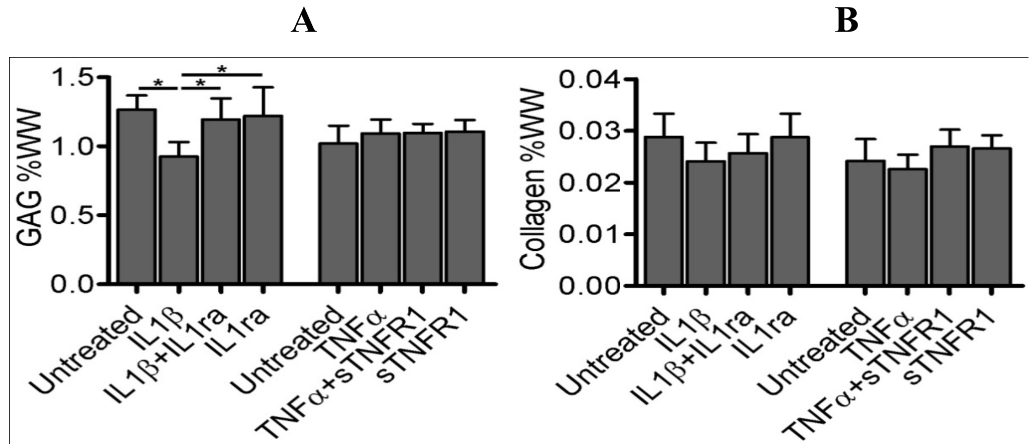

Figure 5. Biochemical analyses results: (**A**) GAG content as %/water weight and (**B**) collagen amount as %/water weight.

5. DISCUSSION

Intervertebral disc degeneration is the major cause of chronic low back pain for which current treatment methods have limited success. In intervertebral disc degeneration, changes in the extracellular matrix of the nucleus pulposus lead to reduction in function. Up-regulation of catabolic cytokines—IL1β and TNFα—in the NP of degenerate discs are associated with alterations in composition [20]. However, there has been some debate as to which of these cytokines has a more direct role in initiating NP extracellular matrix changes [22, 29]. In the literature, the effects of TNFα in disc degeneration are under debate with some evidence showing minimal effects and others showing no effects. The results of this study support the idea that IL1β plays a more direct role than TNFα [22].

Both mechanical and biochemical analyses demonstrate statistically significant effects of IL1β treatment. Mechanical testing results for IL1β groups showed decreased aggregate modulus and increased hydraulic permeability relative to untreated controls. Alternations in mechanical properties for IL1β treatment followed similar trends as for physiological conditions of degenerate discs, while treatment with TNFα showed no difference. Further, biochemical results showed changes in composition corresponding to changes observed in mechanics. Treatment with IL1β, but not TNFα, showed extracellular matrix changes, specially decreased GAG. This study demonstrated short-term exposure to IL1β induced matrix changes that are functionally significant.

In IVD degeneration, IL1β is upregulated without increased levels of its natural inhibitor, IL1ra. Several recent studies have investigated the therapeutic potential of IL1ra in reducing the catabolic IL1β cytokine activity for disc degeneration. The results of this study demonstrate that IL1ra can effectively prevent NP matrix changes, particularly GAG loss, and the associated functional changes induced by IL1β.

In investigating the initiation and progression of IVD degeneration, specifically factors affecting the NP, our study found IL1β as a key cytokine regulating matrix degradation. As a key event in IVD degeneration, prevention of catabolic cytokine has practical therapeutic implications. IL1ra can effectively inhibit composition changes of the NP matrix, particularly GAG loss, and the associated functional effects induced by IL1β. Significant inhibitory effects place IL1ra as a key therapeutic agent for restoring function in the impaired disc tissue. Results are also clinically significant for developing novel treatments for IVD degeneration.

6. RECOMMENDATIONS

The in vitro investigation of disc degeneration and potential therapies is necessary for designing future applications of cytokine antagonists. Future work will focus on gene expressions specific to the down-regulation of anabolic genes and up-regulation of catabolic genes associated with degeneration. Investigating gene expression will further quantify changes in catabolic enzyme activity and matrix synthesis that follow cytokine exposure. Changes in catabolic and anabolic activity will be contributed to alternations in composition and mechanics. Other future work includes using biodegradable polymeric microspheres to deliver therapeutic agents and evaluating therapeutic agents in an in vivo model of disc degeneration. Results of the current study demonstrated the direct role of IL1β in disc degeneration and the inhibitory effects of IL1ra, which is important for novel treatment approaches.

ACKNOWLEDGMENTS

I would like to thank my advisor, Dr. Dawn Elliott, for selecting me and supporting me with this summer research project. I would like to especially thank Lachlan Smith, the post-doc with whom I worked closely, for his instruction, help, and invaluable guidance. Also, I would like to thank the McKay Lab for providing a welcoming and encouraging workplace and learning environment. I would also like to thank Jan Van der Spiegel and SUNFEST for providing me with this invaluable research program. Lastly, I would like to thank NSF for their continued support of the SUNFEST program through grants, as well as the NIBIB grant for funding this study.

REFERENCES

1. Roberts S, Eisenstein SM, Menage J, Evans EH, and Ashton IK, Mechanoreceptors in intervertebral discs. Morphology, distribution, and neuropeptides.[see comment]. Spine, 1995. 20(24): p. 2645-51.

2. Bogduk N, The lumbar disc and low back pain. Neurosurgery Clinics of North America, 1991. 2(4): p. 791-806.

3. Andersson GB, Epidemiological features of chronic low-back pain. Lancet, 1999. 354(9178): p. 581-5.

4. Deyo RA and Tsui-Wu YJ, Descriptive epidemiology of low-back pain and its related medical care in the United States. Spine, 1987. 12(3): p. 264-8.

5. Frymoyer JW, Back pain and sciatica. New England Journal of Medicine, 1988. 318(5): p. 291-300.

6. Luo X, Pietrobon R, Sun SX, Liu GG, and Hey L, Estimates and patterns of direct health care expenditures among individuals with back pain in the United States. Spine, 2004. 29(1): p. 79-86.

7. Knoke JD, Smith TC, Gray GC, Kaiser KS, and Hawksworth AW, Factor analysis of self-reported symptoms: does it identify a Gulf War syndrome? Am J Epidemiol, 2000. 152(4): p. 379-88.

8. Ishihara H, McNally DS, Urban JP, and Hall AC, Effects of hydrostatic pressure on matrix synthesis in different regions of the intervertebral disk. Journal of Applied Physiology, 1996. 80(3): p. 839-46.

9. Hunter CJ, Matyas JR, and Duncan NA, The three-dimensional architecture of the notochordal nucleus pulposus: novel observations on cell structures in the canine intervertebral disc. Journal of Anatomy, 2003. 202(Pt 3): p. 279-91.

10. Cassidy JJ, Hiltner A, and Baer E, Hierarchical structure of the intervertebral disc. Connective Tissue Research, 1989. 23(1): p. 75-88.

11. Marchand F and Ahmed AM, Investigation of the laminate structure of lumbar disc anulus fibrosus. Spine, 1990. 15(5): p. 402-10.

12. Thompson JP, Pearce RH, Schechter MT, Adams ME, et al., Preliminary evaluation of a scheme for grading the gross morphology of the human intervertebral disc. Spine, 1990. 15(5): p. 411-5.

13. Adams MA, Freeman BJ, Morrison HP, Nelson IW, and Dolan P, Mechanical initiation of intervertebral disc degeneration. Spine, 2000. 25(13): p. 1625-36.

14. Antoniou J, Steffen T, Nelson F, Winterbottom N, et al., The human lumbar intervertebral disc: evidence for changes in the biosynthesis and denaturation of the extracellular matrix with growth, maturation, ageing, and degeneration. J Clin Invest, 1996. 98(4): p. 996-1003.

15. Frobin W, Brinckmann P, Kramer M, and Hartwig E, Height of lumbar discs measured from radiographs compared with degeneration and height classified from MR images. European Radiology, 2001. 11(2): p. 263-9.

16. Olczyk K, Age-related changes in proteoglycans of human intervertebral discs. Zeitschrift fur Rheumatologie, 1994. 53(1): p. 19-25.

17. Stokes IA and Iatridis JC, Mechanical Conditions That Accelerate Intervertebral Disc Degeneration: Overload Versus Immobilization. Spine, 2004. 29(23): p. 2724-32.

18. Keshari KR, Lotz JC, Kurhanewicz J, and Majumdar S, Correlation of HR-MAS spectroscopy derived metabolite concentrations with collagen and proteoglycan levels and Thompson grade in the degenerative disc. Spine, 2005. 30(23): p. 2683-8.

19. Gruber HE, Ingram JA, Norton HJ, and Hanley EN, Jr., Senescence in cells of the aging and degenerating intervertebral disc: immunolocalization of senescence-associated beta-galactosidase in human and sand rat discs. Spine, 2007. 32(3): p. 321-7.

20. Le Maitre CL, Hoyland JA, and Freemont AJ, Catabolic cytokine expression in degenerate and herniated human intervertebral discs: IL-1beta and TNFalpha expression profile. Arthritis Res Ther, 2007. 9(4): p. R77.

21. Lotz JC, Colliou OK, Chin JR, Duncan NA, and Liebenberg E, Compression-induced degeneration of the intervertebral disc: an in vivo mouse model and finite-element study. Spine, 1998. 23(23): p. 2493-506.

22. Hutton WC, Elmer WA, Boden SD, Hyon S, et al., The effect of hydrostatic pressure on intervertebral disc metabolism. Spine, 1999. 24(15): p. 1507-15.

23. Le Maitre CL, Freemont AJ, and Hoyland JA, The role of interleukin-1 in the pathogenesis of human intervertebral disc degeneration. Arthritis Res Ther, 2005. 7(4): p. R732-45.

24. Hoyland JA, Le Maitre CL, and Freemont AJ, Investigation of the role of IL-1 and TNF in matrix degradation in the intervertebral disc, 2008 Rheumatology 47:6

25. Ohshima H, Urban JP, and Bergel DH, Effect of static load on matrix synthesis rates in the intervertebral disc measured in vitro by a new perfusion technique. Journal of Orthopaedic Research, 1995. 13(1): p. 22-9.

26. Shinmei M, Kikuchi T, Yamagishi M, Shimomura Y. The role of interleukin-1 on proteoglycan metabolism of rabbit annulus fibrosus cells cultured in vitro. Spine 1988; 13: 1284-90.

27. Kang JD, Stefanovic-Racic M, McIntyre LA, Georgescu HI, Evans CH. Toward a biochemical understanding of human intervertebral disc degeneration and herniation. Contributions of nitric oxide, interleukins, prostaglandin E2, and matrix metalloproteinases. Spine 1997; 22: 1065-73.

28. Weiler C, Nerlich AG, Bachmeier BE, Boos N. Expression and distribution of tumor necrosis factor alpha in human lumbar intervertebral discs: a study in surgical specimen and autopsy controls. Spine 2005; 30: 44-54.

29. Seguin CA, Pilliar RM, Roughley PJ, Kandel RA. Tumor necrosis factor α modulates matrix production and catabolism in nucleus pulposus tissue. Spine 2005: 30: 1940-8.

30. Soltz MA and Ateshian GA. Experimental verification and theoretical prediction of cartilage interstitial fluid pressurization at an impermeable contact interface in confined compression. Journal of Biomechanics 1998: 31:10: 927-34.

9. APPENDIX

NOTE: In review and submitted to the Orthopaedic Research Society Fall Conference 2010

Inhibition of Functional Matrix Degradation in a Cytokine-Mediated In-Vitro Model of Nucleus Pulposus Degeneration

+Smith, L J; Nerurkar, N L; Cortes, D H; Horava, S D; Dodge, G R; Hebela, N M; Mauck R L; Elliott, D M
Department of Orthopaedic Surgery, University of Pennsylvania, Philadelphia, PA
delliott@mail.med.upenn.edu

INTRODUCTION

Altered nucleus pulposus (NP) extracellular matrix composition and mechanical function are hallmarks of disc degeneration [1,2]. Early stage degeneration is characterized by decreasing aggrecan content, with the associated decrease in hydrostatic pressure impairing the ability of the NP to perform its most critical function: the even distribution and transfer of compressive loads between the vertebral bodies [3].

Changes in matrix composition occur within an increasingly inflammatory local microenvironment [1]. There is up-regulation of pro-inflammatory cytokines, particularly interleukin 1 beta (IL1β) and tumor necrosis factor alpha (TNFα), without a concomitant increase in associated inhibitory regulators of these cytokines [1].

The direct functional consequences of cytokine-mediated extracellular matrix changes in the NP have not been described, in part due to the lack of an appropriate mimetic in-vitro culture model. In this study we developed an in-vitro model that was used to investigate the effects of IL1β and TNFα on both NP extracellular matrix composition and mechanical function. In addition, we examined the capacity of IL1 receptor antagonist (IL1ra) and soluble TNF receptor 1 (sTNFR1), inhibitors of IL1β and TNFα respectively, to mitigate cytokine-mediated functional and compositional changes.

METHODS

Cell Isolation, Preculture and Treatments: NP cells were isolated from mature bovine caudal discs and expanded through 2 passages. Cells were seeded in agarose gels (4mm diam. x 2.4mm thick) at a density of $20x10^6$/ml, and precultured for 6 weeks in chemically defined media containing 10ng/ml TGFβ3 [4]. Samples were then removed and cultured without TGFβ3 for an additional 2 weeks. Samples were then divided into cytokine and inhibitor treatment groups (Table 1). After 3 days of treatment, mechanical properties and biochemical composition were evaluated.

Treatment Group	IL1	TNF
Cytokine Only	rhIL1β, 10ng/ml	rhTNFα, 10ng/ml
Cytokine + Inhibitor	rhIL1β, 10ng/ml + rhIL1ra, 100ng/ml	rhTNFα, 10ng/ml + rhsTNFR1, 100ng/ml
Inhibitor Only	rhIL1ra, 100ng/ml	rhsTNFR1, 100ng/ml
Untreated Control	Control (no treatment)	Control (no treatment)

Histology: To confirm uniform matrix distribution in mature constructs, samples were processed into paraffin. Sections were stained with either picrosirius red or alcian blue to demonstrate collagen and glycosaminoglycan (GAG) accumulation respectively.

Mechanics: Constructs from each treatment group were tested in confined compression (n=5). The testing system consisted of an acrylic chamber fixed above a porous platen in a bath filled with culture medium. Compression was applied with an impermeable ceramic indenter attached to a mechanical testing system. Samples were first subjected to a 0.02N preload for 500s, followed by a stress relaxation test, consisting of 10% strain applied at 0.05%/s, followed by relaxation to equilibrium for 10mins. Aggregate modulus, H_A, was calculated as equilibrium stress/applied strain. Hydraulic permeability, k_0, was determined using linear biphasic theory assuming material isotropy [5].

Biochemistry: Following mechanics, the same samples were weighed and digested in papain. Digests were assayed for DNA content (per construct), and sulfated GAG and hydroxyproline (collagen) normalized to wet weight.

Statistics: Differences in mechanics and composition between groups were assessed using ANOVAs and Student Newman-Keuls pair-wise post-hoc tests, with significance considered for $p<0.05$.

RESULTS

Histology: Functionally mature constructs are shown in Fig 1. GAG staining was intense and uniform, while collagen staining was more diffuse.

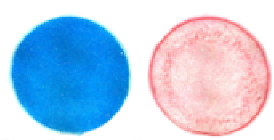

Figure 1. Functionally mature constructs: GAG (left) and collagen (right).

Mechanics: H_A increased from 2.5±0.4kPa (mean±SD) at day zero, to 199.23±4.7kPa following preculture. Treatment with IL1β resulted in a significant decrease in H_A (33%), and an increase in k_0 (41%) compared with untreated controls (Fig 2, *$p<0.05$). For samples treated with IL1β+IL1ra, or IL1ra alone, H_A and k_0 were not significantly different from controls. No changes in H_A or k_0 were found for any of the TNF treatment groups.

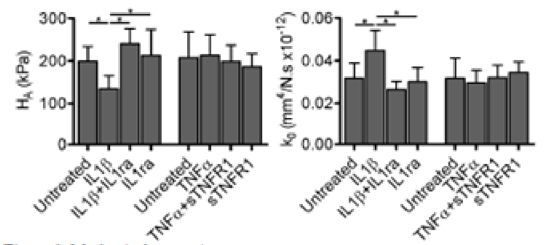

Figure 2. Mechanical properties

Biochemistry: Relative to untreated controls, GAG decreased significantly for samples treated with IL1β (27%), but was not different from controls for all other treatments (Fig 3, left, *$p<0.05$). Collagen showed a similar trend as for GAG, but there were no significant differences between groups (Fig 3, right). DNA did not change significantly for any of the treatments (not shown).

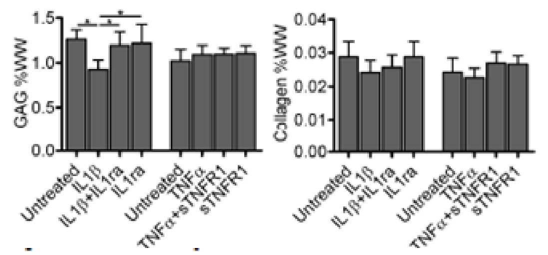

DISCUSSION

While both IL1β and TNFα are upregulated in the NPs of degenerate discs [1], there has been some debate as to which of these cytokines plays a more direct role in mediating extracellular matrix changes [6,7]. The results of this study support the hypothesis that IL1β plays a more direct role than TNFα [6]. Further, we have demonstrated that matrix changes, particularly decreased GAG, following short term exposure to IL1β are functionally significant. Our results support the therapeutic potential of IL1ra for disc degeneration [8,9], by demonstrating that IL1ra can effectively prevent NP GAG loss and the associated functional changes induced by IL1β.

The in-vitro culture model developed here presents a new platform for investigating biological mediators of disc degeneration and the associated compositional and functional changes. Future work will seek to quantify the changes in catabolic enzyme activity and matrix synthesis that follow cytokine exposure, and contribute to alterations in composition and mechanical properties.

ACKNOWLEDGEMENTS

This study was funded by NIBIB grant R01EB002425, and a Department of Veterans Affairs Merit Grant.

REFERENCES

[1] Le Maitre+ 2007 Biochem Soc Trans 35:4; [2] Johannessen+ 2005 Spine 30:24; [3] Boxberger+ 2006 J Orthop Res 24:9; [4] Huang+ 2009 Tissue Eng Part A 15:11; [5] Soltz+ 1998 J Biomech 31:10; [6] Hoyland+ 2008 Rheumatology 47:6; [7] Seguin+ 2005 Spine 30:17; [8] Le Maitre+ 2007 Arthritis Res Ther 9:4; [9] Goupille+ 2007 Arthritis Res Ther 9:6.

Autonomous Laser Locking System

NSF Summer Undergraduate Fellowship in Sensor Technologies
Brett Kuprel (Electrical Engineering) – University of Michigan
Advisor: Professor Daniel D. Lee

ABSTRACT

The purpose of this project is to create an autonomous laser locking system for a robot that will be used in the Multi Autonomous Ground-robotic International Challenge (MAGIC). Locking onto a target has many applications in robotics. The laser could be replaced by a flashlight, a camera, a projectile launcher, etc. Solving this problem requires the use of coordinate transformation matrices to deal with multiple reference frames. It also requires sensor analysis to determine positions of both the robot and the target. In this paper I describe an approach to solving this problem.

1. INTRODUCTION

In many robotics applications, it is important to have the ability to lock onto a target. For example, a robot that has a camera on it might be more useful if it could keep the camera pointed at an object of interest while the object is moving. The target locking system could be used for a number of things such as a laser pointer, a flash light, or a missile.

In general, for something to remain pointed at an object in three dimensions, it must have two degrees of rotational freedom. This allows it to remain locked onto the target regardless of where the robot is - or how it is oriented.

This paper presents my results of integrating a laser pointer locking system into an autonomous ground vehicle. The direction of the laser is determined by the angle of each gear. In order to keep the laser locked onto a target, the angle of each gear must be continuously calculated as a function of the robot's orientation and position with respect to the location and motion of the target.

2. BACKGROUND

2.1 Simultaneous Localization and Mapping (SLAM)

SLAM is an algorithm used in robotics to map an unknown environment while at the same time maintaining an estimate of current position. When these processes occur concurrently, the error in estimation converges [1]. This algorithm requires input from sensors, some of which are described in this paper. A 3D map resulting from a SLAM algorithm is shown in Figure 1.

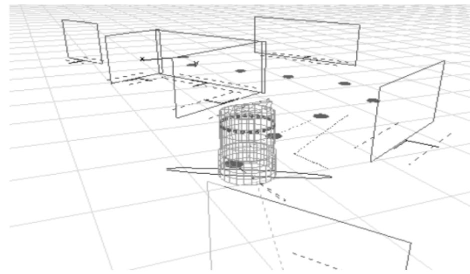

Figure 1

Real-time SLAM visualization by Newman et al [2]

2.1.1 Accelerometer

Accelerometers measure acceleration. Most methods involve a linearly elastic material (F=kx). In order to convert the mechanical motion into an electric signal, components such as piezoresistors or capacitors are used. A piezoresistor's resistance depends on the stress applied to it. The voltage across a capacitor is inversely proportional to the separation of the conducting plates. In robotics applications, three accelerometers – ideally positioned perpendicularly to one another – are required to obtain acceleration in all three dimensions.

2.1.2 Gyroscope

Gyroscopes measure angular velocity. One method of doing this is by taking advantage of angular momentum conservation. A heavy disk spinning at a high frequency resists change in angular momentum. When this disk is mounted on low friction bearings that have freedom to rotate along three linearly independent axes, the external torque of a moving object applied to the spinning disk is minimized. The result is that the axis of rotation of the disk remains fixed. Another method is a vibrating structure gyroscope. The physical principle is that a vibrating object tends to keep vibrating in the same plane as its support is rotated. A third more precise and also more expensive method takes advantage of light interference in a coil of fiber optic cable.

2.1.3 Light Detection and Ranging (LIDAR)

LIDAR works along the same principles as RADAR with the difference being the wavelength of radiation emitted. Light is sent out and scattered when it reaches an object. Some of this light is scattered exactly back in the direction of the LIDAR sensor. The sensor calculates the distance to the object based on the time it took for the light to return. It does this for many angles in a plane. To give an idea, the LIDAR we used returns an array of distances for 1,080 angles over a range of 270 degrees (90 degrees is cut off from the enclosure) at a rate of 40 Hz. LIDAR has problems with transparent objects such as glass because the light does not reflect.

2.1.4 Global Positioning System (GPS) Satellite Receiver

A GPS receiver works on the same principles as LIDAR: the time light takes to reach an object determines the distance. One difference is that LIDAR is used as both the source and the receiver of the light. The way GPS works is that a satellite acts as the source and sends timestamp information with the light. One source, however, is not enough to determine a unique position. If all that is known is the distance to the satellite and the position of the satellite, the possible positions of the receiver would include all points on the surface of a sphere centered around the satellite with a radius equal to the distance measured. If one assumes that the receiver is on the surface of the earth, the possible positions would be the intersection of the sphere and the earth, which is roughly a circle (Figure 2, top). The intersection of three spheres would be two points (Figure 2, bottom). If these points are far enough apart, and the position of the receiver is roughly known, this could be enough information. Assuming perfect accuracy and precision, four intersecting spheres would determine a unique position in space. This could be 3 satellites and an ellipsoidal approximation of the earth, or just 4 satellites. As the number of satellites increases, the error due to inaccuracy and imprecision decreases. In general, a GPS receiver is able to receive a signal from at least four satellites and up to as many as twelve.

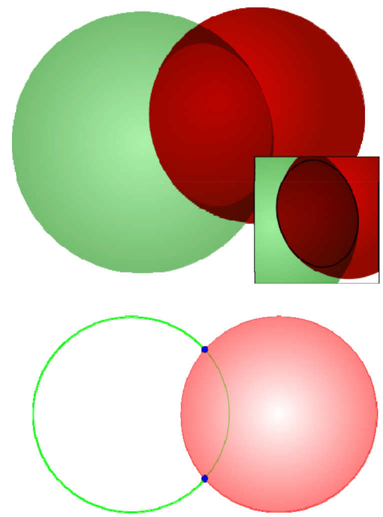

Figure 2

(Top) *Intersection of two spheres is a circle*

(Bottom) *Intersection of a circle and a sphere is 2 points*

2.1.5 Odometry

An odometer measures distance traveled by a wheel. This can be accomplished through optical or electromagnetic methods. The electromagnetic method involves two sensors attached to fixed points on the wheel with one magnet on the spinning electric motor. When the magnet on the motor passes one of the sensors, it causes a spike in voltage. The frequency of these spikes determines the angular speed of rotation. The second magnet is used to determine direction of rotation, which is determined by the order of spikes (i.e. magnet 1 then magnet 2, or magnet 2 then magnet 1). The optical method involves a light source, a photo sensor, and a perforated disk mounted to the motor. The frequency of spikes in the photo sensor is directly proportional to the angular speed of the wheel. Both techniques return an angular velocity of the wheel, but this alone is not enough to determine distance traveled. The diameter of the wheel must also be known. The diameter and the time integrated angular velocity of the wheel are enough to determine the distance travelled by a single wheel.

2.2 Differential Drive

Knowing the distance traveled by one wheel of a vehicle is not sufficient for determining the change in position of the vehicle. If one wheel is travelling faster than the other, the resulting action of the vehicle will be to turn. If the vehicle has two wheels, the motion of the vehicle can be modeled as the center arc of the two arcs travelled by the wheels (Figure 3). If the vehicle has four wheels, it is necessary that they will slip, and so the two-wheel approximation is not as accurate.

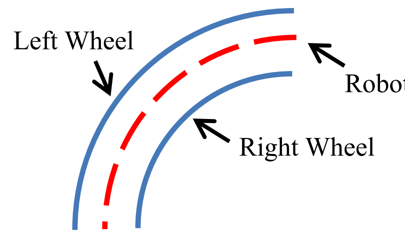

Figure 3

Modelling the motion of a two-wheeled robot based on the distance travelled by each wheel

2.3 Motion Planning

In robotics it is important to get from point A to point B in the most efficient way. Efficiency is determined by the cost of travelling the path. The cost can be a function of time, distance, terrain, etc. One algorithm of approaching this problem is called the A* Search Algorithm [3]. It works by finding the path that minimizes the cost. In order to do this, it must have a cost map to work with. This is obtained by SLAM, and any other cost modification relevant to the application.

2.4 Homogenous Transformations

Often it is convenient to describe various locations in different coordinate systems. An example is converting between a global coordinate system and individual local coordinate systems. To convert points between coordinate systems, transformation matrices can be used [4].

2.5 Proportional-Integral-Derivative (PID) Controller

A PID controller calculates an error value as the difference between a measured process variable and a desired set point. The controller attempts to minimize the error by adjusting control parameters. The proportional value determines the reaction to the current error, the integral value determines the reaction based on the sum of recent errors, and the derivative value determines the reaction based on the rate at which the error has been changing. The weighted sum of these three actions is used to adjust the process via a control element

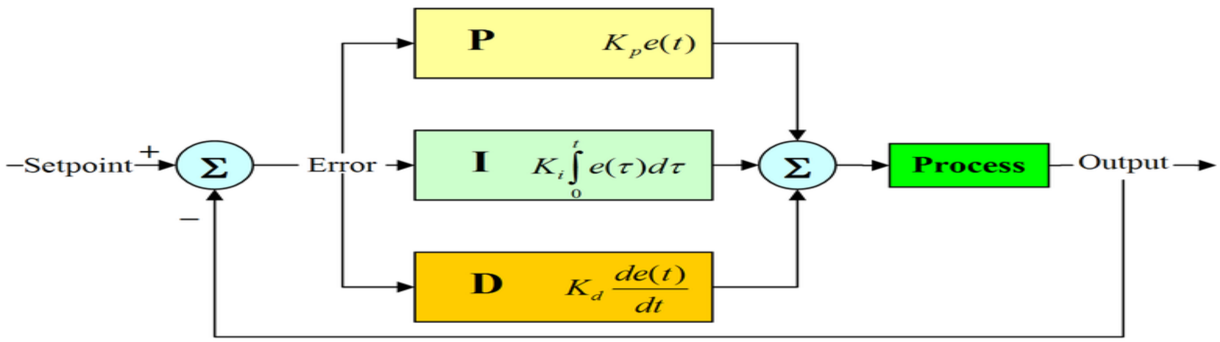

Figure 4

A block diagram of a PID controller

3. APPROACH

In order for the robot to point a laser at a target, the robot must know its own position and orientation. This task is more difficult than it might seem. A naïve approach would be to use only GPS. The problem with this is that GPS is only precise within about a half meter. Also, when a GPS receiver is near a building, it will report a false position due to multipathing which means that the satellite signal was reflected before it reached the receiver. A better method is to simultaneously map the robot's environment and localize it within that map also known as Simultaneous Localization and Mapping (SLAM). SLAM synthesizes various sensors including lidar, gyroscopes, and wheel encoders. The primary sensor is the lidar. An example of a typical lidar output is shown below:

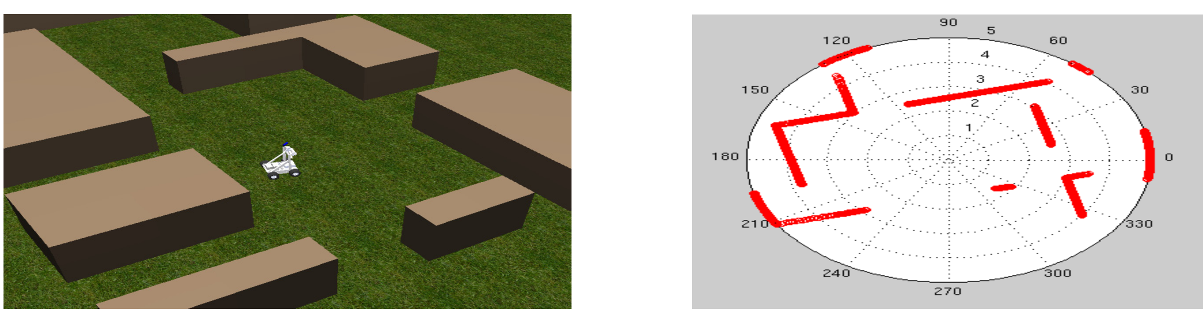

Figure 5
Left: robot in an environment
Right: lidar data of environment

SLAM works by adding each new lidar output to a collaborative map. If a robot were to drive inside a building, SLAM would build a map of the interior. In order to do this, SLAM must know how to add consecutive lidar maps. For example, if the robot turns, then the new map will different from the old one by a rotation. If the robot goes straight, the new map will be shifted backward compared to the old one. SLAM determines what the robot did between maps by using encoder and gyroscope data. Encoders give information about translation, while the gyroscopes give information about rotation. This information, however, is not absolute. SLAM makes small variations in rotation and translation to find a least squares fit.

For a laser to be able to lock onto a target that can move in three spatial dimensions relative to the laser, the laser must have two degrees of rotational freedom. This was accomplished by using 2 servos. A servo is basically a gear that can rotate to a specific angle. The angle is determined by the voltage applied to it. The servos we used can rotate between 0 and 300 degrees. When oriented so that one servo controls yaw and the other controls pitch, the resulting field of view is all points in space except for a 60 degree pyramid. It is shown in Figure 4.

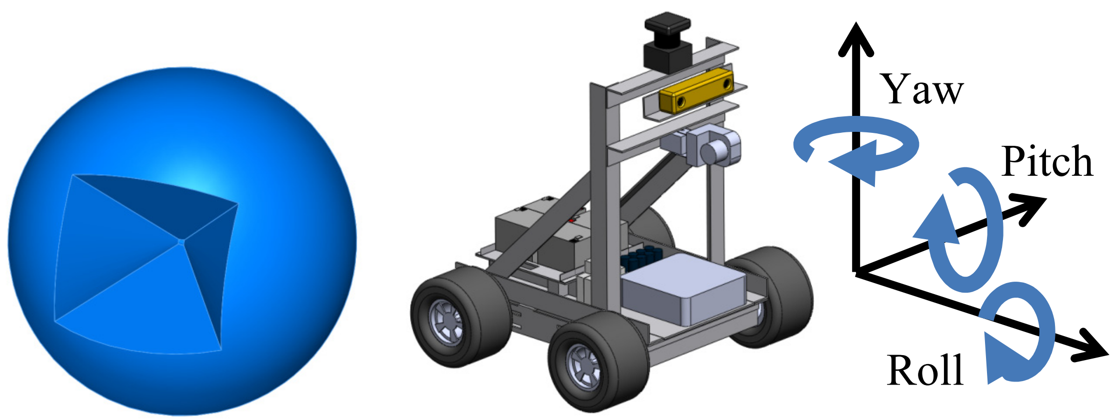

Figure 6

Left: Field of view of laser
Right: roll, pitch, and yaw w.r.t. the robot

The direction of the laser is determined by the angles of the servos. These angles need to be continuously calculated as a function of the robot's position and orientation, as well as the target's position and orientation. The first step I took was to find the target in robot coordinates, which is initially given in global coordinates.

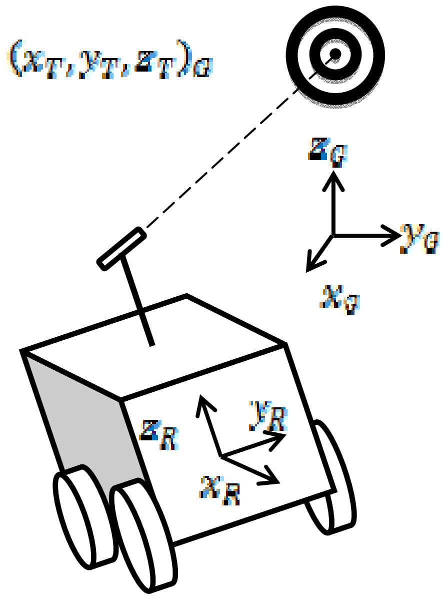

Figure 7

The target is given in global coordinates $(x_T, y_T, z_T)_G$

The goal is to convert the global coordinates into robot coordinates.

In robot coordinates, the x-axis is in the direction of motion, the z-axis is normal to the plane made by the 4 wheels, and the y-axis is to the left due to convention.

A straightforward way of converting points between global and robot coordinates is by using a transformation matrix. The way a transformation matrix works is that one first determines the series of rotations and translations of the original coordinate system required to match it up with the other coordinate system. Each rotation/translation corresponds to its own transformation matrix. The final matrix is calculated by multiplying the individual matrices in order. To match the global coordinate system up with the robot's coordinate system, the following transformations have to happen in order (use Figure 5 as a reference):

1. Translate along x_G axis to x coordinate of robot, along y_G axis to y coordinate of robot, and along z_G axis to z coordinate of robot
2. Rotate around the z_G axis the yaw of the robot
3. Rotate around the y_G axis the pitch of the robot
4. Rotate around the x_G axis the roll of the robot
5. Translate along x_G axis to x coordinate of the laser, along y_G axis to y coordinate of the laser, and along z_G axis to z coordinate of the laser

Multiplying these transformations together results in a matrix that will convert robot coordinates to global coordinates. The goal, though, is to do the opposite: convert global coordinates to robot coordinates. This matrix can be found by simply finding the inverse of the other matrix. The transformation matrix is shown in Equation 3.

$$T_{G\rightarrow R} = [\mathrm{Trans}(\mathrm{RobotPosition}) * \mathrm{Rot}_z(\mathrm{yaw}) * \mathrm{Rot}_y(\mathrm{pitch}) * \mathrm{Rot}_x(\mathrm{roll}) * \mathrm{Trans}(\mathrm{LaserOffset})]^{-1} \quad [1]$$

$$T_{G\rightarrow R} = \left(\begin{bmatrix}1 & 0 & 0 & x_R\\ 0 & 1 & 0 & y_R\\ 0 & 0 & 1 & z_R\\ 0 & 0 & 0 & 1\end{bmatrix}\cdot\begin{bmatrix}\cos(yaw) & -\sin(yaw) & 0 & 0\\ \sin(yaw) & \cos(yaw) & 0 & 0\\ 0 & 0 & 1 & 0\\ 0 & 0 & 0 & 1\end{bmatrix}\cdot\begin{bmatrix}\cos(pitch) & 0 & \sin(pitch) & 0\\ 0 & 1 & 0 & 0\\ -\sin(pitch) & 0 & \cos(pitch) & 0\\ 0 & 0 & 0 & 1\end{bmatrix}\cdot\begin{bmatrix}1 & 0 & 0 & 0\\ 0 & \cos(roll) & -\sin(roll) & 0\\ 0 & \sin(roll) & \cos(roll) & 0\\ 0 & 0 & 0 & 1\end{bmatrix}\cdot\begin{bmatrix}1 & 0 & 0 & x_L\\ 0 & 1 & 0 & y_L\\ 0 & 0 & 1 & z_L\\ 0 & 0 & 0 & 1\end{bmatrix}\right)^{-1} \quad [2]$$

Although calculating this matrix is complicated, the application is quite simple. To convert a point in global coordinates to robot coordinates, one simply needs to multiply the global coordinates by the transformation matrix.

$$\begin{bmatrix} x_R \\ y_R \\ z_R \\ 1 \end{bmatrix} = T_{G \to R} * \begin{bmatrix} x_G \\ y_G \\ z_G \\ 1 \end{bmatrix} \qquad [3]$$

R = robot
G = global

To switch from robot coordinates to global coordinates, multiply by the inverse:

$$\begin{bmatrix} x_G \\ y_G \\ z_G \\ 1 \end{bmatrix} = (T_{G \to R})^{-1} * \begin{bmatrix} x_R \\ y_R \\ z_R \\ 1 \end{bmatrix} \qquad [4]$$

Notice that when the robot moves the transformation matrix changes. The matrix must be recalculated every time new information about the robot's position and orientation are received.

Once the target is known in robot coordinates, the angle of the horizontal/yaw servo can be calculated. The requirement is that the plane of the vertical/pitch servo be lined up with the target.

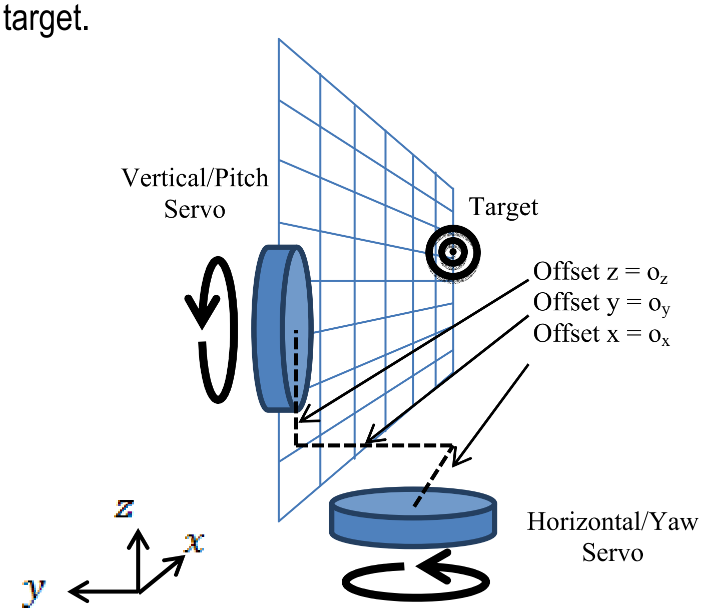

Figure 8

The sensors do no rotate around the same point, and so calculating the angle of each requires the offset from one servo to the other.

The horizontal angle can be found by first calculating the angle as if there were no offset, and then making a correction to compensate for the offset.

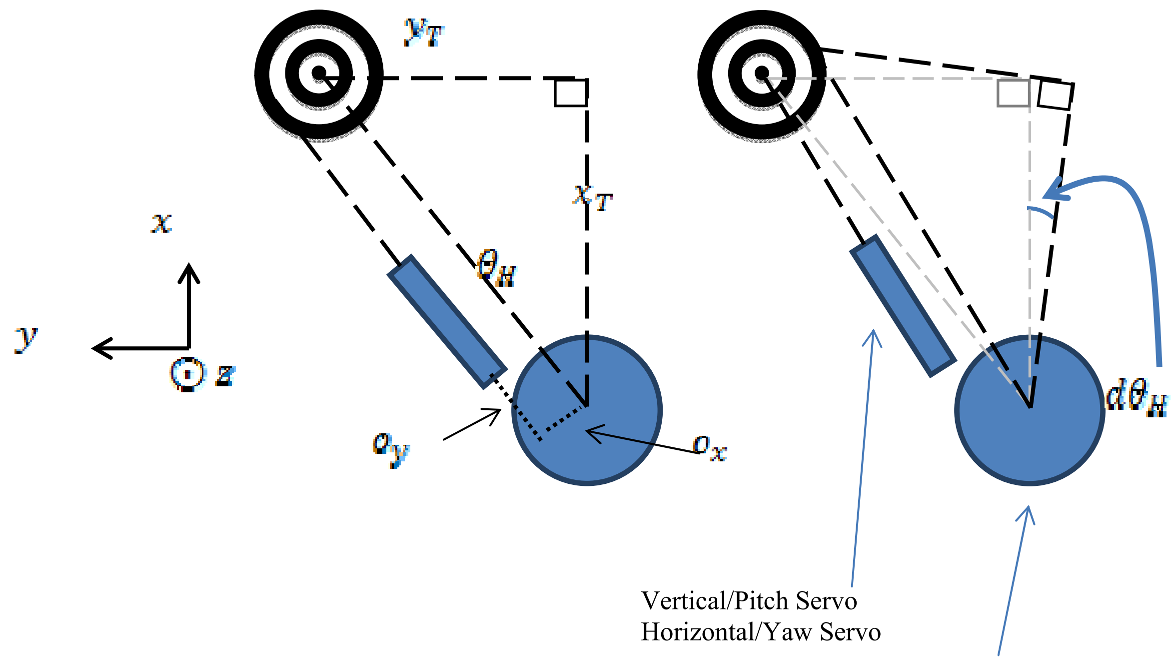

Figure 9

Calculating the required angle of the horizontal/yaw servo to align the pitch servo's plane with the target. It requires a small correction $d\theta_H$

$$\theta_H = \arctan\left(\frac{y_T}{x_T}\right) \qquad [4]$$

$$d\theta_H = \arcsin\left(\frac{o_y}{\sqrt{x_T^2+y_T^2}}\right) \qquad [5]$$

$$\theta_H = \theta_H - d\theta_H \qquad [6]$$

Notice that if the y offset is zero, then no correction needs to be made. Also there is no dependence on the offset which is in the direction of the laser (x offset).

Now, the vertical angle needs to be calculated. The first step I took in doing this was to create another coordinate system centered on the pitch servo. This means another transformation matrix is required to find the coordinates of the target in this new coordinate system.

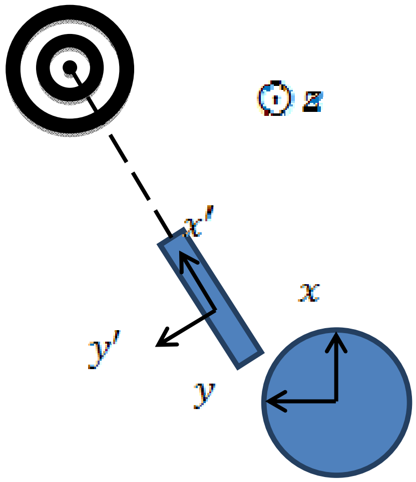

Figure 10

The new coordinate system is different from the old one by a translation equal to the distance between the center of the horizontal/yaw servo and the center of the vertical/pitch servo. Also there is a rotation equal to the angle of the horizontal servo θ_H

$$T = [\mathrm{Trans}(\mathrm{ServoOffset}) * \mathrm{Rot}_z(\theta_H)]^{-1} \qquad [7]$$

Finding the angle of the vertical/pitch servo now is easy.

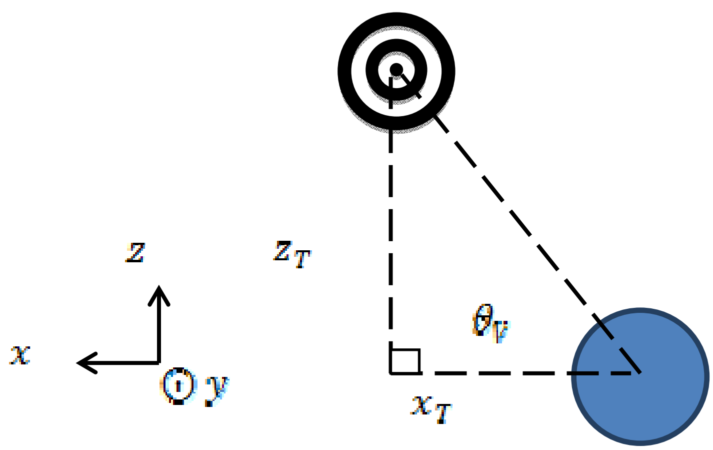

Figure 11

Calculating the angle of the vertical/pitch servo is straightforward after the coordinate transformation

$$\theta_v = -\arctan\left(\frac{z_T}{x_T}\right) \qquad [8]$$

Although these equations allow the laser to accurately point at a target, they do not take into account the relative motion between the target and the robot. There are two problems that occur with setting the angle of each servo.

1. The angles of the servos are updated at discrete time intervals which causes the laser point to be unsteady

2. The servos are designed such that when a target angle is set, the servo comes to a complete stop at the target angle. When the target angle is constantly changing, the servo never reaches it.

The solution to the first problem is to make the servo's motion more continuous. There are two ways of approaching this problem:

1. Increase the frequency at which the target command angle is sent
2. Send angular velocity commands instead

The first option will not work in our case due to the fact that the position and orientation information updated at 40 Hz, and this is limited by the angular velocity of the lidar. Most often, the target angle changes because the position and orientation of the robot change. Increasing the target angle command rate to 400 Hz would mean that the same target angle command would be sent 10 times. The second option is reasonable and it also solves the second problem. Sending angular velocity commands requires calculating the desired angular velocity or angular acceleration. I wrote a PID controller to do this. The controller looks at the difference between the desired angle and the target angle and sets the angular velocity accordingly.

4. RESULTS

The autonomous laser locking system was tested with a robotics simulator.

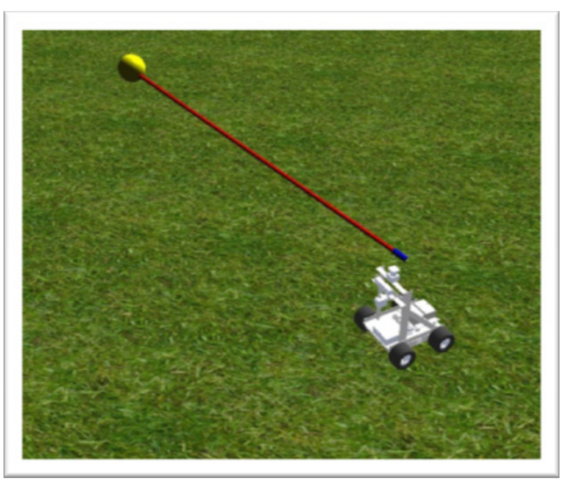

Figure 11 (left)

The autonomous laser locking system was tested with a physics simulator. The model of the robot was imported from SolidWorks. In the simulator, the yellow ball moves while the robot drives around. The laser remains pointed at the target.

Figure 12 (right)

The laser is targeting the center of the red bin.

5. CONCLUSIONS

In order to create a laser locking system, the following steps were taken:

- Estimate position
- Receive target in global coordinates
- Calculate target in robot coordinates
- Calculate angles of servos
- Do PID control on angle error to obtain an angular velocity
- Repeat

6. RECOMMENDATIONS

The servos are currently controlled with angular velocity commands. It would make more sense to control them with angular acceleration commands because acceleration can change almost instantaneously whereas velocity cannot.

ACKNOWLEDGEMENTS

I would like to thank:

- Professor Dan Lee (research advisor)
- Alex Kushleyev (graduate student in lab)
- Dr. Jan Van der Spiegel (Sunfest coordinator)
- National Science Foundation

REFERENCES

[1] Durrant-Whyte, H. and Bailey, T., “Simultaneous Localization and Mapping (SLAM): Part I The Essential Algorithms,” *Robotics and Automation Magazine*, 2006

[2] P.M. Newman, J.J. Leonard, J. Neira, and J. Tardos. “Explore and return: Experimental validation of real time concurrent mapping and localization”. *Proc. IEEE Int. Conf. Robotics and Automation*, 2002

[3] PE Hart, NJ Nilsson, B Raphael, “A formal basis for the heuristic determination of minimum cost paths”. *IEEE transactions on Systems Science*, 1968

[4] Jennifer Kay. “Introduction to Homogeneous Transformations & Robot Kinematics.” *Rowan University Computer Science Department*. January 2005

Pediatric Dynamometer Using Piezoresistance Sensor

NSF Summer Undergraduate Fellowship in Sensor Technologies
Logan Osgood-Jacobs (Engineering) – Swarthmore College
Advisor: Dr. Jay N. Zemel

ABSTRACT

External forces on the body have long been known to have a large effect on children's bone growth and development. Researchers at Children's Hospital of Philadelphia (CHOP) want to explore this relationship. However, there is no current technology that directly measures the forces applied to the body. Dr. Babette Zemel, from CHOP, and Dr. Jay Zemel, from ESE at Univeristy of Pennsylvania, have been developing an in-shoe physical activity dynamometer (FootPAD), which will directly measure forces felt through children's feet. The past versions of this device have been developed using piezoelectric sensors; however, the drift caused by temperature changes in the shoe was unacceptable. This study looked into using piezoresistance sensors in the device instead of the piezoelectric ones. Preliminary tests with the sensors showed that they did not have the same temperature problem and that the sensors could accurately measure changes in force within the 10% accuracy needed. A circuit for the device using these sensors was designed and built, however further work with the software is needed before the device can be fully implemented and tested.

1. INTRODUCTION

According to a 1995 study by Riggs and Melton, bone disease causes fractures in approximately 1.5 million people each year. However, as the US population is growing older this number continues to increase.[1] The surgeon general's report on Bone Health and Osteoporosis predicts that by 2020 over half of Americans over 50 will be at risk of developing osteoporosis. Considering the increasing toll on the population, it is important to find the best way to prevent bone disease. Bone diseases decrease bone strength and increases fracture risk by impacting bone density, bone turnover, and bone structure.[2] Childhood is the primary time when bone is produced, making this age group the best focus for bone growth and development studies.[3] The stronger bones children develop the less risk of bone disease they face in the future.

A widely accepted model for the study of bone growth is the mechanostat theory, which predicts that bone size and mass will be impacted predictably by varying muscle force during growth. Studies of this effect have looked primarily at the correlation between exercise and bone development.[4] These studies have shown the importance of childhood exercise for strong bones throughout life.[3] However, it is difficult to directly measure the force of muscle on bone let along directly measure externally applied forces over time in humans. An example of the research needed is what aspect of applied forces has the greatest impact on bone growth and development, i.e is it the peak force, the total force, or the rate of loading that is important? With this information, researchers could develop an exercise regimen that could best improve bone strength.

Most studies have relied on parent and or child surveys, muscle measurement, or accelerometers to get information about the external forces experienced by the child.[4] However, survey data is problematic because it is subjective, and outside of extreme activity or inactivity it is difficult to get any accurate information about the intensity of activity. In addition, surveys provide little information about the actual external forces. Accelerometers are a valuable tool when looking at amount of activity. However, they are not capable of measuring static forces and do not take into account the force that would be added from carrying an object.[5] Many of these problems could be addressed by a pediatric dynamometer, which would be inconspicuous, e.g. in a child's shoe, and be able to continuously collect data about the forces applied to the user's feet and legs. This would address many of the previous technology problems and the data collected could examine what part of the force has the most impact on bone development.

2. BACKGROUND

Since 2004, SUNFEST fellows and University of Pennsylvania students have worked with Dr. Jay Zemel to develop a pediatric dynamometer. [6] The original design fit inside a child's shoe and was able to collect and store data over a reasonable period of time. However, the device used sensors of polyvinylidene fluoride (PVDF), a piezoelectric polymer film that produces a current proportional to the strain along the horizontal axis when the film is bent. However, it was not possible to get reproducible measurements with this sensor due an inconstant conversion from strain to the vertical force. A SUNFEST fellow in 2009 tried using a different type of piezorelectric sensor from Emfit Ltd. called a piezoelectret.[6] The electret principle uses dipoles induced across small air voids to generate a current when a vertical force compresses the dipoles in the air voids. Although these sensors were able to get reproducible measurements at a constant temperature, the sensor was temperature sensitive, causing a drift in the results that was unacceptable. To overcome this problem a less thermally sensitive sensor based on a "pressure sensitive ink" was selected to measure the force, the FlexiForce A201 force sensors shown in Fig. 1.[8] The FlexiForce A201 conductance changes linearly with the applied force (F). The linearity simplifies determining the force from a calibration since $F = k(1/R)$, where k is a constant and R is the measured resistance.

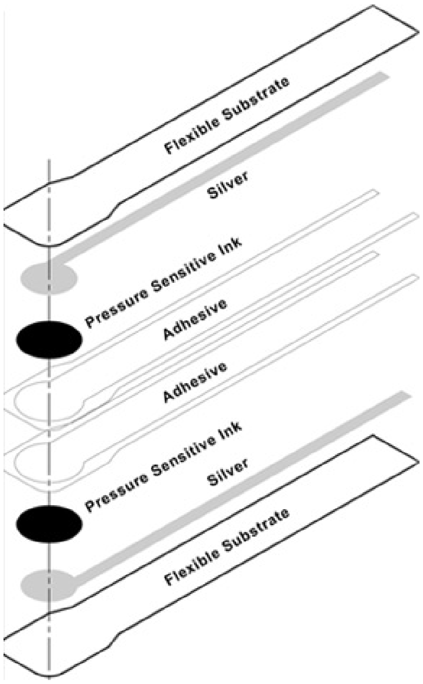

Figure 1: Construction of FlexiForce© A201 sensor. [8]

3. GOALS

The pediatric dynamometer is to be used by Dr. Babette Zemel, the Director of the Nutrition and Growth Laboratory at the Children's Hospital of Philadelphia, to study the impact of forces through the feet on child bone development. In order to directly measure the external forces on children's bones, a portable unobtrusive device that measures force needs to be developed. The pediatric dynamometer must fit inside a child's shoe, accurately measure the force, and collect and store the data over a reasonable period of time. The data are communicated to a computer using a standard RS232 cable when the measurement period is completed. Past projects have been able to create a device that was able to do all of these except accurately measure the force. In order for the device to work with the FlexiForce A201 sensors, the analog section of the device has to be redesigned. The goals for redesigning the device are as follows:

Modify the existing user interface to work with the new system.
Build a working circuit that is as small as possible.
Modify the existing microprocessor program to take the necessary data and relay it to the computer.
Calibrate the sensor.

4. DESIGN AND BUILD OF THE PEDIATRIC DYNAMOMETER

4.1 Device Overview

The device consists of consists of a dual operational amplifier chip, the OPA2237, a Reg710 3V voltage stabilizer, a PIC 18F14K50 microprocessor, and a Numonyx M25P16 flash memory. A schematic of the circuit can be seen in Appendix A. The switch from the piezoelectric to the FlexiForce A201 sensor required a different signal coupling circuit. The PIX 18F14K50 microprocessor controlled the operation, timing of the measurements, data acquisition and transfer, etc., as well as converted the analog signals from the two op amps to digital format. The Numonyx memory chip stored the digitized data on board the device until read-out. These components were selected to match those used in another device developed at Penn, the Neonur. This device measures pressure changes in a baby bottle.[9] Although the purpose of the Neonur is different from the FootPAD, the underlying circuitry using the microprocessor and memory chip is the same.

4.2 Basics of FlexiForce A201 Sensors

The FlexiForce sensor is composed of two layers of silver connected to pressure-sensitive ink. This pressure-sensitive ink is only in the circular end of the sensor, so this is the only area where force is sensed in the device. The pressure-sensitive ink acts as a variable resistor, while the silver layers extend to connectors that can plug into the device. The resistance varies linearly with the applied force and since V = IR , so does the voltage. Once the proportionality constant is found this can be used to calculate force as F=kV/I.

4.3 Circuit Design

Figure 2 FlexiForce sensor used in device.[8]

One of the goals of the project was to make the circuit as small as possible, however for testing a larger circuit was needed. The smaller circuit, which measures 1.23 in x 1.56 in, is shown in Appendix B. The larger circuit, shown in Appendix C, has wires attached at some of the vias to allow for easier testing.

4.3.1 Gain Circuit

The gain circuits for both sensors are set up as non-inverting amplifiers. Considering the variable sensor resistance as R_S and the load resistor as R_L the voltage in to the amplifier (V_m) is $\frac{R_l}{R_L + R_s} * 3V$ (1). The load resistor keeps the current drawn from the battery to a minimum. The value for R_L was decided by testing the gain circuit on a breadboard across a range of forces at varying resistances. The resistance of R_L=1000Ω was determined to be the highest resistance with a reliable output, drawing only 3mA of current.

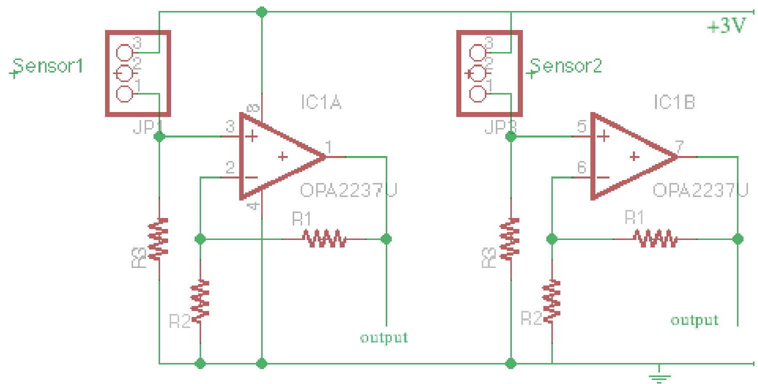

Figure 3 Gain circuit used in device.

A non-inverting operational amplifier configuration gives the equation $V_i = (\frac{R_1}{R_2} + 1)V_m$ (2). The microprocessor has an 8bit processing unit, meaning that it can operate with numbers up to 2^8 = 256. For the best resolution we want this to be equivalent to close to 2.56V. Based on data taken with the breadboard circuit without amplification, a gain of 17 was needed. This means that $\frac{R_1}{R_2} = 16$. Based on the resistors at hand, R_1 = 2430Ω and R_2 = 150Ω, giving a gain of 17.2. Saturation of the operational amplifier is not a concern because the same voltage input, 3V, to the sensor is used in the amplifier and the output has been set up to stay below 2.56V.

4.3.2 Voltage Stabilizer

A voltage stabilizer is critical for accurate results from the device. As seen in the equation 1, the voltage output (what is recorded from the sensor) is dependant on V_{in}. As the battery is drained V_{in} would decrease, causing a drift in the results. The voltage stabilizer prevents this drift from happening. Texas Instrument's Reg710 3V was chosen for the part. This allows for the battery to go down to 2.8V[10] and still produce a 3V input to the rest of the circuit. In addition this device works with as little as 10mA current.

4.3.3 Microcontroller and Flash Memory

The Microchip PIC18F14K50 is the microcontroller used in the FootPAD. This chip employs software generated with the MPLAB and the C18 compiler. This software, distributed by Microchip, enables software to be written in C for the device rather than the more difficult-to-understand machine code that microchips use.

In addition to having analog-to-digital conversion capabilities, the PIC18F14K50 can communicate with the computer via the RS-232 protocol. The RS-232 cable used allows the device to interface with the computer using a USB connection rather than a serial connection. To make the pins line up appropriately between the USB cable and the board, a connector as shown in Figure 4 is used to switch the pins. Also, the serial peripheral interface (SPI) mode enables 8bits of data to be transferred to and received from the flash memory simultaneously. Both the flash memory and microprocessor can run on single supply voltage and draw little current, thereby extending the battery life of the device.

4.3.4 Constructing the Board

The circuit board was cut using a new LPKF Promat® S62 circuit board plotter. This machine was new to the University. Therefore, a protocol was developed to take a design from an EAGLE plot to a cut board ready to be soldered. In order convert an EAGLE file to a finished board; a set of jobs was first created to export the correct files from EAGLE to be used in Circuit CAM. A procedure was then developed to import these files into Circuit CAM, create the correct paths for the machine to follow when cutting out the board, and export the file to the machine operational software, BoardMaster. The last part of the protocol is used to import the paths to BoardMaster and cut out the board with this program. Although the machine is more automatic than the previous version used, many quirks needed to be worked out before the board could be successfully cut. Once the board was cut, the components were then soldered on the board. However, due to the small size it was difficult to solder all of the components without creating a short circuit. Each component was checked and sometimes multiple versions of the board were made to ensure the connections were made correctly. The completed board is shown in Figure 4 with USB cable connector and a quarter for scale.

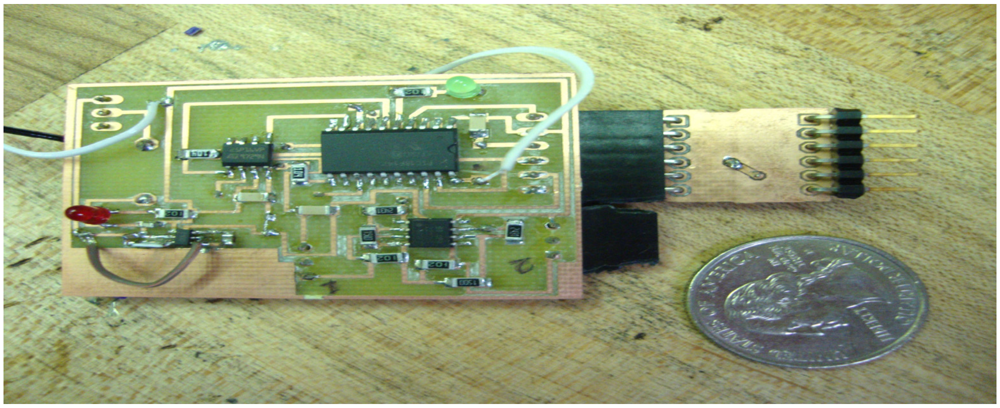

Figure 4 Finished circuit board.

4.4 Microcontroller programming

The programming used in this device is the same as that used in the Neonur.[9]

5. TESTING

Thus far we have not been able to get the fully implemented circuit to work consistently, so much of the testing has been done using a breadboard. With the breadboard circuit the voltage output from the amplifier could be directly measured, bypassing the need for any of the other components of the circuit design.

5.1 Verification of FlexiForce A201 Sensor Viability

Before the sensor could be implemented as part of the device, we needed to verify that it met the conditions needed. First, the sensor needed to be able to accurately measure force. Second, the sensor needed to not drift with changes in temperature at least between room temperature and around body temperature.

5.1.1 Accuracy

For the FlexiForce A201 sensor to accurately measure force it needed to have a consistent relationship between the voltage output and the applied force. According to the manufacturer, there should be a linear relationship between force and voltage output. To test this the voltage output was measured at varying forces. The force was measured using a scale and the voltage output was measured using a voltmeter.

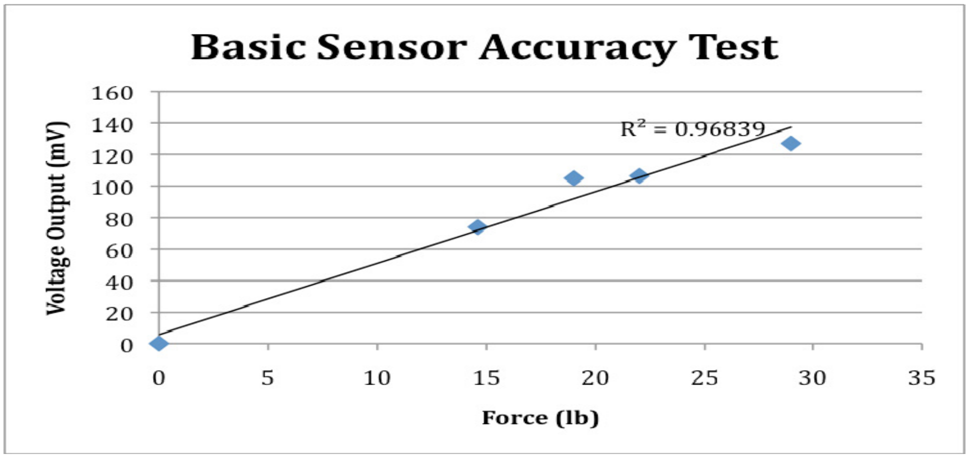

Figure 5 Test of sensor accuracy using voltage output from the sensor and the load resistor.

As shown by the R-squared value in Figure 5, the sensor is accurate within the needed 10%
.

5.1.2 Temperature Sensitivity

In order to test the temperature sensitivity, the force was kept constant while an object placed under the sensor heated up. Throughout the test, which went to a temperature slightly higher than body temperature, the output voltage only varied .05%. This shows that the FlexiForce A201 sensors successfully avoids the main problem encountered with the piezoelectric sensor used in earlier models.

5.2 Preliminary Device Tests

The working circuit was tested against a force plate. The force plate, used by CHOP, is known to be very accurate. The device was placed on top of the force plate and stepped on one time. The reading from the force plate is shown in the top of Figure 6 and the reading from the FootPAD device is shown in the bottom of Figure 6.

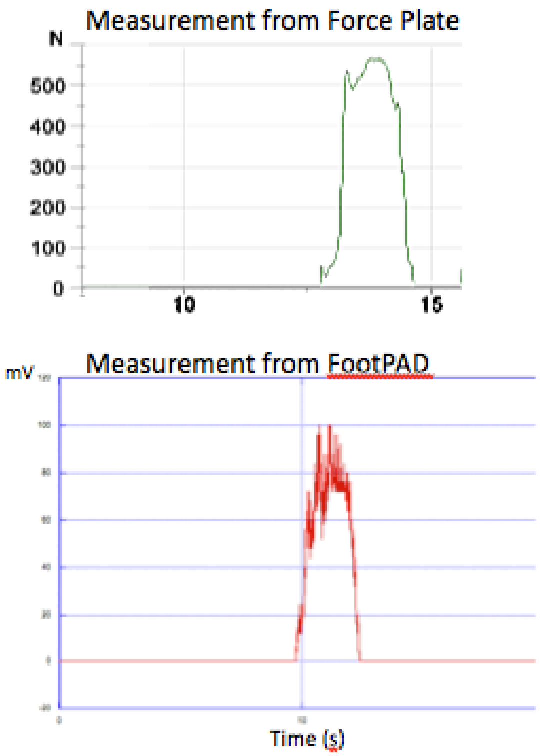

Figure 6 Step test as recorded by the force plate and the FootPAD.

The profile of the two recordings is very similar. This indicates that the device is working correctly and the potential to be calibrated with the force plate. It is important to note that the force plat is recording an average of the forces over the foot, while the FootPAD is recording only the point force acting on one area of the heel. This difference in measuring can account for the difference seen in the recording.

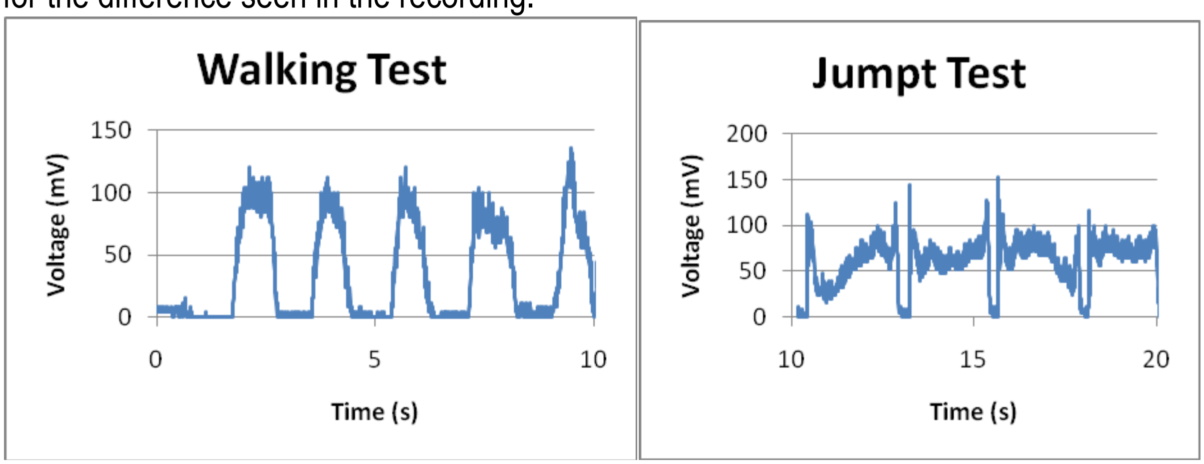

Figure 7 Voltage output data from walking and jump test performed with the FootPAD.

The other tests done with the FootPAD were a walking test and a jumping test. These were both done by having the device attached to the ankle of the tester and the sensor attached to the heel of the shoe. As can be seen in Figure 7, both of these tests gave results with consistent readings. In addition these tests were repeatable and the profiles. This consistency shows that the device will be able to accurately measure the forces applied to the load bearing bones.

6. CONCLUSIONS

Preliminary tests with the sensor on a breadboard demonstrated the viability of using a piezoresistance sensor for the FootPAD device. A circuit, which will be used in the device, was designed and built. A procedure for doing this completely in the lab was also developed. This procedure will make it possible for the device to be consistently reproduced and modifications made easily as needed when Dr. Babette Zemel is using the device. The preliminary tests show promise for the usability of the device as it is designed currently. However, much work is still needed before the device can be fully implemented.

7. FUTURE WORK

7.1 Software

Although the circuit is set up to work with two sensors, one at the ball of the foot and the other at the heel of the foot, the software can currently only read in one sensor. In order to get more accurate data this needs to be modified so that it can read from both sensors during the same trial.

7.2 User Interface

Currently data can be taken off of the device using either the graphical user interface developed for the Neonur or through the hyperterminal. It is important that the device be simple enough for anyone to use. The hyperterminal requires extra knowledge, so it is best if a person does not need to use this. Although the Neonur application is straightforward, it has extra functionality that is not necessary for this device and does not work with data coming in from two channels. It would be best if the user interface were created to only connect to the device, export two text files with the data in from testing, and allow for data collection with a real-time graph of the results.

7.3 Device Testing

Although the device is operational, it was not fully tested due to time constraints. The FootPAD now needs to be tested and calibrated. A past SUNFEST fellow[11] created a device meant to calibrate the FootPAD. This device uses a clock motor to cyclically load the FootPAD, imitating the loading present while walking. It is important to calibrate the device in order ensure accurate measurements. In addition, testing with the device in a shoe is important. This type of testing will show how the device works with the added heat and friction present in a shoe and the constantly changing loads while a person walks.

7.4 Shoe Integration

A key aspect for the device to be successfully used with children is that it be "invisible." For this to be true the device needs be integrated in a package that can be put in any sized shoe with padding, so that it cannot be felt. In addition it needs to be able to be easily removed and replaced, so that the parent or researcher can collect the data without the child noticing. If children are aware of the presence of the device they are likely to either play with it or change their habits.

ACKNOWLEDGMENTS

I would like to thank my advisor Dr. Jay Zemel. He has truly been a great mentor. He is always willing to help me and make sure I fully understand everything. I really appreciate his focus on learning over results. I would also like to thank Dr. Van der Spiegel. He has done an amazing job organizing the SUNFEST program with workshops and guest speakers throughout the summer.

I would also like to thank Sanket Doshi for all of his help with the programming, even as he was moving across the country. In addition, I would like to thank all of the SUNFEST and LSRM fellows for making this summer such a great experience. Lastly, I would like to thank the National Science Foundation for funding this program and making this amazing experience possible.

REFERENCES

1. US Department of Health and Human Services. *Bone Health and Osteoporosis: A Report of the Surgeon General.* Oct. 2004.

2. National Osteoporosis Foundation. *NOF – Bone Mass Measurement*. [Online]. Available: http://www.nof.org/osteoporosis/diseasefacts.htm.

3. International Osteoporosis Foundation. *Bone Development in Young People*. [Online]. Available: http://www.iofbonehealth.org/patients-public/more-topics/bone-development-inyoung-people.html.

4. S. L. Bass, P. Eser, R. Daly, "The effect of exercise and nutrition on the mechanostat," *J. Musculoskelet*. *Neuronal*. *Interact*., vol. 5, no. 3, pp. 239 – 254, Apr. 2005.

5. D. P. Cliff, J. J. Reilly, A. D. Okely, "Methodological considerations in using accelerometers to asses habitual physical activity in children aged 0-5 years," *J. Science and Medicine in Spor*t, vol. 12, pp. 557-567, 2009.

6. K. Gerasimowicz, *Pediatric Physical Activity Dynamometer.* SUNFEST 2009, Center for Sensor Technologies, Univ. of Pennsylvania, 2009.

7. A. A. Barlian, W. Park, J. R. Mallon, A. J. Rastegar, B. L. Pruitt, "Review: Semiconductor Piezoresistance for Microsystems," *Proc. IEEE Inst Electr. Electron Eng*, vol. 97, no. 3, pp. 513-552, Mar. 2009.

8. FlexiForce©, FlexiForce© Sensors. [Online]. Available: http://www.tekscan.com/flexiforce/flexiforce.html.

9. S. J. Doshi, *Neonur – System to Measure Neonatal Feeding Characteristics*. Thesis, Electrical Engineering Department, Univ. of Pennsylvania, 2010.

10. Reg710 Datasheet, Texas Instruments. [Online], Available: http://focus.ti.com/lit/ds/symlink/reg710-5.pdf

11. O. Tsai, *Dynamometer- The New Activity Monitor*. SUNFEST 2004, Center for Sensor Technologies, Univ. of Pennsylvania, 2004.

10. APPENDIX

10.1 Appendix A

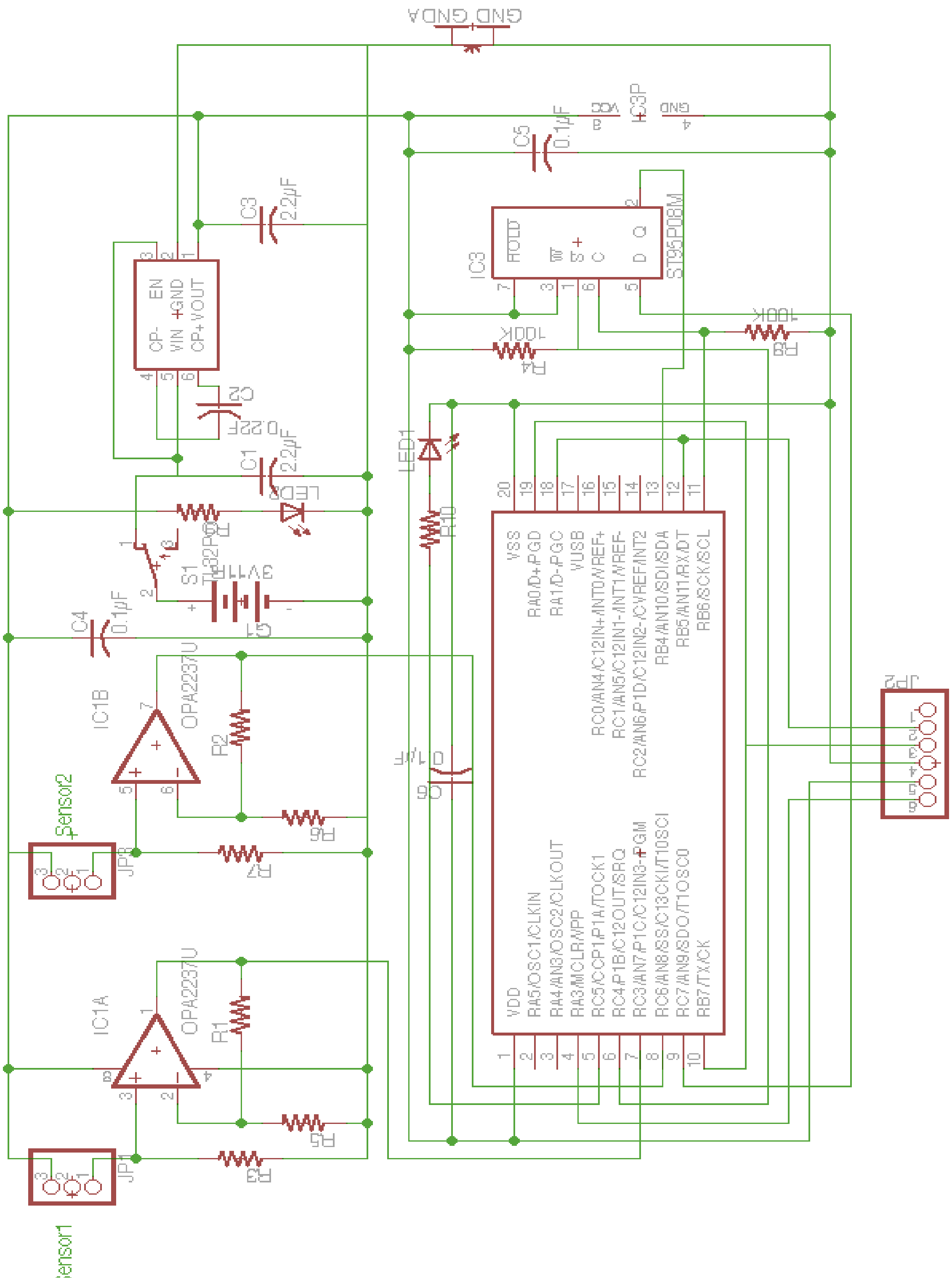

10.2 Appendix B

Top of Board

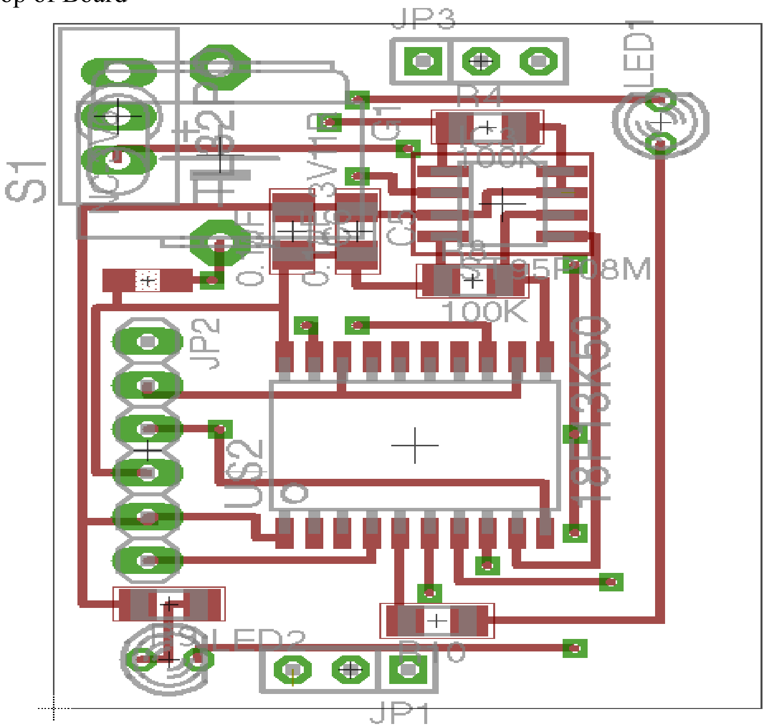

Back of Board

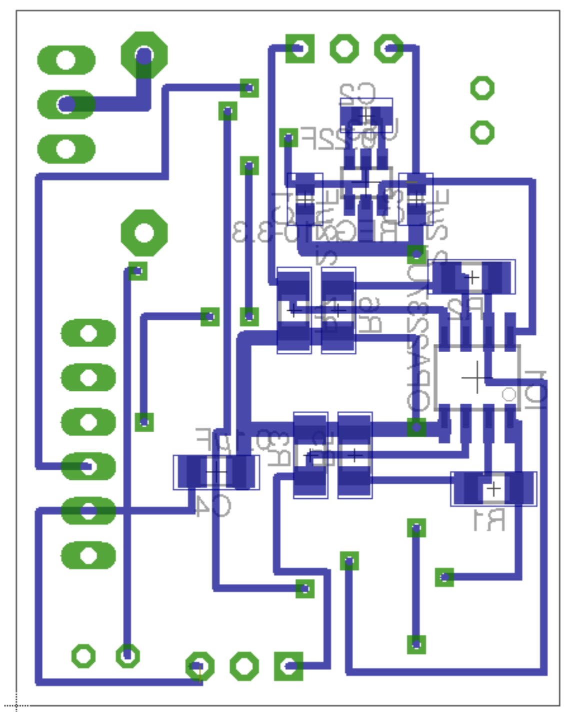

NAVIGATIONAL SENSING FOR THE EDUBOT

NSF Summer Undergraduate Fellowship in Sensor Technologies
Sriram Radhakrishnan (Electrical & Systems Engineering) – University of Pennsylvania
Advisors: Dr. Daniel E. Koditschek, Dr. Galen Clark Haynes

ABSTRACT

Automation – making a robot perform human functions but without human control – is the overarching goal of robotics. An important aspect of autonomous robots is the ability to detect and avoid obstacles. The goal of this project was to determine the feasibility of enabling a hexapedal robot, known as the EduBot, to generate maps of its surrounding area. This was accomplished by equipping the EduBot with a laser scanner, which was then controlled by the ROS robotic software package. The laser scanner was used to measure the distances to obstacles surrounding the EduBot. These measurements were then used by a ROS program to generate a map of the environment. The EduBot mapped various areas within a building to provide a large sample for analysis. These maps were then compared with the actual area to determine their accuracy. Once software and hardware errors discovered in early maps were corrected, the EduBot was able to generate accurate representations of its surrounding environment, thus allowing the EduBot to sense it surroundings. This suggest that autonomous navigation by the EduBot is possible.

INTRODUCTION

Every day, humans avoid obstacles as we navigate through the world. As this process is done subconsciously, we do not realize the complex calculations that are required to perform this task. Humans use sensory data from various organs to figure out a safe path between two points. This path is then updated as new obstacles are sensed.

As with humans, robots must be able to avoid obstacles. As robots slowly become more autonomous, they need to be able to deal with the physical objects in their surrounding area. [1] For example, when someone commands a robot to go through a dangerous building in search of something, that person does not know what is inside the building and what areas are navigable; the robot needs to figure that out for itself. In order for robots to perform the same task, they would need to have similar data, provided by sensors mounted on the robot. [1] Each sensor would measure something about the surrounding environment.

However, as Cmdr. H.R. Everett (U.S. Navy) writes, “There has been quite a tendency in many cases to oversimplify these issues, and assume that the natural growth of technology will provide the needed solutions.” [1] In other words, engineers have not devoted a great amount of time towards developing solutions for obstacle avoidance, something this project aims to do.

One of the most important senses is that of sight; to a robot, sight is essential to detecting obstacles. A robot sees by using a sensor to map the layout of its surrounding environment. This project deals with implementing a laser scanner on a legged robot to enable sight-based navigation. In addition, in order to simplify the software implementation of the laser scanner, a new robot software package was used, known as ROS (Robot Operating System). ROS was chosen because it contains many built-in programs that were useful in this project *(see Section 2.3)*. [2]

The Background section *(Section 2)* explains some of the concepts used in this project in order to give a better understanding of the procedures and results discussed in later sections. In addition, each subsection briefly explains the reasoning behind using that particular concept in this project.

Sections 3 and 4 present the methods used and the results gained from this project, as well as a discussion of these results. Sections 5 and 6 summarize the findings from this project, their consequences, and recommendations for future exploration of navigational sensing on the EduBot.

BACKGROUND

There are four main things necessary to implement an obstacle avoidance system in a robot: a robot, an object sensor, a software package that can control both the robot and the sensor, and positioning. Each of these items is described below.

The EduBot and the RHex Robotic Platform

RHex is a family of six-legged robots designed to travel on multiple terrains. [3] The robots use legs rather than wheels because legs are better able to adapt to changes in terrain. [4] The intent of the RHex project is to create a biologically-inspired robot that can be used in many applications, particularly in outside environments. [3] One of the many adaptations of the RHex platform is the

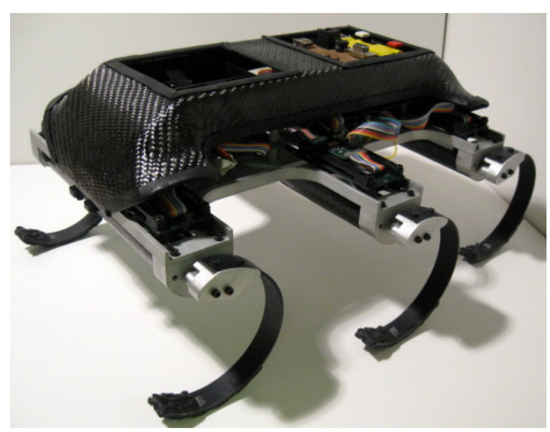

Figure 1: EduBot
(Source: KodLab Website, kodlab.seas.upenn.edu)

EduBot *(shown in Figure 1)*, which is primarily used for education and research. [3] This project aims to augment the capabilities of the EduBot by adding a laser scanner that can aid in autonomous navigation.

Light Detection and Ranging (LIDAR)

The key to avoiding obstructions is being able to sense them. This requires the use of a variety of sensors. These sensors must not only provide good data but must also work with the limited resources (e.g. power, space) available on a mobile robot. [1] Researchers are most interested in non-contact detection methods – ways of finding obstacles without actually touching them. [1] The most common sensors use either sonar or laser, each having its advantages and disadvantages. [1] A laser range finder has been selected for this project.

Light Detection and Ranging, or LIDAR, is a process whereby a laser beam is used to determine various characteristics of the surrounding environment. [5] A laser beam is aimed at a point in the world. The reflection of this beam is then sensed by a receiver. By comparing the transmitted beam with the returned beam, various characteristics can be measured of the point in space, including distance. Since a laser beam is pure in that it is composed of very few wavelengths, it performs well in sensing.

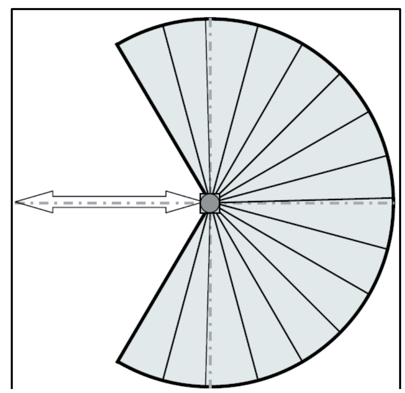

Figure 2: Hokuyo URG-04LX-F01 Laser Scanner
(Source: Hokuyo Automatic Co.)

The laser scanner used in this project contains a laser mounted on a rotating platform. By spinning this platform at high speeds, the laser scanner measures the distance to the nearest obstacle at all points in the angular range, as illustrated in Figure 2. The center point represents the laser scanner, while the shaded area shows the measurable area. This measureable area covers a range of 240^{o} around the laser scanner.

Robot Operating System (ROS)

The Robot Operating System, commonly known as ROS, is an open-source software package created for use on a variety of robotic platforms. [6] Being open-source, ROS is freely available for anyone to edit. This has led to the creation of numerous supplemental programs that add to ROS's functionality, many of which are used in this project. [2] ROS employs modular programming, a concept in which each part of a robot is controlled by a different program (called a node). [6] This way, it is easier to implement new features and add them to the existing ROS framework. This concept also simplifies the integration of ROS with the EduBot's existing software framework, and thus has been chosen for this project.

ROS employs a language-neutral interface for communication. [6] This interface consists of messages whose format is defined in a short text file listing the fields of the message. These messages are posted to topics, which are essentially message boards for ROS nodes. [2] Each topic contains information that a program has posted to it. For example, in this project, a laser scanner posts data gathered (i.e. distance measurements) to the *base_scan* topic. This use of messages and topics allows ROS to be, in theory, language neutral. This means that programs can be written in a variety of languages as each program is self-contained. All connections between nodes are handled through the language-blind message system, eliminating the need for programs to communicate with each other directly. In practice, four main programming languages are supported – C++, Python, Lisp, and Octave. [6] This project primarily uses Python, with a few programs written in C++.

The various programs in ROS are organized into stacks and packages. A package is a collection of programs and other code that work together to perform a certain task. [2] A stack, similarly, is a collection of packages that achieve a certain goal. [6] This project uses several ROS packages, such as the *gmapping* package for generating maps. The base ROS structure includes several tools to help with navigating through the ROS file structure, as well as error debugging and status checking. Since nodes in ROS are connected in a graph-like structure (i.e. with nodes connected together like a tree), one ROS tool, called *rxgraph*, displays a visual representation of the present ROS structure, including all running nodes and topics. [6] An example of this tool, adapted from the ROS tutorials, is shown in Figure 3.

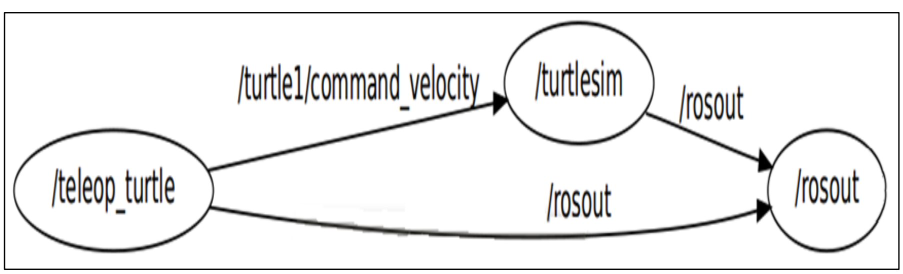

Figure 3: Example of the Graphical Representation of the ROS System Structure
(Source: ROS Tutorials, www.ros.org/wiki)

Each oval represents a ROS node, while each arrow represents a communication topic. The terminology explained in this section is used in later sections when discussing this project.

Positioning

In order to generate a map of its surroundings, a robot must be able to match each laser distance measurement with a point in space, typically denoted by using a traditional Cartesian coordinate system and a rotation angle. There are many methods of determining a robot's position, such as odometry and global positioning systems. [7] Because of its simplicity and relative ease of use, odometry has been chosen for this project *(see Section 2.4.1)*. In addition, the ROS mapping utility used to generate the map employs a method known as Simultaneous Localization and Mapping (SLAM) to correct some of the error inherent with odometry *(see Section 2.4.2)*.

Odometry

Odometry is a method of determining a robot's position relative to its starting point. By knowing, for example, the circumference of its wheel or its speed, a robot can be programmed to calculate how far it has moved. [7] In fact, odometry is the most commonly used method for robot positioning, as it is relatively simple and provides usable data for a low cost. [7] However, since odometry is based on the iterative summation of robot movements, a great deal of error occurs over time. [7] This error can be caused both by systematic discrepancies, such as an incorrect wheel circumference, and by non-systematic discrepancies, such as wheel slippage. While systematic error can be corrected by calibration, non-systematic error is much more difficult to fix. Therefore, while odometry allows for a general position, it cannot provide a specific position with only negligible error. For this project, however, the accuracy of odometry is sufficient, particularly as the ROS program used for mapping employs a process known as SLAM *(See Section 2.4.2).*

Simultaneous Localization and Mapping (SLAM)

Simultaneous localization and mapping (SLAM) is a technique to compute the current position of a robot relative to its starting position while generating a map of its environment. [8][9] As Sebastian Thrun writes, "The SLAM problem is generally regarded as one of the most important problems in the pursuit of building truly autonomous mobile robots." [8] The SLAM algorithm is based on two things: knowing the starting location of the robot, and being able to sense the surrounding environment. In this project, the starting location is assumed to be the origin, or (0,0). Sensing the surroundings of a robot is the primary goal of this project. The SLAM process relies on generating a map of the robot's surroundings and then figuring out the position of the robot using this map. As the robot moves, it gathers data regarding its surroundings from a sensor, which in this project was the laser scanner. The SLAM method compares successive sets of laser data (i.e. the laser view at point A with the view at point B), and analyzes the differences between them. For example, if the robot moved forward between points A and B, then the image of the environment at point B would be very similar to the image at point A, but the distances would be different to account for the robot's movements. Using these changes, SLAM can compute the change in the robot's position. Since each image is essentially a map, this process is also known as map matching. [7] The ROS *gmapping* program uses a combination of SLAM computation and odometry information from the robot to determine the robot's position relative to its starting point. [2] While SLAM is fairly accurate, it can fail if there is not enough laser data to compute a position change. In these instances, *gmapping* uses odometry to determine the robot's position.

EXPERIMENTAL PROCEDURES

The laser scanner used in this project was the Hokuyo URG-04LX-F01 Scanning Laser Range Finder *(shown in Figure 4)*. This laser scanner employs a Class 1 laser mounted on a spinning base, enabling scanning in a range of 240^{o} around the device. [10] It is powered by a 12VDC input.

Figure 4: Hokuyo URG-04LX-F01 Laser Scanner
(Source: Hokuyo Automatic Co., Ltd.)

To generate a map, the ROS gmapping utility requires two transformations between coordinate frames: *laser-to-robot* and *robot-to-odom*, where *odom* is short for odometry. The former accounts for the difference in position between the center of the laser scanner and the center of the robot, while the latter is the position of the robot determined using odometry. These transformations are recorded in ROS using the *tf* package, which contains code for publishing transforms to the *tf* topic using a uniform format.

In order to learn ROS and how the laser scanner worked, both were implemented using a wheeled cart and a laptop (to mimic a robot) before being implemented on the EduBot. Each of these implementations is explained in the subsections below.

Cart Implementation

A Lenovo ThinkPad T510 Laptop was used as the computational unit. The laptop was running Ubuntu Linux 10.04, on which ROS was installed. The laser was then connected to the laptop via USB, using drivers provided by the manufacturer. To emulate the EduBot, the laptop and the laser scanner were placed on a wheeled cart. The laser scanner was powered using a standard AC power adapter connected to an extension cord.

In the cart implementation, the *laser-to-cart* transformation was programmed with no shift, as the difference in position was not essential to accurate map building. For the odometry data, a Bash script was written so that the distance traveled could be easily input into the program. The script accepted changes in position using the arrow keys, each representing the appropriate direction (e.g. up key for forward, left key for left). When the script detected a key-press, it would update a ROS topic (named "position") with the new coordinates. Each key-press denoted a 0.1 meter shift in the given direction. To convert these coordinates to the appropriate transformation format, another ROS program was written that subscribed to the *position* topic, took the coordinate information, and published the transform using commands from the *tf* package. The script was written using the Bash scripting language, while the conversion node was written using Python. The program for the static *laser-to-cart* transform was written in C++.

The laser was connected to ROS using the *hokuyo_node* package, a built-in ROS interface for Hokuyo laser scanners. This package contains a ROS node, also called *hokuyo_node*, which converts raw laser data into ROS messages posted on the *base_scan* topic.

The cart containing the laser and the laptop was then taken to various locations within the University of Pennsylvania's engineering buildings. At each location, the transform and laser data were recorded (i.e. saved to a file) while the cart was moved around a small area. In each instance, the cart was moved along walls until the entire area was mapped. To ensure that the area was mapped in its entirety, the cart was moved in a loop.

After the first few runs, the *gmapping* utility was used to generate the maps. Generating the maps involved playing back the recorded laser and transform data while running the *gmapping* ROS node. These initial maps were not very representative of the measured area *(see Figure 7 in the Results section)*. To correct this error, settings regarding the accuracy of the odometry information were changed. These values, named *srr, srt, str, stt*, essentially told the *gmapping* utility how much to trust the odometry information, and were reported on a scale of 0.0 to 1.0, with 1.0 representing very poor accuracy. However, setting all four of these values to 0.9 did not considerably change the map *(see Figure 8 in the Results section)*. A review of the code and of the gmapping utility found that the angular position of the cart was not input correctly. Initially, the angular position of the cart (in the *cart-to-odom* transform) was set to 0 radians. As in the standard angular coordinate system, 0 radians represented the positive x-axis direction. However, the inputs to the odometry script were based on the fact that the cart was actually pointing in the +y-axis direction, or π/2 radians. The *cart-to-odom* transform was then updated with the correct angle. The resulting maps were much more representative of the measured area *(see Figure 9 in the Results section)*.

Initially, the manual odometry script only accepted inputs of forward, backward, left, and right. However, the EduBot is not a *holonomic* robot, meaning that it cannot move sideways; rather, it can only turn left or right. To account for this limitation, the script was updated to accept inputs for rotating left or right. Each time the appropriate key was pressed, the angular position would change by π/4 radians. This change enabled the cart to better mimic the EduBot, as well as to generate more complete maps *(see Figure 11 in the Results section)*.

EduBot Implementation

After understanding the laser scanner, the relevant ROS programs, as well as ROS itself, we moved to the EduBot. All the experiments in this project were conducted on the EduBot known as *Penn3*. The EduBot was powered using a 14.8V, 1320mAh lithium-polymer battery. The EduBot was controlled by a built-in CPU and ran Ubuntu Linux 8.04. The laptop (Lenovo ThinkPad T510) was used to connect via SSH to the EduBot over a Wi-Fi connection. This connection was executed both through a Linksys access point as well as through an ad-hoc connection. The ad-hoc connection, which connected the laptop directly to the EduBot, later became necessary since mapping occurred in areas out of range of the access point.

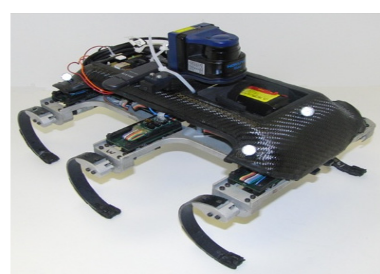

Figure 5: EduBot with Mounted Laser Scanner

To power the laser scanner on the mobile EduBot, the 12V port on the EduBot's battery management board was used. A connector was fashioned using a standard male AC adapter plug with two wires on the other side. These wires connected to the EduBot, while the adapter plug connected to the laser scanner. The laser did not greatly affect the battery life on the EduBot. The EduBot draws approximately 30W when walking and 10W when stopped, while the laser draws approximately 4.4W [10]. This additional power draw from the laser decreased the battery life by about 20%, according to calculations. While the calculated run time of the EduBot for pure walking was about forty minutes, the calculated run time with the laser on only decreased to about 33 minutes. In practice, battery life was not an issue, as each mapping run took less than fifteen minutes. In addition, to ensure sufficient voltage, each mapping run was executed on fully-charged batteries. The laser itself was mounted on the EduBot shell using cable ties and electrical tape *(see Figure 5)*.

Due to limitations of the laser scanner driver used on the EduBot, the laser scanner was connected to the laptop using a USB cable as before. While this kept the laptop tethered to the robot, mobility was maintained by placing the laptop on a cart. In addition, ROS was unable to be installed on the EduBot since its on-board data storage space was insufficient. The EduBot used a 2GB compact flash card, while ROS itself requires more than 1GB. While a bigger card was tried, there were unsolvable issues with booting to the new card.

As with the cart implementation, a program was needed to compute the position of the EduBot using odometry. The EduBot uses a software package called Dynamism. Dynamism is a lightweight, real-time robot control environment used to control the EduBot platform. [11] Dynamism allows a computer to interface with the EduBot to acquire data, such as speed settings, using either Python or C++ commands. The speed of the EduBot is reported using an arbitrary scale with positive numbers incremented by one-tenth. A speed of 1.0 was chosen for its relative stability and steady movement. At this setting, the actual speed, in cm/s, of the EduBot was measured. After taking several measurements in different environments, an average speed of 0.15 meters per second was found. While the EduBot can both turn-in-place and turn while moving, only turning-in-place was used, since the EduBot did not have a consistent angular speed when turning while moving. For turning-in-place, the EduBot has only two speed values: 1 and -1. Because the odometry would be calculated using time, the turning speed was measured in radians/sec, and was approximately $\pi/8$ radians per second. This was not a very accurate measurement however, and in practice, turning required some manual adjustments.

Using these speed measurements, an odometry node was programmed in Python for use with ROS. This node interfaced with Dynamism on the EduBot and queriedDynamism for the values of the speed and turn variables. Based on the value of each variable, the node adjusted the coordinates of the EduBot accordingly. Once this node was programmed, it was tested for accuracy. As soon as the program was run, however, the EduBot would crash, apparently because it was unable to handle both motor control and transmitting data to the computer. After some trial and error, the node was rewritten to use a different command to read in the variables. This command specified the time interval between variable reads, thus reducing the speed of reading. After setting this value at one second, the EduBot performed without any problems. This interval was then reduced to 0.5 seconds for better positional accuracy.

Another ROS node was programmed for the transformation between the laser frame and the EduBot frame. As stated in Section 3.1, this transformation was ignored in the cart implementation as it was not important. With the EduBot, however, this is crucial to ensure that the distance measurements are from the point of view of the EduBot. This difference in position was measured to be -0.04 meters in the x-axis and -0.11 meters in the z-axis. As the laser was mounted in the center of the robot, there was no change in the y-axis.

The EduBot was then taken to various areas to map the environment. The mapping process itself was fairly simple. Since odometry data was automatic and did not have to be entered manually as with the cart implementation, there was little user input necessary to acquire the odometry and laser data other than to control the robot. The robot was controlled using a Logitech joystick pad, with buttons for functions such as calibrate and stand, as well as control sticks for walking and turning.

The major problem found during mapping was with connectivity. At random times while mapping, the laptop would lose connectivity with the EduBot, thus requiring a full reset of the robot and starting the mapping process again. Initially, this was thought to be a problem with the CPU, in that the CPU would randomly reset itself. However, further examination revealed that the wireless card used for Wi-Fi connectivity on the EduBot was the cause of the problems. While removing the card and plugging it back in restored the connection, this was unfeasible as it required input using a keyboard and a monitor, which are unavailable when away from the lab. The problem was eventually attributed to poor USB ports on the EduBot. A new wireless card was attached to the EduBot using a USB extender, which seemed to work better. In addition, two batteries were used instead of one to better maintain the voltage necessary to run the robot.

As the EduBot moved forward, it would turn slightly and not go straight. In order to easily correct this, the EduBot odometry program was updated to allow for minute turning adjustments while moving without changing the position angle. While this change made turning possible only when stopped, it was necessary to ensure a higher accuracy for the odometry data.

Because of the lesser accuracy of the EduBot odometry data compared with the odometry in the cart implementation, the quality factors (i.e. the parameters of the ROS *gmapping* program) were set at 0.7 for all the maps taken with the EduBot.

RESULTS

In the cart implementation, maps were taken in two main locations within the School of Engineering: Berger Auditorium Lobby in Skirkanich Hall (referred to as Berger) and the Graduate Research Wing 3rd Floor Elevator Lobby in the Moore Building (referred to as GRW). For comparison with the maps, a picture of the GRW area is shown in Figure 6, while the Berger area is shown in Figure 10. Initially, as stated above, the angular position was not set correctly. This resulted in a very poor representation *(see Figure 7)*. This poor quality was also not noticeably affected by changing the odometry accuracy settings in the *gmapping* program *(see Figure 8)*. Once the angular position was corrected, the resulting map was a much better representation of the actual area *(see Figure 9)*.

Figure 6: The Mapped GRW Area

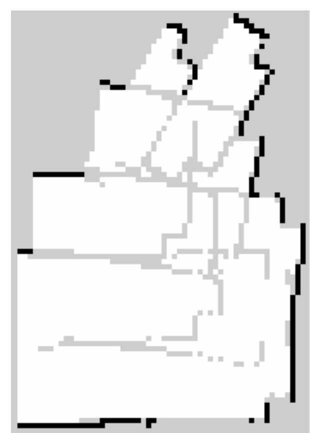

Figure 7: Map before any Correction (Location: GRW)

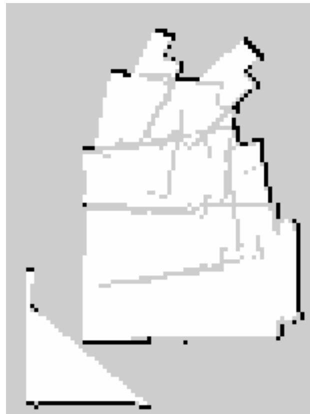

Figure 8: Map with Changed Accuracy Settings (Location: GRW)

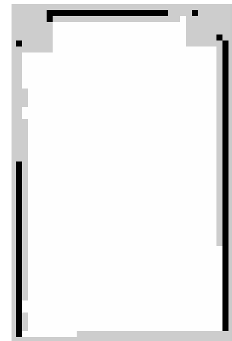

Figure 9: Map after Angular Position Fix (Location: GRW)

After the cart's odometry script worked for simple movements, the ability to rotate was added, resulting in the map shown in Figure 11. This map increased the accuracy of the map, since laser data were gathered for areas all around the cart, instead of just in the laser's measurable range *(see Figure 2)*.

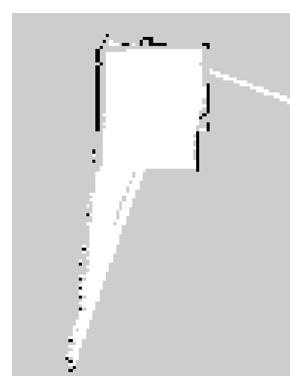

Figure 10: The Mapped Berger Area

Figure 11: Map after Rotation Feature Added (Location: Berger)

After the cart implementation was successful, we moved to the EduBot. Because of various connectivity and power problems encountered *(see Section 3.2)*, each map took much more time to produce. However, because of the mobility of the EduBot, much larger areas were able to be mapped.

The primary mapping location for the EduBot was a hallway in the Towne Building *(shown in Figures 12, 13, and 14)*. A map of the area shown in Figure 12 was taken first *(see map in Figure 15)*, followed by the entire area shown in Figures 12, 13, and 14 *(see map in Figure 16)*.

Figure 12: Mapped Area in Towne Building Hallway (Part 1, front)

Figure 13: Mapped Area in Towne Building Hallway (Part 2, back-right)

Figure 14: Mapped Area in Towne Building Hallway (Part 3, back-right)

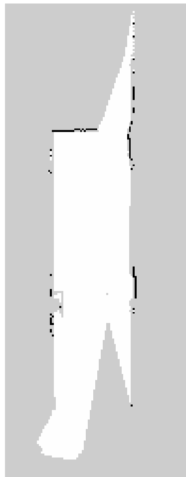

Figure 15: Map of Area in Figure 11

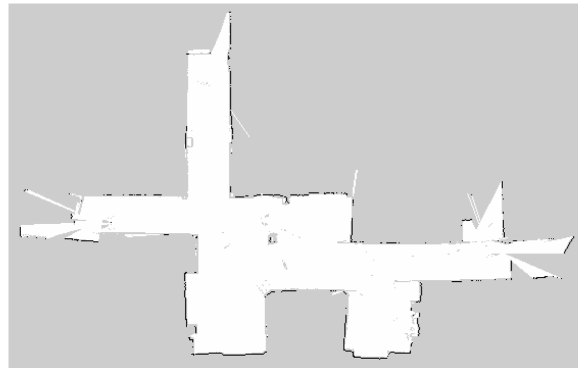

Figure 16: Map of Entire Towne Building Hallway from Figures 11, 12, and 13

As shown in Figures 15 and 16, the maps generated using the EduBot are a good representation of the actual area. The points where the map becomes inaccurate (e.g. on the top and bottom of Figure 15, as well as on the very left and right portions of Figure 16) are due to those areas not having any walls or other obstacles to sense. Thus, the laser scanner did not gather any data about those regions.

DISCUSSION & CONCLUSION

The purpose of this project was to determine the feasibility of using a laser scanner mounted on a robot to map out an area. Using a commercially available Hokuyo laser scanner, we mapped various indoor areas, first using a wheeled cart and then using the EduBot. Initially, these maps were very unrepresentative of the actual area, owing to various errors in programming, as shown in Figures 7 and 8. These errors were fixed in the cart implementation, resulting in good quality maps *(Figure 9)*. The EduBot implementation was more complex, as it required more programming to integrate the ROS programs with the EduBot's own software. We faced some issues with inaccurate odometry, as was expected from Everett, et al.'s statements [7]. However, the resulting maps were a relatively good representation of the mapped area *(Figures 15 and 16)*. These maps suggest that they can be used with programs such as the ROS stack navigation to allow for autonomous navigation.

RECOMMENDATIONS

Based on the outcomes of this project, further implementation of laser-based navigation can be attempted. ROS has a stack called *navigation* that uses transform and map data to navigate a robot to a specific pose. Since both transform and map data has been successfully gathered for the EduBot in this project, it may be possible to use the *navigation* stack with the EduBot. Before implementing, the maps should be more closely checked for accuracy to prevent the EduBot from crashing into obstacles. While the maps in this report were resized for space, in the original map files, each pixel represented 0.050 meters. Using this scale, comparisons can be made between distances from the map and measurements of the actual mapped areas. If these values match with negligible error, then the map can be deemed sufficiently accurate for use with autonomous navigation. While this method was used to check a few measurements on the maps, there was insufficient time to verify every distance. In addition to distance accuracy, taking several maps of the same area and comparing their relative accuracy would ensure that the mapping process can be repeated with equal accuracy.

There also might be ways to improve the odometry of the EduBot, both in the code and physically on the robot. The robot's gait was not perfectly straight and did slip, particularly during turns. Legs with better grip or a different gait may work better. Installing a sensor on the EduBot's legs to better compute distance traveled may also improve odometry. In addition, using a global positioning system will probably improve positional accuracy. Using a GPS would only be possible outdoors, but because of the relative unevenness of outdoor terrain, odometry would be even less reliable than indoors, thus making GPS a viable solution.

Another consideration is the amount of G-force felt by the laser. The laser scanner used in this project was specified to withstand only a certain amount of G-forces. While this was not a problem when testing in a flat indoor area, the EduBot may face strong forces when used in outdoor areas, such as a desert or a rocky terrain. Installing shock absorbers or in some way protecting the laser would be necessary to use the robot in such an environment.

Finally, while space limitations prevented installing ROS on the EduBot, this can easily be fixed by increasing the on-board disk space. Running ROS directly on the EduBot eliminates the need to tether the EduBot to the laptop for the laser, which would allow for easier mapping of large areas. This may also reduce the effect of connectivity issues between the EduBot and the laptop.

ACKNOWLEDGEMENTS

I would like to thank Professor Daniel E. Koditschek for giving me the opportunity to work in the KodLab this summer. I would also like to thank Dr. Galen Clark Haynes, Aaron Johnson, and B. Deniz Ilhan for all their help and advice throughout the course of my project. Finally, I would like to thank Professor Jan Van der Spiegel and the University of Pennsylvania for hosting and organizing the SUNFEST program, and the National Science Foundation for their continued financial support of the SUNFEST REU.

REFERENCES

[1] C. H. R. Everett, "Survey of collision avoidance and ranging sensors for mobile robots," *Robotics and Autonomous Systems,* vol. 5, pp. 5-67, 5, 1989.

[2] Willow Garage, "ROS Wiki," vol. 2010, 10/1/2009, 2009.

[3] KodLab. 2010, KodLab : Rhex. *2010(6/23),* Available: http://kodlab.seas.upenn.edu/RHex/Home.

[4] U. Saranli, M. Buehler and D. E. Koditschek, "RHex: A Simple and Highly Mobile Hexapod Robot," *The International Journal of Robotics Research,* vol. 20, pp. 616-631, July 01, .

[5] J. B. Campbell. 2007, "LIDAR," in *Introduction to Remote Sensin*g (4th ed.) Available: http://books.google.com/books?hl=en&lr=&id=r1JwIxMGYUAC&oi=fnd&pg=PR15&dq=LIDAR+introduction&ots=rT8SVk933M&sig=PtDQicu_ULkixyxMaRo0z5pVIiI#v=onepage&q=LIDAR%20introduction&f=false.

[6] M. Quigley, B. Gerkey and et al. ROS: An open-source robot operating system. Available: http://pub1.willowgarage.com/~konolige/cs225B/docs/quigley-icra2009-ros.pdf.

[7] J. Borenstein, H. R. Everett, L. Feng and D. Wehe, "Mobile robot positioning: Sensors and techniques," *J. Robot. Syst.,* vol. 14, pp. 231-249, 1997.

[8] S. Thrun, "Simultaneous Localization and Mapping," *Robotics and Cognitive Approaches to Spatial Mapping,* pp. 13-41, 2008.

[9] H. Durrant-Whyte and T. Bailey, "Simultaneous localization and mapping: part I," *Robotics & Automation Magazine, IEEE,* vol. 13, pp. 99-110, 2006.

[10] L. Hokuyo Automatic Co., "Scanning Laser Range Finder Specifications," vol. 2010, pp. 6, 2/1/2008, 2008.

[11] G. C. Haynes, "Dynamism Project," vol. 2010, 2009.

Evaluation of Composite Electronic Materials Based on Poly (3, 4 – propylenedioxythiophene/Poly – (p – Naptheleneethynylene) Wrapped Single Wall Carbon Nanotubes for Supercapacitors

NSF Summer Undergraduate Fellowship in Sensor Technologies
Johary Rivera (Chemistry) - University of Puerto Rico, Río Piedras Campus
Advisor: Dr. Jorge Santiago

ABSTRACT

Supercapacitors have emerged to do major advances in energy storage and technology. This paper summarizes the performance data of a specially designed poly (3, 4 – propylenedioxythiophene) PProDot based conducting polymer for use in a p-type supercapacitor. Performance data of these polymer composite electrodes are also compared with those of a poly (3, 4 – propylenedioxythiophene/poly – (p – naptheleneethynylene) wrapped single wall carbon nanotube supercapacitor. Longevity of the system was analyzed to determine life span and durability of both PProDot and PProDot/PNES/SWNT based devices. Both composites were characterized using Scanning electron microscopy (SEM).

1. INTRODUCTION

Electrochemical capacitors (EC) are new energy sources that have been under development for some time. Also known as “supercapacitors” or “ultracapacitors”, they can complement or replace batteries in electrical storage and harvesting, when high power delivery or uptake is needed.[1] Early electrochemical capacitors were rated at a few volts and had capacitance values from a fraction of farads to several farads.[2] But to meet higher requirements of future systems, their performance must be improved. One way to improve performance would be through the development of active storage devices using active materials (high surface area carbons, electroactive polymers, and transition metal oxides and nitrides). Another way would be to modify the electrolytes using conventional aqueous and nonaqueous electrolytes, advanced polymer electrolytes, or ionic liquids. Finally, device configurations, both symmetric and asymmetric, could be explored.

However, for such materials to be used in supercapacitors, they should fulfill the following requirements: (i) a high conductivity for assuring a high power density, (ii) an adequate pore size distribution and (iii) surface properties that could undergo redox reactions.[3]Such is the case of polymers and carbon nanotubes (CNTs) which have been reported in the literature. It has been demonstrated that carbon nanotubes can serve as a coating layer over ordinary current collectors to drastically enhance the electrode performance[4] and polymers have been shown to have very good cyclability and maximum capacitance.[5]

Due to the high requirements needed for better future systems, the region of the power vs. energy density plane of electrochemical capacitors was the goal of this investigation.. In this paper we present an electrochemical polymerization of a p-type supercapacitor device based on a poly (3, 4 – propylenedioxythiophene). Longevity of the system was analyzed to determine life span and durability of the electrochemical capacitor. Scan rate tests and oxidizing voltage window tests were also done. Scanning electron microscopy (SEM) characterization was done for the analysis of ProDot and CNTs morphologies. Also a poly – (p – naptheleneethynylene) wrapped single wall carbon nanotube supercapacitor was constructed to undergo the same analysis so that comparison of both systems was executed.

2. MATERIALS AND METHODS

2.1. *Preparation of solutions:*

A tetrabutylammonium hexafluorophosphate ($TBAPF_6$) electrolyte was prepared using 25 mL of propylene carbonate (PC) [Sigma-Aldrich, 99.7%] solution and 0.9796 g of $TBAPF_6$ [Fluka, 99.0%]. Also a *Poly (3, 4 – propylenedioxythiophene)I Tetrabutylammonium hexafluorophosphate electrolyte* (PproDot/$TBAPF_6$/PC) was prepared. The polymer solution was done using approximately 30 mg of Poly (3, 4 – propylenedioxythiophene) [Aldrich, 97%] dissolved in 10 mL of $TBAPF_6$ solution.

2.2. *Electropolymerization of ProDot in $TBAPF_6$/PC*

For the electropolymerization of ProDot, the electrode setup was the following: platinum (Pt) working electrode from Bio Analytical Systems (BAS), silver wire (Ag) 99.9% (d = 2mm) reference electrode from Alfa Asar and platinum strip(Pt) (4 mm height, 6 mm wide) cut from commercial grade Pt foil from Sigma Cohn Corporation as an auxiliary electrode.

The working electrode was polished previously with 0.3 micron and 0.05 micron alumina slurry and rinsed with distilled water. The electrodes were sonicated for 10 minutes and rinsed with distilled water and dried with gas nitrogen (N_2). The Ag wire and Pt strip were gently polished with Carbimet paper disc and put in a 90 micron solution.

The electropolymerization was done in a glove box under an N_2 atmosphere. The cyclic voltammetry was done using Pine Instrument Potenciostat. A simple CV experiment was done using an initial sweep up direction with a total of 24 sweeps. The sweep potentials were from -1000 mV to 1600 mV and a sweep rate of 100 mV/s.

2.3. *Tests done on electrodes*

Scan rate tests were done in a TBAPF6/PC solution using previously electropolymerized electrodes. The parameters used were the following: sweep rates: 25, 50, 100, 200, 250, 300, 400, 500, 750, 1000, 2500, 5000, 10000 mV/s, total sweeps: 6, sweep potentials: -1000 mV to 1000 mV, sweep up direction with 3 electrode setup mentioned.

Oxidizing voltage window tests were also conducted using a ProDot/TBAPF6/PC solution. Oxidizing tests were done using the following parameters:Sweep rate: 100 mV/s, total sweeps: 9, various sweep potentials. A sweep up direction CV with three electrode setup mentioned.

2.4. *Charge capacities and Coloumbic Efficiencies*

Anodic and cathodic charges were determined plotting each CV as a function of current vs. time (See Figure 1). The area below and above the curve is calculated by the same PineChem Software which gave us these values. Anodic and cathodic charges can not exceed a 30% limit difference. Columbic efficiency was determined by the ratio of cathodic to anodic charge capacity.

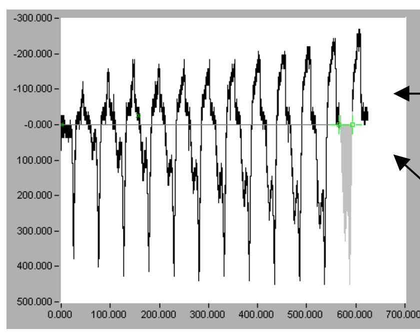

Cathode

anode

Figure 1: CV as a function of current vs. time

2.5. *Supercapacitor assembley and testing based on the ProDot/TBAPF$_6$/PC system*

The supercapacitor constructed is that of type I where the same p-doping polymer is used for both electrodes. One electrode contains ProDot in its neutral state and the other in its oxidized state. The same three electrode setup is used for the electropolymerization procedure and doping of both electrodes followed. The device was set up as shown in Figures 2 and 3.

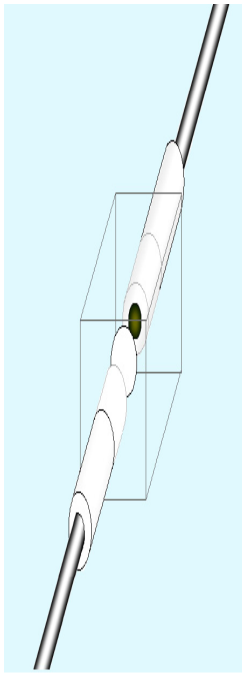

Figure 2: Supercapacitor device configuration

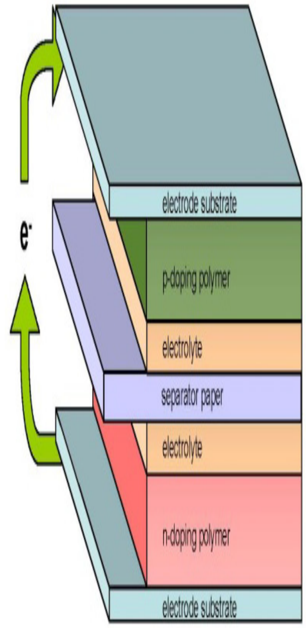

Figure 3: Supercapacitor device internal configuration

2.6. *Supercapacitor Scan Rate Tests*

After device construction scan rate tests were conducted using the following parameters:

Sweep rates: 250, 100, 50, 25, 500, 1000, 2500, 5000, 10000 mV/s, total Sweeps: 4 and a type I device potential of 0 mV to 500 mV. Charge potentials and columbic efficiencies were determined.

2.7. *Integrating Poly – (p – Naptheleneethynylene (PNES) Wrapped Single Wall Nanotubes Composite*

Same supercapacitor device was constructed but with the integration of PNES/SWNT. 8 μL of these SWNT were drop casted onto the platinum working electrodes. Same testing and experimental procedure was conducted.

3. *RESULTS*

3.1. *ProDot/TBAPF6/PC electrodes*

After electroploymeriztion of Pt electrode was used for scan rate tests, cathodic and anodic charges were calculated.

Electrode 1 used for oxidizing voltage window tests had a cathodic charge of 12.21 mC and an anodic charge of 22.26 mC. Polymer film had a deep purple color and was well deposited over the working electrode.

Electrode 2 used for scan rate tests had a cathodic charge of 9.649 mC and an anodic charge of 16.17 mC. Polymer film also presented a deep purple color and was well deposited over the working electrode.

NOTE: Anodic and cathodic did not exceed the 30 % limit of difference.

Table 1: Scan Rate Tests on PproDot 1

Scan rate (mV/s)	*Lower limit (mV)*	*Upper Limit (mV)*	*Anodic Charge mC*	*Cathodic Charge mC*	*Coloumbic Efficiency(%)*
25			*8.396*	*8.020*	*95.52*
50			*7.999*	*7.797*	*97.47*
100			*7.544*	*7.444*	*98.67*
200			*6.825*	*6.774*	*99.25*
250			*6.490*	*6.452*	*99.41*
300	*-1000*	*1000*	*6.187*	*6.155*	*99.48*
400			*5.582*	*5.551*	*99.44*
500			*4.933*	*4.900*	*99.33*
750			*3.690*	*3.623*	*98.18*
1000			*2.925*	*2.778*	*94.97*
2500			*1.434*	*995.2 uC*	*69.40*
5000			*854.9 uC*	*411.0 uC*	*48.08*
10000			*496.5 uC*	*156.5 uC*	*31.52*

NOTE: Boxed scan rates have been graphed to show slow degradation of polymer film. These are the limits where the polymer film is still well adhered to the Pt electrode.

Graph 1: Scan Rate Tests

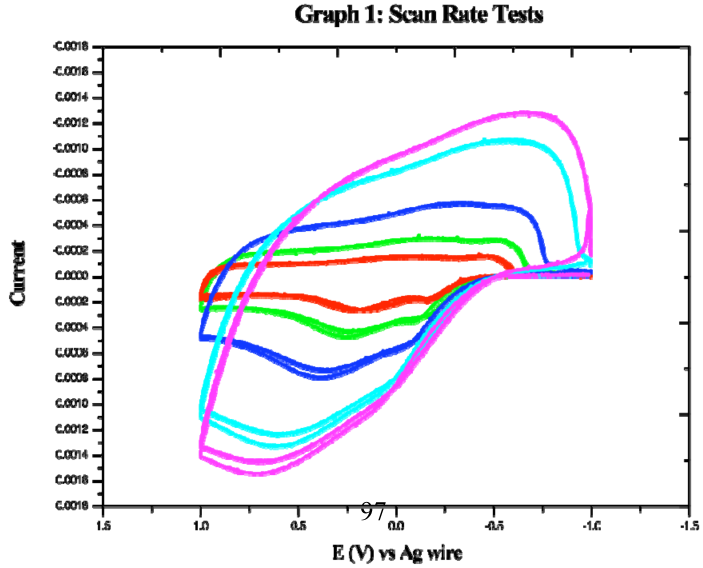

Table 1 and Graph 1 show that as the scan rate increases there is an evident increase of columbic efficiency and consequent degradation of polymer film.

Graph 2: Peak Height vs Scan Rate Tests

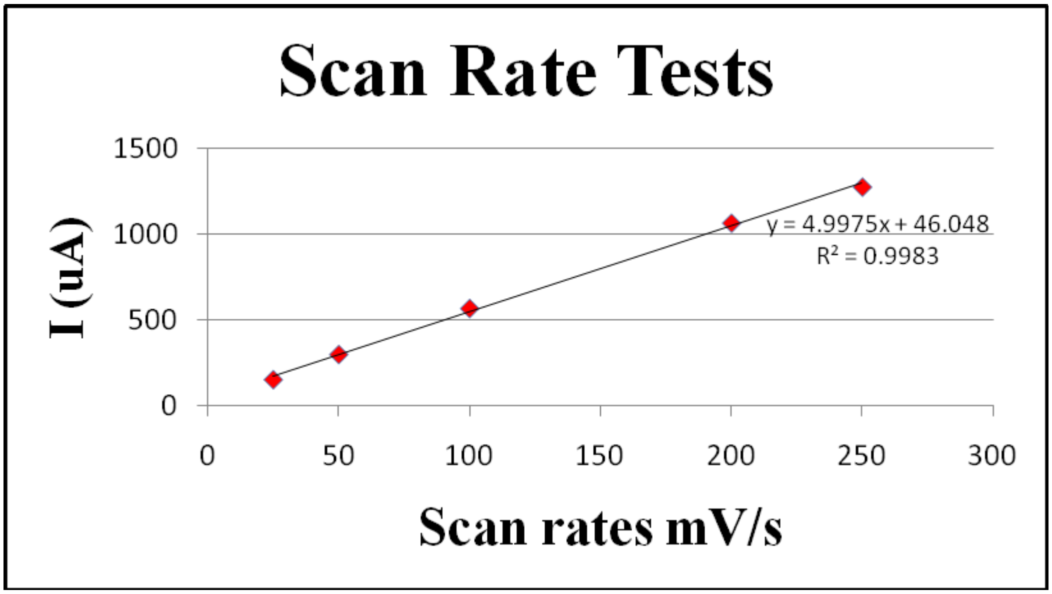

This graph evinces immobilized polymer film from the 25 mV/s to 250 mV/s scan rate

Table 2: Oxidizing Voltage Window Test

Sweep rate (mV/s)	*Lower limit (mV)*	*Upper limit (mV)*	*Anodic charge*	*Cathodic charge*	*Coloumbic Efficiency (%)*
100	-1000	900	10.13	9.295	91.76
		1000	10.45	9.710	92.92
		1100	7.741	6.680	86.29
		1200	10.28	8.160	79.38
		1300	13.81	10.44	75.60
		1400	18.65	13.78	73.89
		1500	21.59	17.18	79.57
		1600	26.70	21.81	81.69
		1700	32.30	26.28	81.36
		1800	39.16	31.39	80.16
		1900	48.23	38.28	79.37
		2000	56.01	44.85	80.07
		2200	70.93	54.35	76.62
		2400	89.80	66.05	73.55

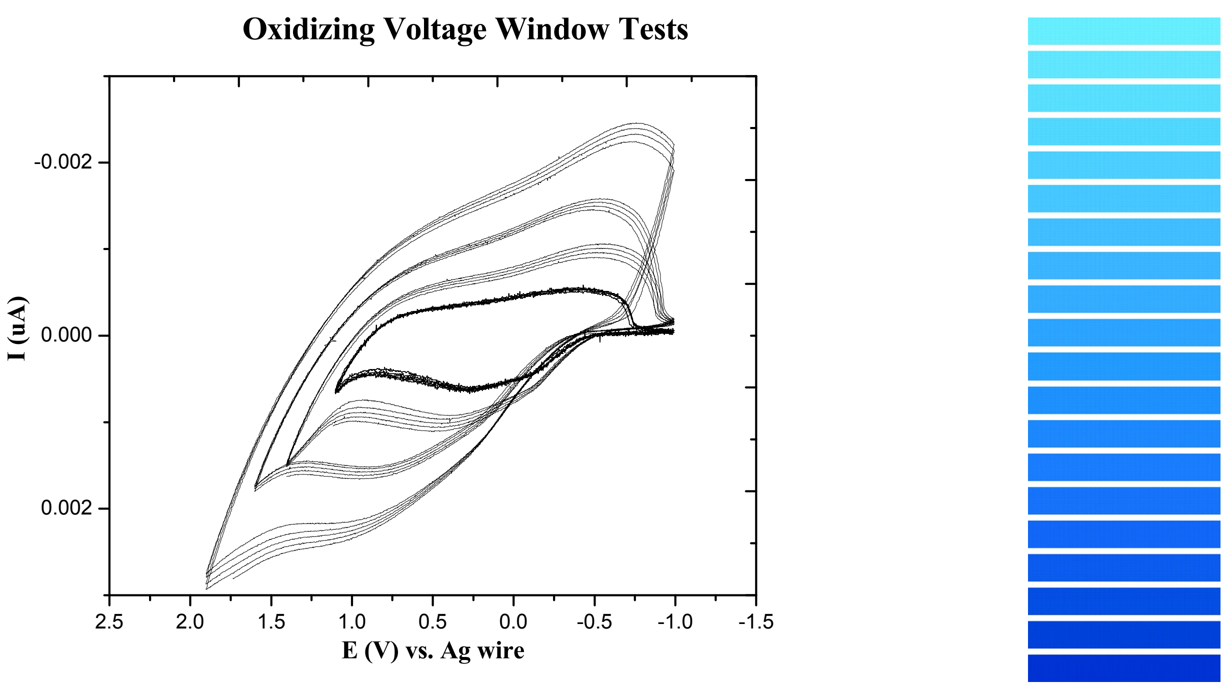

Oxidizing voltage window tests show a decrease in coloumbic efficiency as the potential limit increases meaning degradation of polymer film. As the potential limit increases, the polymer film changes from a light blue color to a navy blue, as shown at the right side of the graph.

3.2. *ProDot/TBAPF6/PC Supercapacitor Device*

After electroploymeriztion of the Pt working electrode that was used for scan rate tests, cathodic and anodic charges were calculated.

Electrode 1 had an anodic charge of 12.74 mC and a cathodic charge of 8.467 mC. It was doped to its oxidized state and recovered an anodic charge of 5.109 mC and a cathodic charge of 4.985 mC. Its polymer film turned from a deep purple to a blue color after oxidation.

Electrode 2 had an anodic charge of 13.05 mC and a cathodic charge of 8.238 mC. It was doped to its neutral state and recovered an anodic charge of 1.010 mC and a cathodic charge 973.1 μC. Its polymer film remained a deep purple color after neutralization.

Table 3: Supercapacitor Scan Rate Tests

Scan rate (mV/s)	*Lower limit (mV)*	*Upper Limit (mV)*	*Anodic Charge mC*	*Cathodic Charge mC*	*Coloumbic Efficiency(%)*
25			8.396	8.020	95.52
50			7.999	7.797	97.47
100			7.544	7.444	98.67
200			6.825	6.774	99.25
500	-1000	1000	4.933	4.900	99.33
1000			2.925	2.778	94.97
2500			1.434	995.2 uC	
5000			854.9 uC	411.0 uC	48.08
10000			496.5 uC	156.5 uC	31.52

Scan Rate Tests on Device

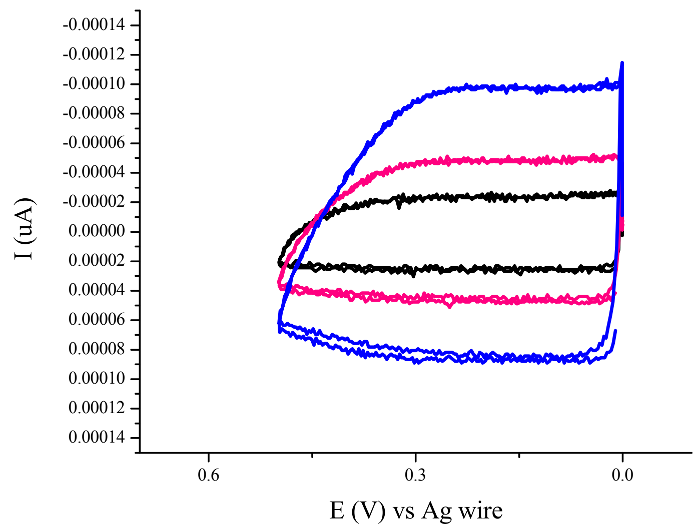

Scan rate tests on the device demonstrated an evident decrease on columbic efficiency while there was an increase in scan rate. The graph of scan rates done on the device show degradation of the polymer film while the speed of the system is increasing. In other words increase of scan rate is an increase of degradation of polymer film.

3.3. *ProDot/PNES/SWNT electrodes*

After drop casting SWNT and electroploymeriztion of Pt electrode was used for scan rate tests, cathodic and anodic charges were calculated.

Electrode 1 used for oxidizing voltage window tests had a cathodic charge of 9.200 mC and an anodic charge of 15.97 mC. Polymer film had a deep purple color and was well deposited over the working electrode.

Electrode 2 used for scan rate tests had a cathodic charge of 10.02 mC and an anodic charge of 16.10 mC. Polymer film also presented a deep purple color and was well deposited over the working electrode.

NOTE: Anodic and cathodic did not exceed the 30 % limit of difference. Same tendencies on all tests were seen.

Table 4: Scan Rate Tests

Scan rate (mV/s)	*Lower limit (mV)*	*Upper Limit (mV)*	*Anodic Charge mC*	*Cathodic Charge mC*	*Coloumbic Efficiency(%)*
25	*-1000*	*1000*	*10.28*	*8.391*	*81.62*
50			*8.333*	*7.804*	*93.65*
100			*7.008*	*6.802*	*97.06*
200			*6.032*	*5.918*	*98.11*
250			*5.557*	*5.485*	*98.70*
300			*5.333*	*5.244*	*98.33*
400			*4.759*	*4.696*	*98.68*
500			*4.337*	*4.282*	*98.73*
750			*3.455*	*3.385*	*97.97*
1000			*2.778*	*2.683*	*96.58*
2500			*1.332 uC*	*1.018 uC*	*76.43*
5000			*910.0 uC*	*793.0 uC*	*87.14*
10000			*460.1 uC*	*166.9 uC*	*36.27*

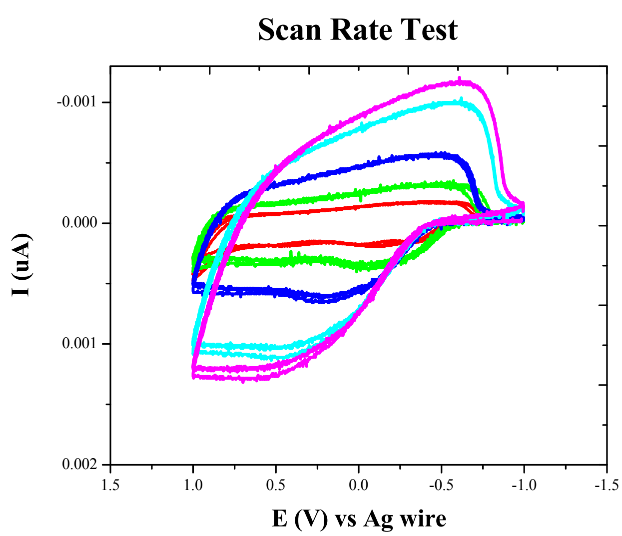

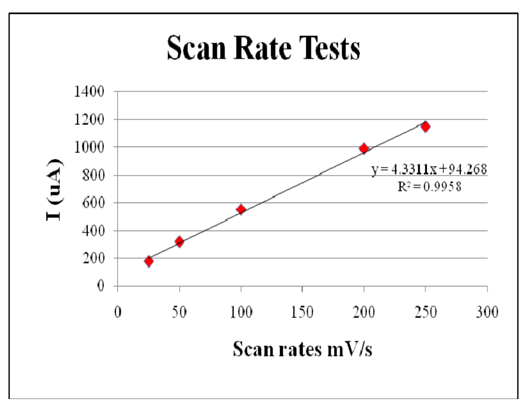

Table 5: Oxidation tests on PproDot/PNES/SWNT 1

Sweep rate (mV/s)	*Lower limit (mV)*	*Upper limit (mV)*	*Anodic charge*	*Cathodic charge*	*Coloumbic Efficiency (%)*
100	-1000	900	4.549	4.235	93.10
		1000	5.079	4.704	92.62
		1100	6.185	5.356	86.59
		1200	8.259	6.594	79.84
		1300	10.81	8.448	82.98
		1400	18.65	13.78	73.89
		1500	12.34	10.00	81.04
		1600	14.93	11.96	80.11
		1700	18.06	14.39	79.67
		1800	21.57	17.27	80.06
		1900	25.02	20.32	81.22
		2000	28.90	23.70	82.00
		2200	42.61	33.57	78.78
		2400	53.71	40.64	75.67

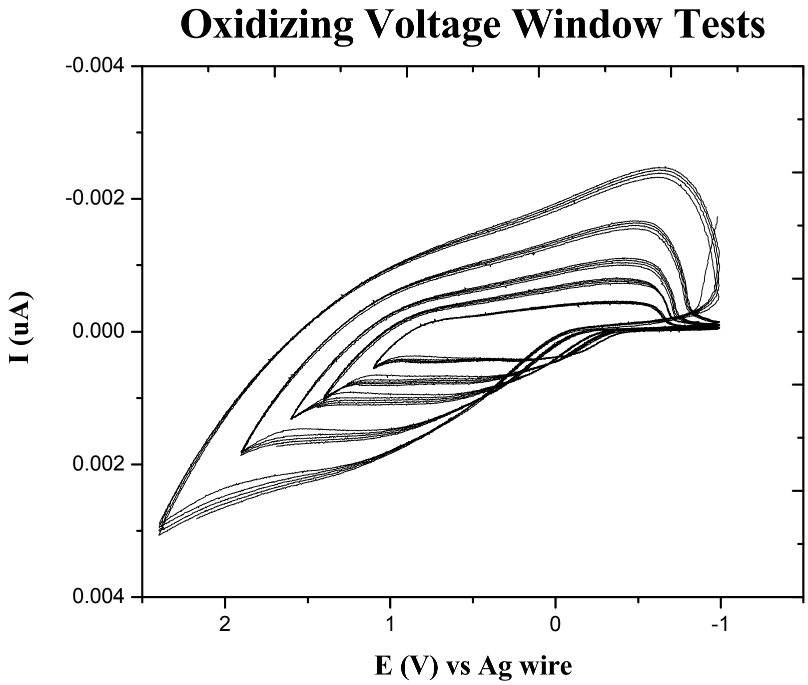

3.4. *ProDot/PNES/SWNT Supercapacitor Device*

After electroploymeriztion of the Pt working electrode that was used for scan rate tests, cathodic and anodic charges were calculated.

Electrode 1 had an anodic charge of 9.745 mC and a cathodic charge of 6.370 mC. It was doped to its oxidized state and recovered an anodic charge of 3.259 mC and a cathodic charge of 3.259 mC. Its polymer film turned from a deep purple to a blue color after oxidation.

Electrode 2 had an anodic charge of 8.061 mC and a cathodic charge of 5.809 mC. It was doped to its neutral state and recovered an anodic charge of 828.0 uC and a cathodic charge 872.6 μC. Its polymer film remained a deep purple color after neutralization.

Table 6: Supercapcitors Scan Rate Tests

Scan rate (mV/s)	*Lower limit (mV)*	*Upper Limit (mV)*	*Anodic Charge uC*	*Cathodic Charge mC*	*Coloumbic Efficiency(%)*
25	-1000	1000	340.7	330.8	97.09
50			382.3	368.7	96.44
100			407.8	390.2	95.68
200			429.4	402.5	93.74
500			285.8	279.0	97.62
1000			233.1	226.9	97.34
2500			151.9	142.3	93.68
5000			100.9	82.64	81.90
10000			69.16	39.76	57.49

Scan Rate Tests on Device

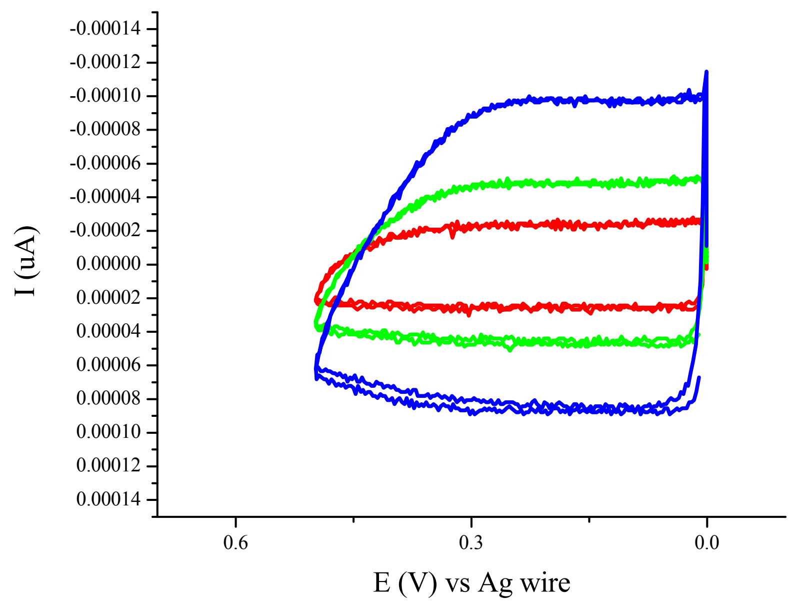

Comparison PproDot vs PproDot/PNES/SWNT

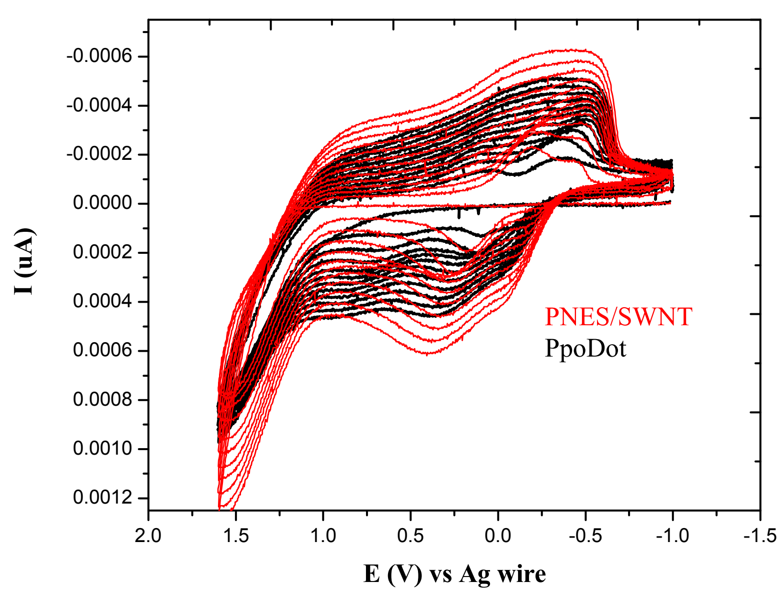

DISCUSSION

In the construction of a supercapacitor various properties should be considerate. In the making of the ProDot/$TBAPF_6$/PC capacitor, the polymer and the whole electrolyte solution were studied before the construction of the device. ProDot or poly (3, 4 – propylenedioxythiophene) is an electronically conducting polymer (ECP) and provided higher capacitance and/or high power capability. ECP's have the ability to tailor conductivity, voltage window, storage capacity and chemical stability. On the other hand $TBAPF_6$ has a small ionic radius. This permitted the constant movement of ions in the electrochemical process which is crucial in the electropolymerization of electrodes and accumulation of charge. Each electrode accumulated more cathodic and anodic charge compared to the ProDot /$TEABF_4$/PC supercapacitor previously constructed (approximately an increase of 50% accumulation of charge).

Device configurations, both symmetric and asymmetric are very important in the construction of a device. This study focused on a Type I symmmetric capacitor containing the same p-doping polymer. Increasing storage capacity and the operating potential differs from type to type. N-polymers are inherently less stable than p-doping polymers. As a consequence, p-doping polymers were used. This added atoms that increased the number of free positive charge carriers. Page: 107

Scan rate tests of the electropolymerized electrodes showed that as the scan rate increases there is an evident increase of columbic efficiency and by consequence degradation of polymer film. Scan rate tests are primarily done to experiment how fast a system can operate without damaging some aspect of functionality. Ions tend to gain more kinetic energy as scan rate increases. Scan rate tests were also done to the whole device and responded the same way as did the electropolymerized electrode. Peak height was plotted versus scan rate where a nice correlation line demonstrates immobilized polymer film. Also oxidation tests were conducted and effectively showed a degradation of the polymer film while coloumbic efficiency decreased and potential limit increased. By changing the sweep potentials, identification of how far the oxidation state can be taken. What helped in the determination in the over oxidation of the polymer film was the surface appearance and color of the electropolymerized Pt electrode. When over oxidized the polymer film changed from a light blue to dark blue color. Also tearing and scratching of polymer film was observed.

Integrating PNES/SWNT gave similar results on scan rate tests and oxidizing tests. Scan rate tests done on device show very good distribution on charge. The scan rate test CV resembles a rectangular form which confirms a very good distribution of charge. Comparing cyclic voltammagrams of PproDot/TBAPF6/PC device and the PproDot/PNES/SWNT we see a major capacitance using the SWNT composite than that using PproDot only. A 3% difference is obtained.

REFERENCES

[1] P. Simon; Y. Gogotsi. Materiales for Electrochemical Capacitors. *Nature Materials*. **7**, 845-846 (2008).

[2] A.F. Burke; J.R. Miller. Electrochemical Capacitors: Challenges and Opportunities for Real World Applications. *The Electrochemical Society Interface*. 53-55, (2008)

[3] E.J. Ra, E. Raymundo, Y.H. Lee, F. Beguin. High Power Supercapacitors using polyacrylonitrile-based Carbon Nanofiber Paper. Carbon 47 (2009) 2984-2992

[4]C. Du, N.Pan. High Power Density Super Capacitor Electrodes of Carbon Nanotube Films by Electrophoretic Deposition. Nanotecnology 17 (2006) 5314 -5318

[5] F. Marchioni, J. Yang, W. Walker, F. Wilde. A Low Band Gap Conjugated Polymer for Supercapacitor Devices. J.Phys.Chem. B (2006),110, 22202 - 22206

MATERIAL TESTING OF SHAPE MEMORY POLYMERS FOR MODULAR ROBOTICS APPLICATIONS AND DEVELOPMENT OF A PROTOTYPE SMP GRIPPER FOR mini-PR2 ROBOT.

NSF Summer Undergraduate Fellowship in Sensor Technologies
Jennifer L. Smith (Biomedical Engineering) – North Carolina State University
Advisors: Paul White and Dr. Mark Yim

ABSTRACT

Goals that have yet to have been realized in the field of modular robotics include low cost mass production, and scalability. Shape memory polymers are light weight, low-cost, and have a large degree of flexibility in material design. For these reasons these polymers have the potential to help reach current goals of modular robotics. The percent recovery and force of these materials for use in actuation was tested in this research. A prototype SMP gripper consisting of two reconfigurable one way SMP actuators was developed that successfully picked up an object weighing one gram in 90% of trials. This SMP gripper is compatible with the CKbot modules from Dr. Mark Yim's laboratory at the University of Pennsylvania and it was installed on an existing modular robot, the mini-PR2, and the robot was programmed to use the gripper successfully. While there remain other obstacles in scaling and mass production problems, the shape memory component of this gripper could be produced on a wide range of scales, and with the proper equipment, made in large quantities for mass production. Future work to improve the SMP gripper will need to involve developing a method of making the gripper reversible.

1. INTRODUCTION

Self reconfigurable robots are built from modules, each of which has all the components required for a functioning robot, such as actuators, sensors, batteries and processing power. A module must be able to communicate with other modules, move with respect to other modules, and allow for connection to and disconnection from other modules. It is widely agreed that robots of this type potentially have three main advantages: their versatility, their robustness, and their low cost [1, 2]. The ability of modular self reconfigurable robots to adapt and change shape allows them to be versatile robots that can accomplish a wide variety of tasks. The robots are robust in two aspects: first, a damaged or nonfunctional module can be compensated for by others [1]. In addition, since modules are all equivalent, there is the possibility of robots replacing broken parts autonomously, allowing for self repair [2]. The final advantage of self reconfigurable robots is their potential for lowering production cost. Since these robots consist of many copies of one or a few types of modules, mass production could potentially lower the overall cost of the robot. In addition, since one modular self reconfigurable robot can achieve many tasks, it could be reused in many situations, saving costs.

These advantages however have not yet been fully realized. The advantage of versatility is only applicable in some situations. A modular robot will probably perform inferiorly to a robot custom designed for a specific task [2] However in a situation in which one robot must complete multiple different tasks, or the nature of tasks is unknown before a robot is deployed, the versatility of modular robots is extremely desirable. A proposed example of such a situation is space exploration missions [2]. There is also potential for success with these types of robots in other unpredictable situations such as search and rescue missions.

Low cost modular robots have also yet to have been realized. While in theory mass production of many identical modules would reduce cost, current robot designs have not yet made mass production feasible. Although control algorithms have been developed to handle millions of units, currently the modular robot with the largest number of active modules is Polybot with 56 modules, developed by Yim et al.[2]. Without hardware design improvements, the mass production of thousands or millions of modules is not possible.

Another challenge faced by modular robots is scalability. The precision with which a modular robot can approximate a complex shape is a function of the module size. The smaller each module is, the more accurately a modular robot can take on a complex form. Smaller robots can also accomplish tasks that would be unfeasible for larger robots [3]. Examples include squeezing through very small spaces, such as under a door or through a human artery. The smallest module created to date is Miniature, developed by Yoshida et al, with a module dimension of 40 x 40 x 50 mm [2].

2. BACKGROUND

2.1 Actuators

Actuators can allow individual modules to move within the environment and allow modules to move with respect to one another in order to achieve locomotion and self reconfiguration [1]. Increased numbers of actuators improve module autonomy, degrees of freedom of the modular robot, and the ease of motion and self reconfiguration for the robot [1]. However, these improvements come at the cost of simplicity, as well as size and weight of the modules. One of the major obstacles to overcome in the effort to scale down the size of modules is the space taken up by actuators [3]. Typically, actuators contribute more than 50% of the volume and weight of the whole module [3]

2.2 Current Actuator Types

Stoy et al. [1] provide an overview of current actuator types used in modular robotics. To date, most modular robotic systems utilize brushless motors as their actuators due to these motors' medium size and high efficiency. However brushless direct current (DC) motors are highly complex and relatively expensive. Another option for actuation are brushed DC motors. These motors are less efficient and larger than brushless DC motors but are easier to control. Stepper DC motors are another alternative – while being slightly more complex than brushed DC motors they are useful if high precision is necessary. However, DC motors become impractical as module size decreases. More recently, shape memory alloys have been used in self reconfigurable robots as a smaller scale actuator.

Shape memory alloys have the property of returning to a memorized shape with a change in temperature. They exhibit high force and are extremely small. This property has been utilized to make several micro scale shape memory alloy actuators [4, 5] One design that showed particular promise for self reconfiguration applications was Yoshida et al's [6] shape memory alloy actuator, which could be utilized in micro scale modular robotics. The actuator consists of two counter torsion shape memory alloy springs. The springs memorize the 0 degree rotation shape and are preloaded by twisting 180 degrees in the reverse direction. The springs remain in the original zero degree position until heat is applied. When one of the coils is heated by an electric current, its Young's modulus increases resulting in a large torque in the direction to restore the zero degree rotation state. This causes the assembly to bend, allowing for actuation. Despite these accomplishments, shape memory alloys do not solve all scaling problems in modular robots since they are difficult to control and react fairly slowly - the alloys need time to cool down and expand before each contraction [1].

2.3 Shape Memory Polymers

Shape memory polymers (SMP) are another smart material with potential usefulness for modular robotics applications. Shape memory polymers are polymers that are able to memorize temporary shapes and then recover their permanent shape with some external stimulus – usually a thermal change [6]. The permanent shape memorization is achieved through chemical or physical crosslinking, and temporary shapes can be fixed in the glass transition or melting transition phase [6]. Xie and Rousseau [7] conducted material testing on these polymers. The samples were immersed in a 70°C water bath for 6 seconds, and then deformed manually into a temporary shape. The temporary shape was set by dipping the sample into a cold water bath at 20°C, while maintaining the deformation load. Shape recovery was achieved by again immersing the sample in the 70°C water bath. Figure 1 depicts the shape memory capabilities of these types of polymers.

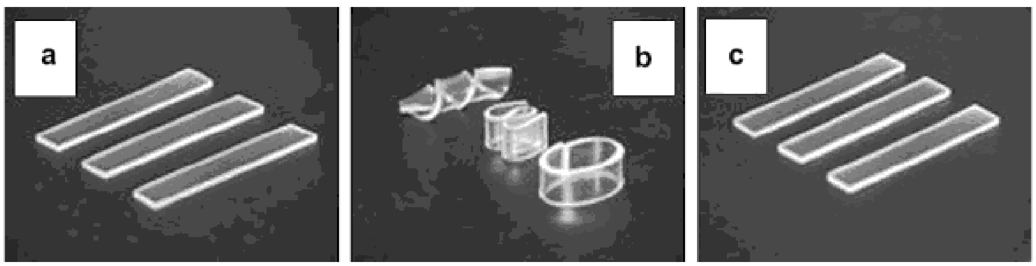

Figure 1a) original/permanent SMP shape b) fixed temporary states c) recovered shapes [7]

In comparison to shape memory alloys, SMPs have some unique advantages. They are light weight, and have great flexibility in terms of material design [6]. They also exhibit high recovery strain and are low cost [7]. Shape memory polymers are also advantageous since it is possible to tailor their material properties. In work reported in 2009, Xie and Rousseau [6] showed that it is possible to precisely tune the glass transition temperature of epoxy shape memory polymers, so they can meet specific application needs. They accomplished this by reducing the polymer's crosslink density or introducing chain flexibility. SMP's with distinctive glass transition temps ranging from 30 to 89°C were achieved. All of the polymers achieved fairly stable moduli in their glassy and rubbery regions and the difference between glass modulus and rubber modulus ranged from two to three orders of magnitude. Xie and Rousseau saw experimental evidence to suggest that a larger difference in glass and rubber moduli indicated greater shape fixity. Despite these advantages, the use of these polymers as functional materials remains rare, and they have yet to have been utilized in the field of modular robotics.

Shape memory polymers do have some disadvantages however. The recovery stress and fatigue strength of SMPs is less than that of shape memory alloys [8]. In addition they lack some particular functions that would be useful for practical applications such as good electric conductivity and high recovery force [7]. For this reason efforts have been made to develop shape memory composites.

2.4 Shape Memory Composites

Shape memory composites (SMC) consist of shape memory polymers reinforced by various other materials. Tobushi et al [8]developed a shape memory composite that consisted of two kinds of shape memory alloy tapes, one showing shape memory effect and the other showing superelasticity, that were heat-treated to memorize the round shape. These shape memory alloy tapes were arranged facing in opposite directions and sandwiched between two shape memory polymer sheets. The resulting SMC belt combined positive characteristics of both the SMA and SMP. A large recovery force was observed at high temperature, a deformed shape could be held at low temperature and then be recovered, and a large load could be carried. The SMC bends in the direction of the shape-memorized round shape of the shape memory effect SMA when heated and bends in the opposite direction toward the memorized round shape of the superelastic SMA during cooling.

Shape memory composites filled with particles such as carbon black, Ni, carbon nanotubules or short fibers have also been developed [7]. These types of SMC have demonstrated new functions such as electrical conductivity and magnetic-responsive performance. Added functions such as electrical conductivity could be utilized in heating the SMPs. If an SMP was conductive, current could be run through the polymer to heat it up rather than using an outside heating source. However there was little improvement in the mechanical properties of these types of composites. Lan et al [7] developed a continuous fiber reinforced SMC that has excellent mechanical properties, namely a large strain in bending. They also created a hinge actuator using the fiber reinforced SMC, and demonstrated it moving a prototype solar panel.

3. APPLICATION OF SMP'S FOR MODULAR ROBOTICS

The advantages of shape memory polymers make them a good candidate for exploration into new forms of actuation in modular robots. If the recovery force of two SMPS could be used in an antagonistic fashion, a shape memory polymer actuator could be created. Such an actuator could be used with current modular robots and have potential to help in the design process of developing small scale, mass-producible robots. The purpose of this research was to manufacture and characterize the material properties of a shape memory polymer to determine the material's feasibility to be used in its pure form as an actuator for use in modular robotics. A shape memory polymer actuated gripper prototype was developed, tested, and installed on an existing robot. This gripper uses two one way actuator SMPs as a reconfigurable gripper. The gripper can be opened into one of a variety of different shapes each time it is used. This provides versatility in picking up objects of differing sizes and shapes. Since the SMPs used on this initial prototype are one way actuators, they must be retrained after each pick up cycle. A method of antagonistic actuation is needed to allow the SMP actuators to operate autonomously for more than one cycle.

4. METHODS

4.1 Fabrication

The method developed by Xie and Rousseau [6]was used to fabricate the shape memory polymer samples for this research. The diglycidyl ether of bisophenol A epoxy monomer (EPON 825) and the curing agents poly(propylene glycol)bis(2-aminopropyl)ether (Jeffamine D230) and decylamine (DA) were used. The samples' composition was as follows: 0.02 mol of EPON 826, 0.005mol D230 and 0.01mol DA. The EPON 826 was weighed into a glass bottle and then placed in an oven preset at 70°C to melt for thirty minutes. After melting, the appropriate volume of Jeffamine D230 and decylamine were inserted into the glass bottle. The glass bottle was shaken vigorously by hand to mix all the components. The mixture was then poured into a mold. For the purposes of this research, rectangular molds were chosen. The mold was then placed in a 100°C oven for 1.5 hours to cure the samples, which were then postcured on a hotplate at a temperature of 130°C for one hour. The time for curing was kept precise, as this is the factor that determines the glass transition temperature of the polymers. In this case, the fabricated polymers had a glass °transition temperature of about 80°C.

4.2 Steady State Temperature Testing

A Steinel 34100 Ultra Heat Dual Temperature Heat Gun was utilized throughout this research as the method of heating the shape memory polymers. This heat gun had two settings, a low temperature setting of 600°F or 316°C and a high temperature setting of 950°F or 510°C. A consistent method of heating the shape memory polymer to temperatures at and around its glass transition temperature using a heat gun needed to be determined. For this reason steady state temperature testing was conducted using the heat gun and an LM35 Precision Centigrade Temperature Sensor. The LM35 Temperature sensor is calibrated to measure temperature in degrees Celcius, and was connected in the circuit shown in Figure 2. An input voltage of 5 volts and a 1K resistor were used. The output voltage from the temperature sensor circuit was directed through Measurement Computing's USB-1208FS device which, along with its accompanying software, converted the output voltage to an array of temperature readings in MATLAB.

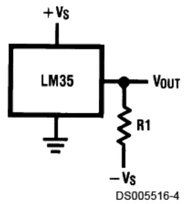

Figure 2. Circuitry for LM35 Temperature Sensor. Vs=5V, R1=1000Ω. [9]

The heat gun and temperature sensor were arranged level with each other at varied distances apart, and two minute long sample periods were taken with the heat gun on, to determine the ambient temperature reached at the temperature sensor. Temperature sensor data was verified for accuracy with a thermometer placed next to the temperature sensor to verify that sensor output was reasonable. The experimental setup for steady-state temperature testing is shown in Figure 3.

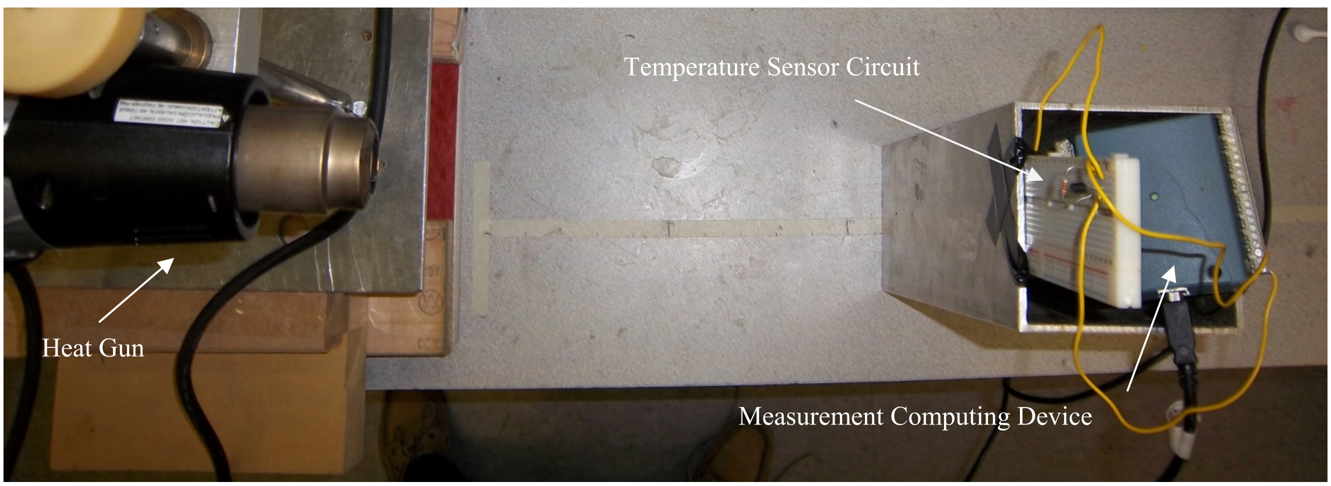

Figure 3. Set up for Steady State Temperature Testing

4.3 Tensile Testing

Tensile testing using an Instron Model 5544 Electromechanical Test System was conducted on the shape memory polymers, both at room temperature and above glass transition temperature. Before beginning tensile testing, the original dimensions of the samples were recorded. In order to accomplish material testing without damaging the shape memory polymer samples a pair of aluminum clamps was manufactured. The SMP samples were clamped into these aluminum clamps, which were in turn clamped into the Instron 5544 for testing. Figure 4 illustrates the experimental setup.

Figure 4. SMP sample mounted to aluminum clamps in Instron machine for tensile testing

Before each tensile test the sample was aligned vertically with Instron's grips. At room temperature ten tensile tests were conducted consecutively on the same sample. The Instron was set to move at a rate of 1mm/minute, and the room temperature samples were allowed to deform up to 2% strain. A tensile test was also conducted above glass transition temperature of the polymer, with the Instron set to move at a rate of 1mm/min, and the sample allowed to deform up to 15% strain. This test was destructive to the sample, so only one trial was conducted.

4.4 Percent Recovery Testing

In order to conduct percent recovery testing the apparatus shown in Figures 5 and 6 was constructed. The apparatus includes a platform the shape memory polymer was clamped to, a platform to which the heat gun was mounted, and an adjustable platform. The distance away from the SMP that the heat gun platform was located could be adjusted. The adjustable platform had a force sensor with a probe clamped to it. When this platform was moved up and down, the force sensor's probe could deform the SMP.

For the percent recovery testing, the original shape of the SMP was a flat bar with dimensions 30mm x 10mm x 1mm. The SMP was mounted onto the apparatus, and the thermometer was placed as close to the SMP as possible without touching it. The heat gun was turned on medium and the SMP was allowed to heat up for one minute. The ambient temperature reported by the thermometer at the end of one minute was recorded. The adjustable platform was then raised, allowing the force sensor probe to make contact with the SMP, and deform it to a new stored angle. The ambient temperature at the end of deformation was recorded and then the heat gun was turned off. The SMPs were heated for one minute before deforming because steady state temperature tests indicated that it took one minute for a constant temperature to be reached using the heat gun as the source of heat. The SMP was allowed to cool for five minutes, to ensure that the SMP cooled down to room temperature, allowing the temporary bent shape to be stored. After five minutes of cooling, the force sensor was moved down and the SMP was removed from the apparatus. Its stored angle was measured and recorded. The SMP was then placed back in the apparatus, and it was ensured that nothing was in the way of the SMP freely deforming back to its original shape. The heat gun was then again turned on for one minute, heating the SMP, allowing it to recover. The ambient temp at the end of one minute was recorded and then the heat gun was turned off. The SMP was again allowed five minutes to cool, and then was removed from the apparatus and the recovered angle was measured.

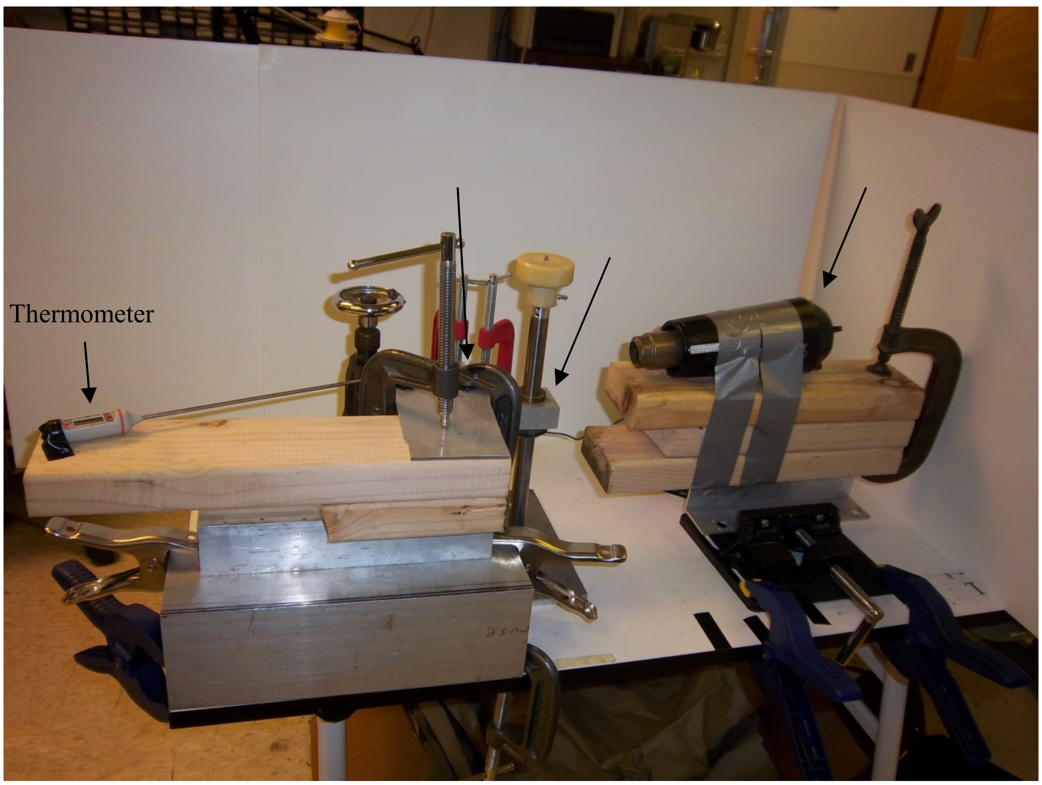

Figure 5. Apparatus used for SMP percent recovery testing.

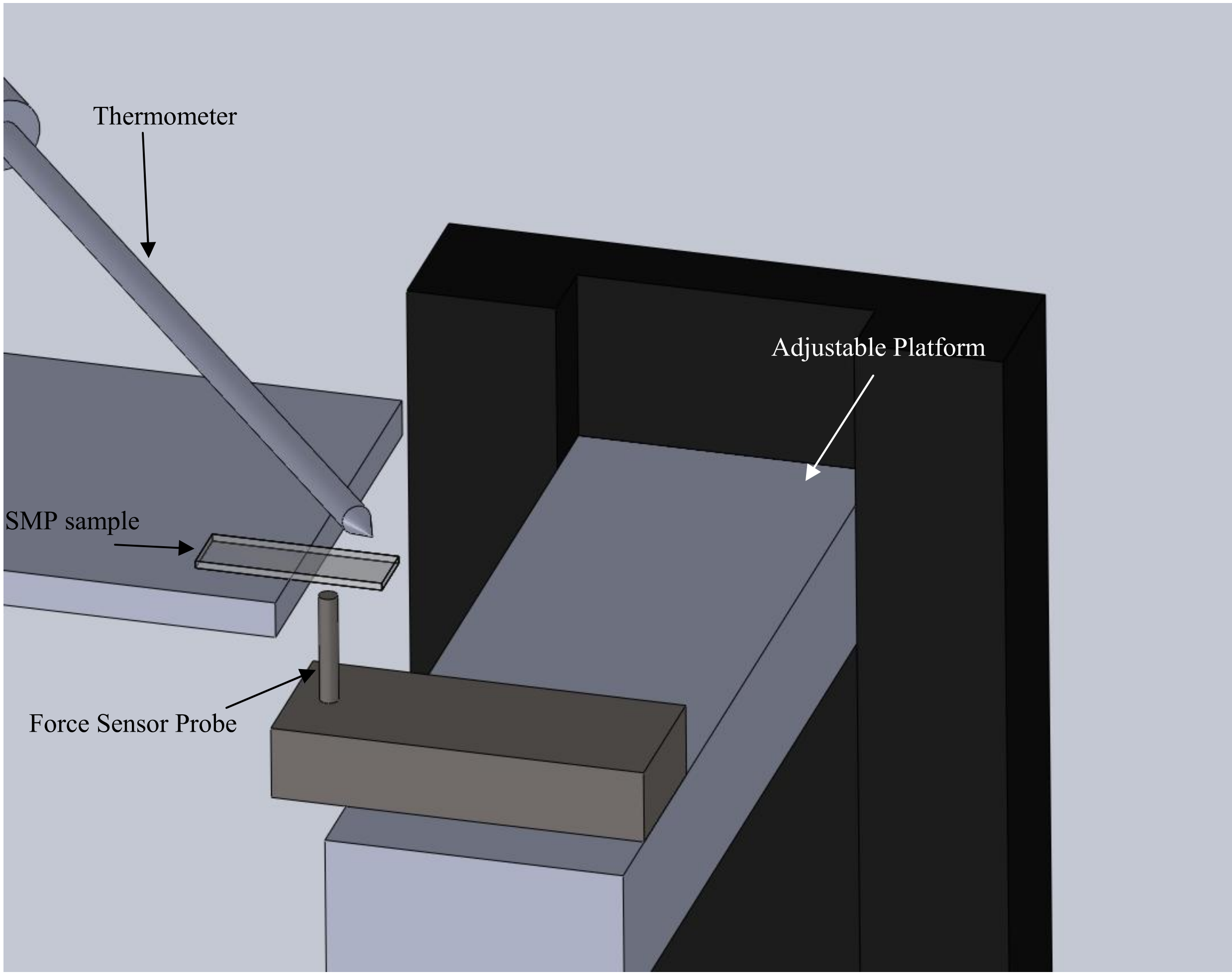

Figure 6. Close up of schematic of an SMP sample ready for percent recovery testing.

The percent recovery was calculated as the ((stored angle) – (recovered angle))/(stored angle). Throughout the trials, the smp was always heated up before deforming with the heat gun at a distance of seven inches away. During recovery, the heat gun was placed at varied distances away to obtain different recovery temperatures. A range of angles from small to large were deformed and recovered at each heat gun distance.

4.5 Force Testing

The same apparatus as was used in percent recovery testing was also used to conduct force testing. A longer probe was used on the force sensor however, to minimize drift of the force sensor's results due to change in temperature. The force sensor only compensates for temperature change up to 71.1°C, and much of the testing needed to be above this temperature since the SMP's glass transition temp is 80°C. Using a longer probe distanced the force sensor device from the heat enough to eliminate drift effect due to heat.

Before each force test the force sensor was zeroed, and then the heat gun was turned on for one minute, allowing SMP to heat up. Ambient temperature was recorded at the end of one minute. The force sensor was then moved upward, deforming the SMP to a new stored angle. The maximum reading on the force sensor during this process was recorded as the force to engage. The heat gun was then turned off and the SMP was allowed to cool for five minutes. The force sensor's position was not moved. Once the sample had cooled, it was removed from the apparatus and the stored angle was measured. The SMP was then clamped back on the apparatus, and the heat gun was turned back on for one minute. The maximum reading on the force sensor was recorded as recovery force. The force sensor was moved down to allow the SMP to freely recover, and then the heat gun was turned off and the SMP was allowed to cool for five minutes before beginning the next trial. Throughout the force testing trials, the SMP was always heated up before deforming with the heat gun at a distance of seven inches away. During recovery, the heat gun was placed at varied distances away to obtain different recovery temperatures. A range of angles from small to large were deformed and their recovery force was measured at each heat gun distance.

4.6 Static Friction Testing

Static Friction Tests were conducted to determine the static coefficient of friction μ between the SMP samples and aluminum, ABS plastic's rough side, and ABS plastic's smooth side. Five SMP samples were used for this testing and each sample was placed on the surface being tested (aluminum, ABS rough or ABS smooth). The surface was tilted until the SMP slipped down the surface. The angle at which slip occurred was recorded and the coefficient of friction μ was calculated as the tangent of this angle. Each of the five samples was tested four times on each surface, for a total of 20 recorded angles for each surface.

4.7 Design of a Shape Memory Polymer Gripper for mini-PR2 Modular Robot

Once all material testing was complete, a SMP gripper was designed. The gripper was designed to be compatible for fitting with existing CKbot modules in Dr. Mark Yim's lab. The mini-PR2 robot uses these modules and the SMP gripper was installed on and used by this robot. The gripper consists of a clamping device that holds two SMP samples parallel to one another at a variable distance apart. The distance between the SMP samples can be varied by changing the width of the middle component of the gripper. Middle components of width 8mm, 12mm, 16mm, 20mm, and 24mm were manufactured. The device components were cut from ¼ inch thick ABS plastic on a laser cutter machine. The finished device, holding two smp samples, is pictured in Figure 8.

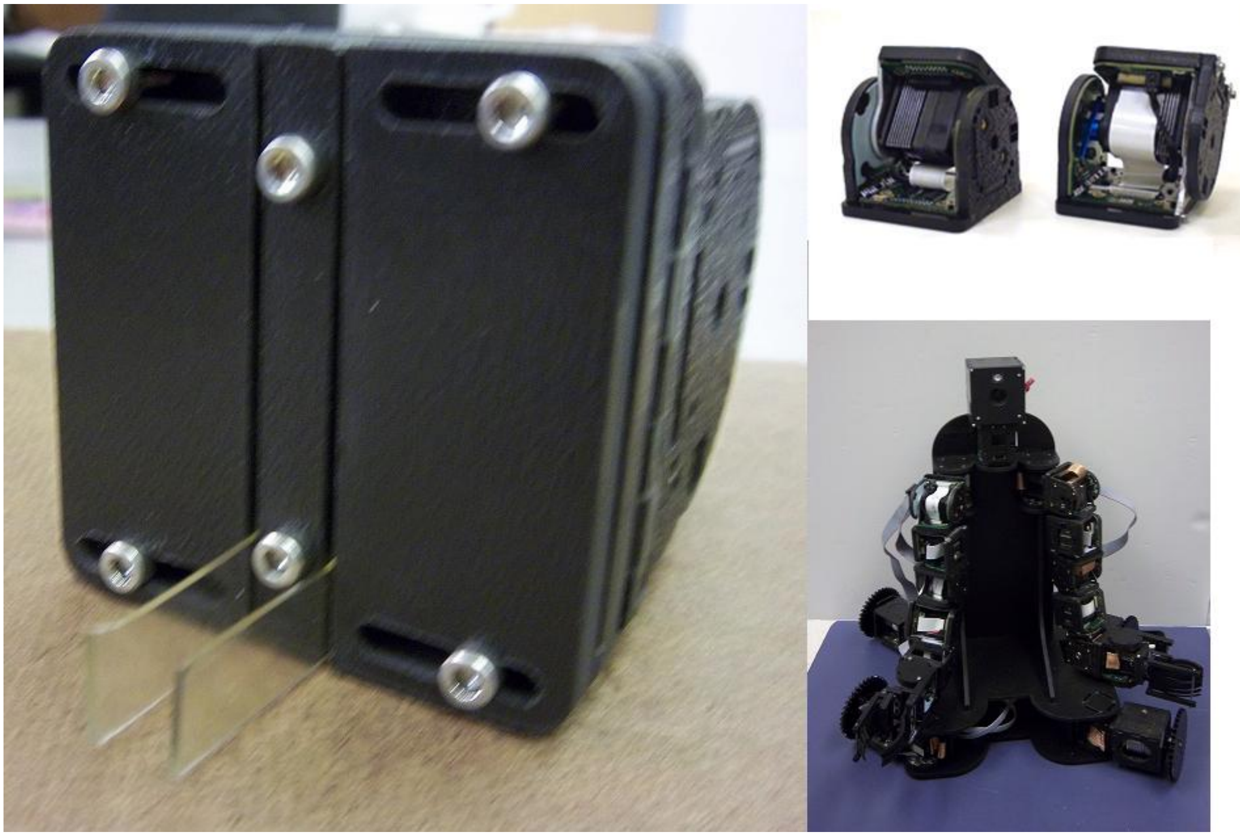

Figure 8. Left: SMP Gripper, attached to the face of a CKbot module. Top Right: CKbot Modules. Bottom Right: Mini-PR2 robot that was programmed to use the SMP gripper.

The gripper is designed to be deformed by heating up the SMPs in the clamps, and then pressing them against a specially designed structure, to deform them to an open gripper shape. Different templates can be used in deforming the gripper to attain different open gripper shapes. I hypothesize that different open shapes will be work more efficiently with differing object sizes and shapes. After being deformed to the open shape of choice, the gripper is then allowed to cool, and can be positioned around an object that needs to be picked up. Then SMP is then heated up again, and the SMPs deform back to their original shape, closing around the object in question.

5. RESULTS

5.1 Steady State Temperature Results

Through the steady state temperature testing, it was determined that a distance of seven inches was optimal placement for the heat gun for ensuring that SMP samples be heated to above their glass transition temperature. At a distance of five inches, the ambient temperature leveled off at a temperature of 130°C, too hot. At a distance of ten inches, the ambient temperature leveled off at a temperature of around 90°C, just slightly above the glass transition temperature. For this reason a distance of 7 inches with the heat gun on medium heat setting was chosen. This ensured that even if there were some alignment errors with the flow of air from the heat gun that we could be confident that the shape memory polymer had reached a temperature above its glass transition temperature. It was also determined that heating for one minute would be sufficient to reach a stable temperature. The graphs of the recorded temperature data at five and ten inches can be seen in figures 9 and 10 respectively.

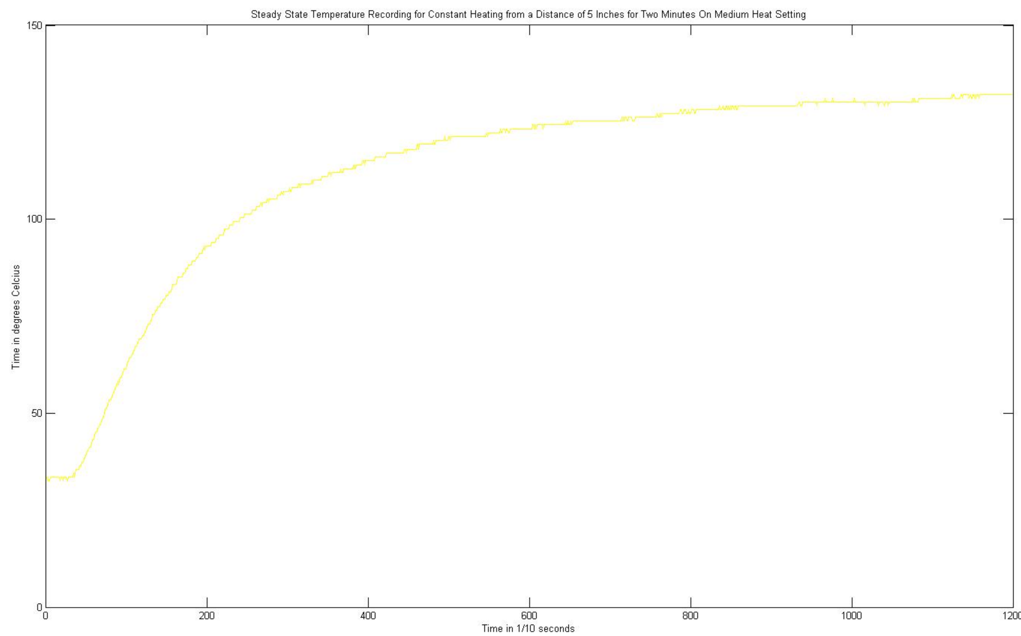

Figure 9. Temperature Recording for Medium Heat from a Distance of Five Inches

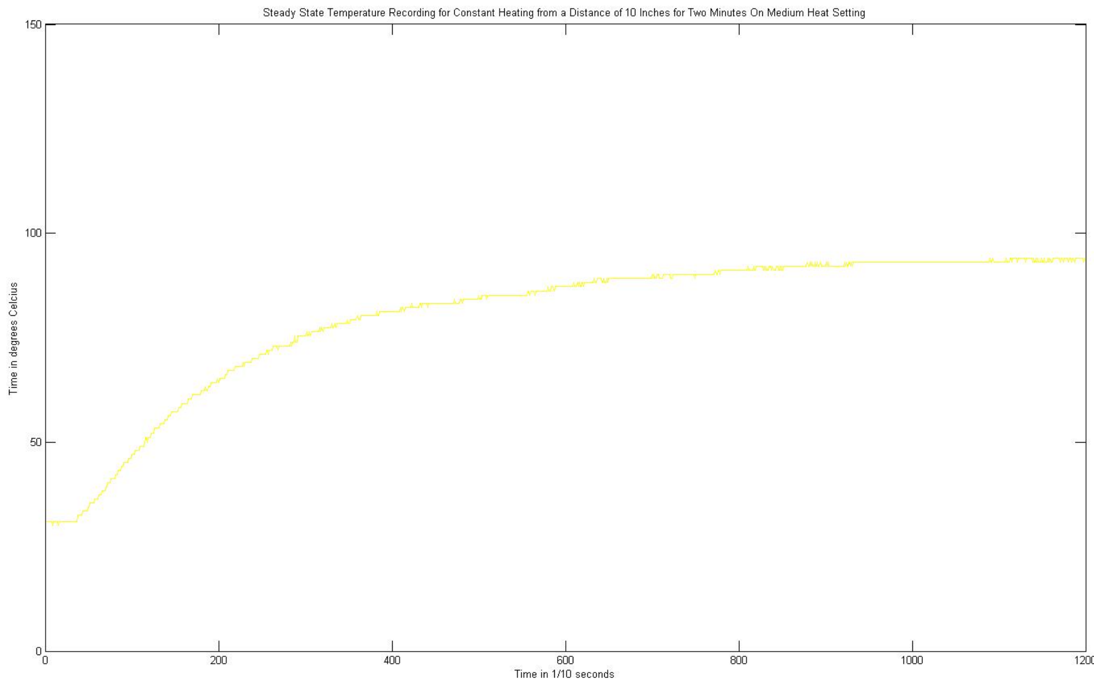

Figure 10. Temperature Recording for Medium Heat from Distance of 10 Inches

5.2 Tensile Testing Results

Before tensile test results on the SMP sample were analyzed, an identical test was ran using ABS plastic, with a known Young's Modulus, to check for accuracy of the results. A linear regression was calculated in the approximately linear region of strain less than 0.5% for each trial, to obtain a value of Young's Modulus. The Young's Modulus values obtained ranged from 35.394 MPa to 54.772 MPa, with an average modulus value of 49.594MPa. These values differ drastically from the expected known modulus of ABS plastic of 2 GPa.

For this reason, it is clear that data obtained from the Instron machine was skewed and inaccurate. For this reason, the stress-strain values obtained during testing of the shape memory polymer are not considered to be accurate. However the stress strain curves for the SMP at room temperature are plotted next to the stress strain curve of the SMP at glass transition temperature for comparison in Figure 11. The data obtained from an SMP at room temperature are plotted in black, and the data for an SMP heated above glass transition temperature is plotted in red.

As can be seen in Figure 11, when the SMP was heated about its glass transition temperature it was able to deform to strains much larger than that of the SMP at room temperature. The average modulus value obtained for the room temperature SMPs at strain greater than 1.75% was 58.716MPa. The Young's modulus obtained for the heated SMP for strain between 9% and 13% was 4.2896 MPa. These strain ranges were chosen because they were the regions in which the stress strain curves for the room temperature and heated SMP were linear. A modulus value was not calculated for the heated SMP at lower strain, even though this section of the graph is also linear, because the polymer experienced some drooping upon heating, and was not truly in tension until strains of around 9%. While none of the these modulus numerical values are considered to be accurate, we can still conclude that the modulus of SMPs at room temperature is more than 13 times larger than the modulus of the SMP heated above glass transition temperature. This indicates that SMPs at room temperature are more than 13 times stiffer than the same SMP when it is heated above its glass transition temperature.

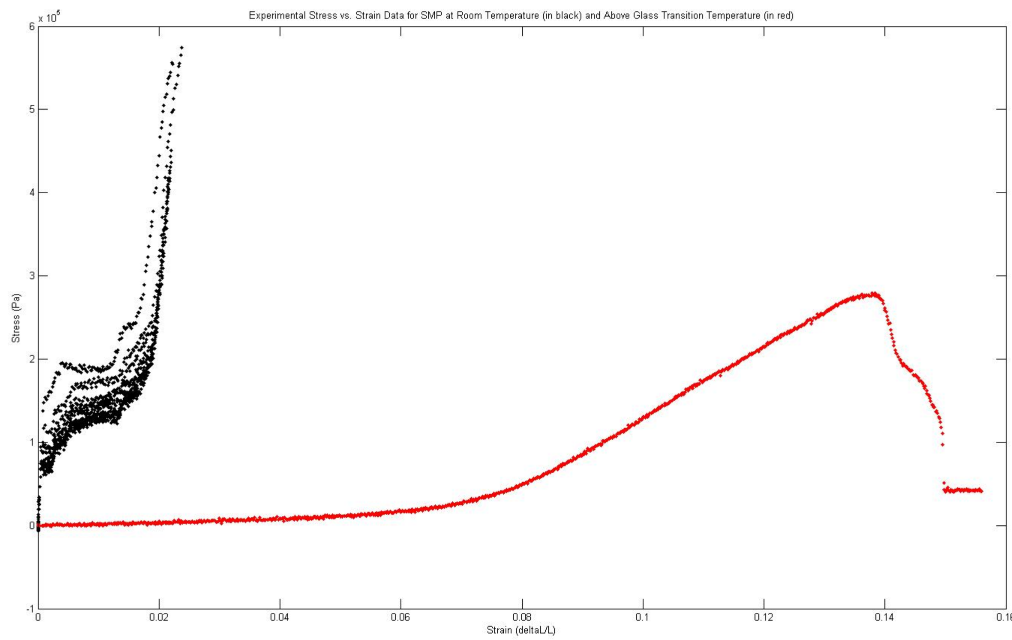

Figure 15. Stress Strain Curves for Room Temperature and Heated SMP.

5.3 Percent Recovery Testing Results

Percent recovery is plotted versus ambient recovery temperature in Figure 16. The green dashed line indicates the shape memory polymer's glass transition temperature. As can be seen from the figure, above the polymer's glass transition temperature, 100% recovery was seen for all trials. In fact, 100% recovery was observed at all temperatures above 70.5°C, 9.5° below glass transition temperature. 100% recovery was even seen at temperatures as low as 63.8°C, although not in all trials. At temperatures lower than this, the percent recovery observed dropped quickly, with recoveries less than 15% below 50°C.

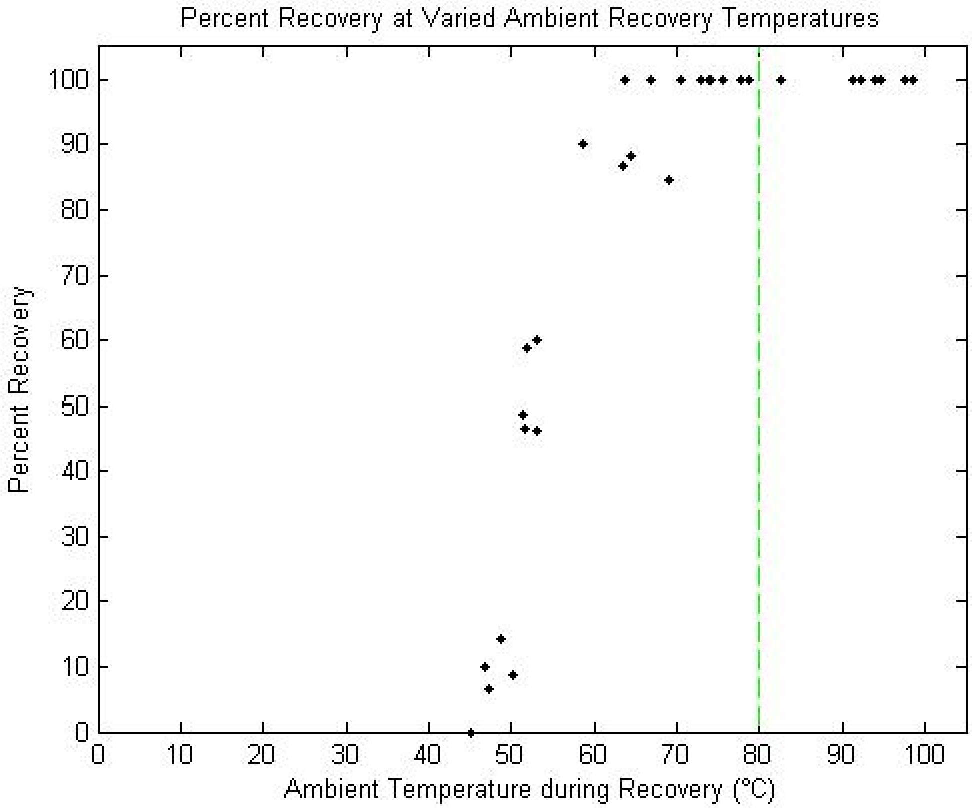

Figure 16. Percent Recovery vs. Ambient Recovery Temperature from SMP bending Test.

Figure 17 plots percent recovery vs. varied stored angles. Stored angles from small to large were all tested at a variety of temperatures ranging from about 30° below glass transition temperature and about 20° above glass transition temperature. As can be seen from the graph, there is no correlation between the value of the stored angle and the percent recovery observed. This indicates that the SMPs on the SMP gripper could be deformed to any shape or angle without affecting the percent recovery, as long as a recovery temperature of close to the glass transition temperature were reached.

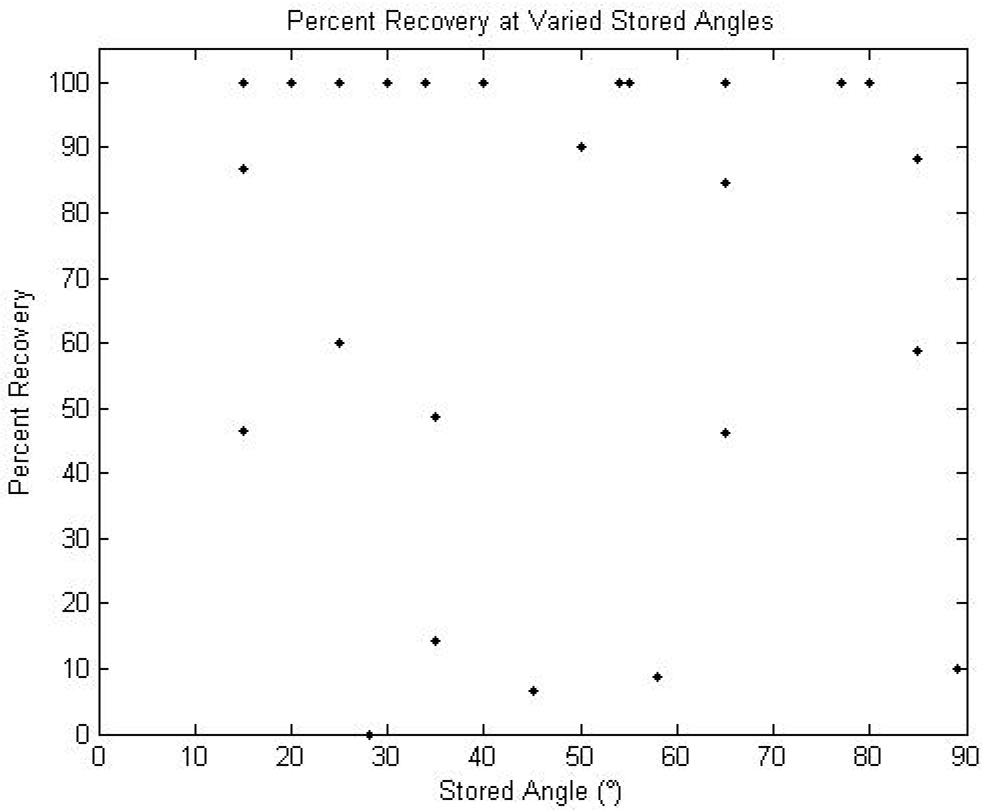

Figure 17. Percent Recovery vs. Stored Angle Value for SMP Bending Test.

5.4 Force Ratio Testing Results

The recovery force of the SMP in grams is plotted against a range of stored angles in Figure 18. As can be seen from this figure, the recovery force is positively correlated to stored angle value. The data follows a trend of increased recovery force for increased stored angle values. The R^2 value for the linear regression of this data is 0.825, indicating a fairly strong correlation. The recovery force ranges from 0.56 grams to 3.11grams.

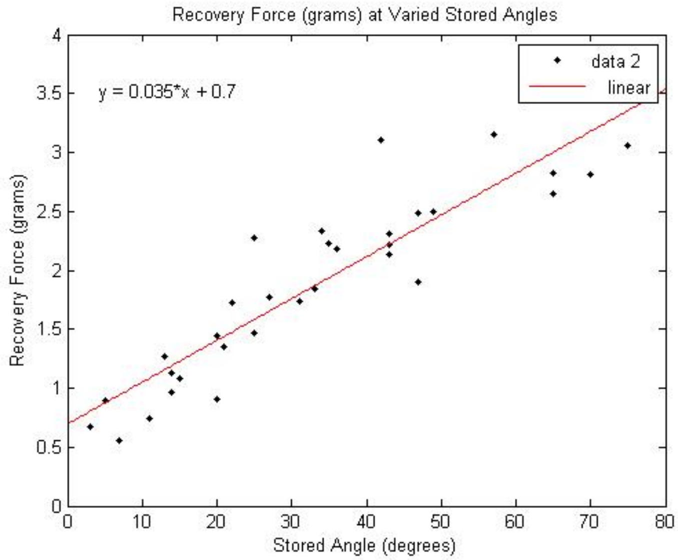

Figure 18: Recovery Force (grams) at Various Stored Angle Values

However, while recovery force increases with greater stored angle values, so does the force to engage the SMP. This can be seen by plotting force ratio against various stored angle values. The force ratio was calculated as the (recovery force)/ (force to engage). Force ratio's greater than one are considered desired results, as this indicates that less energy need be used to engage the SMPs, than for them to recover. As can be seen in Figure 19, the force ratio is close to one across all stored angle values. The R^2 value for the linear regression of this data is 0.05, suggesting that the value of stored angle will not influence the efficiency of the gripper. Larger stored angle values recovery with greater force, but also required greater force to engage.

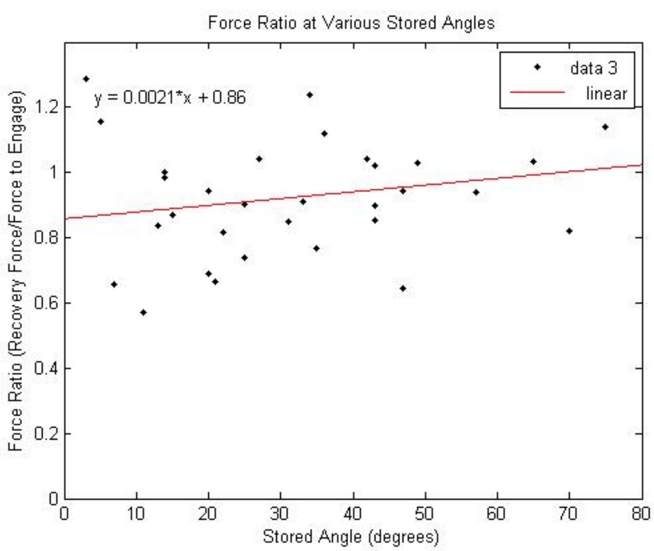

Figure 19: Force Ratio at Various Stored Angles

Figure 20 plots the calculated force ratio's vs. varied recovery temperatures. As can be seen from this figure, the force ratio appears to have no correlation with temperature. A linear regression of the data has a slope of -0.004, near zero, with an R^2 value of .09, indicating that the force ratio does not depend on temperature. In other words, the efficiency of the SMP gripper cannot be improved by manipulating the temperature at which the SMPs recover.

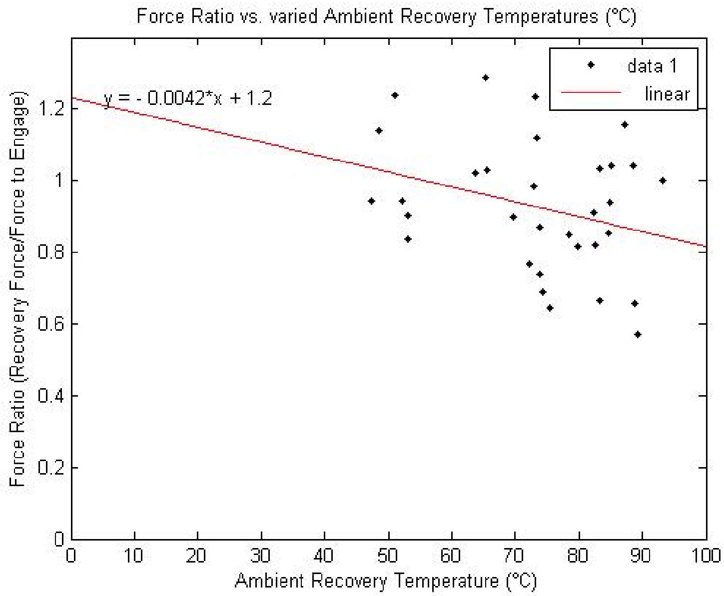

Figure 20. Force Ratio (Recovery Force/Force to Engage) vs. Varied Ambient Recovery Temperatures (°C)

Since the force ratio was not found to be correlated to stored angle or ambient recovery temp, an average force ratio can be taken across all trials. The average force ratio across all of the trials was 0.9265. This indicates that on average, 92.65% of the energy used to engage the SMP to a new stored angle will be exerted back during recovery. While ideally the force ratio should be greater than 1, 0.9265 is still fairly efficient.

Recovery Force increased with larger stored angle values. For this reason, recovery force data was normalized with respect to stored angle value before plotting recovery force vs. ambient recovery temperature. The data was normalized using the following equation: (trial recovery force)*(Maximum Stored Angle/trial Stored Angle). The Maximum stored angle was 75, the largest angle for which force data was collected. This scaled the recovery force data, by increasing the recovery force for angles smaller than 75. This scaled data is plotted in figure 21 vs. ambient recovery temperature. The R^2 value for the linear regression is .0004, indicating that the ambient recovery temperature has no correlation with the recovery force.

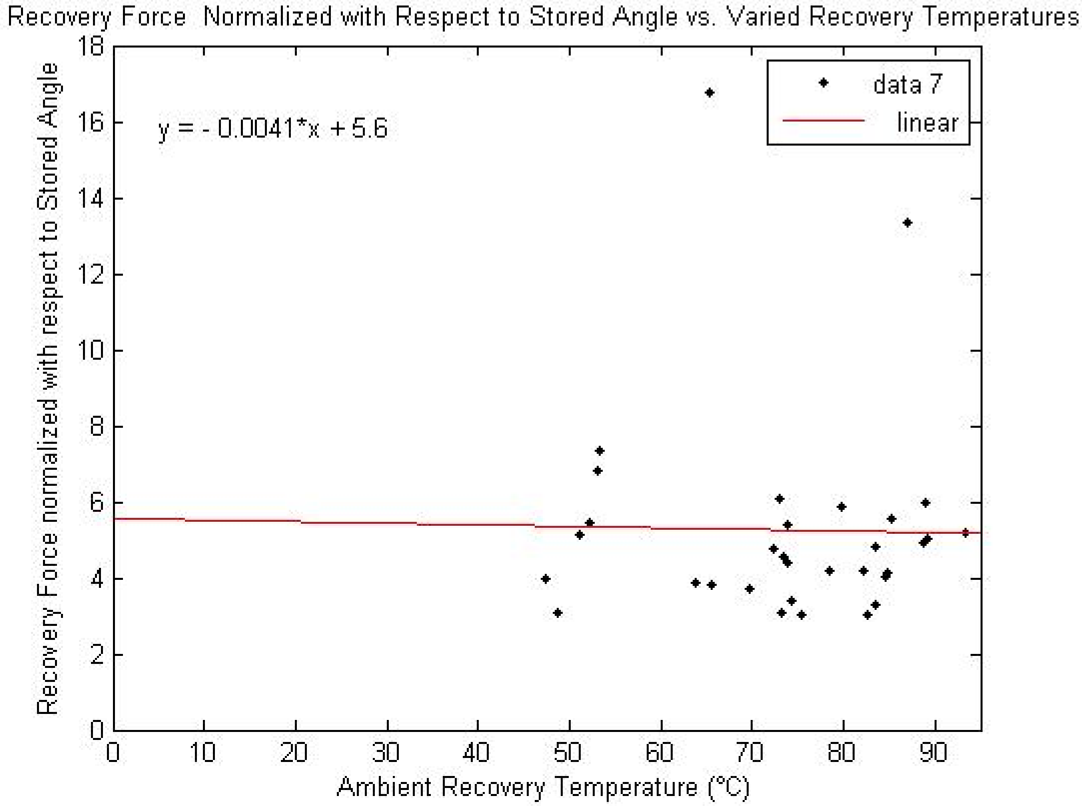

Figure 21: Recovery Force Multiplied by a factor of Max Angle/Trial Angle vs Various Ambient Recover Temperatures.

In order to obtain an estimate of the maximum weight the SMP gripper could pick up, recovery force data was averaged across all trials. The average force recovery was found to be 1.86 grams. This can be considered a conservative estimate for average force recovery since trials in which small stored angles were used are included in this average. Since force recovery increased with greater stored angle, an average was also calculated for those trials in which the stored angle was greater than 40°. 12 trials out of 32 were conducted with stored angles greater than 40°. The average force recovery for this data set was 2.60grams. This is probably a more realistic force recovery estimate for application with the SMP gripper, as it is unlikely the SMPs mounted on the gripper will be deformed for practical use to angles less than 40°. The maximum recorded recovery force across all trials was 3.15grams.

5.5 Static Friction Testing Results

The average value for μ, the coefficient of friction, between aluminum and the SMP samples was found to be 0.61. The average value for μ between the rough side of ABS plastic and the SMP samples was found to be 0.62. The average value for μ between the smooth side of ABS plastic and the SMP samples was found to be 0.64. While it seems unusual that a higher value for the coefficient of friction was found for the smooth side of ABS than the rough side of ABS, this is likely because the dimpled nature of the rough side of ABS plastic allowed for less contact between its surface and that of the SMP.

5.6 SMP Gripper Testing Results

Based on the force ratio testing, the maximum weight of an object that could be picked up with the SMP Grippers was determined. This weight was calculated by multiplying the maximum recorded recovery force, 3.15grams, by the highest of the three recorded coefficients of friction, 0.64. This predicted that the maximum weight object that the SMP grippers would successfully pick up would be 2.02grams. However a more conservative estimate of recovery force obtained by averaging across all trials was 1.86 grams. Multiplied by 0.64, this estimates that the gripper should be able to pick up objects of at least 1.19grams. For this reason, objects weighing 1 gram were used in initial testing of the SMP gripper. This limited the likelihood that a failed lift attempt could be attributed to the force of the SMPs. Since it was observed that recovery force increased with greater stored angles, we beleive that if the SMP gripper were deformed to larger angles then it would be able to pick up heavier objects. Two of the designed structures to be used in deforming the smp gripper's to an "open" position provided successful lifts of an object. These two configurations are shown in Figure 22. Configuration A allows the SMP's to be deformed into a circular shape. Configuration B allows the SMP's to be deformed into an open V shape

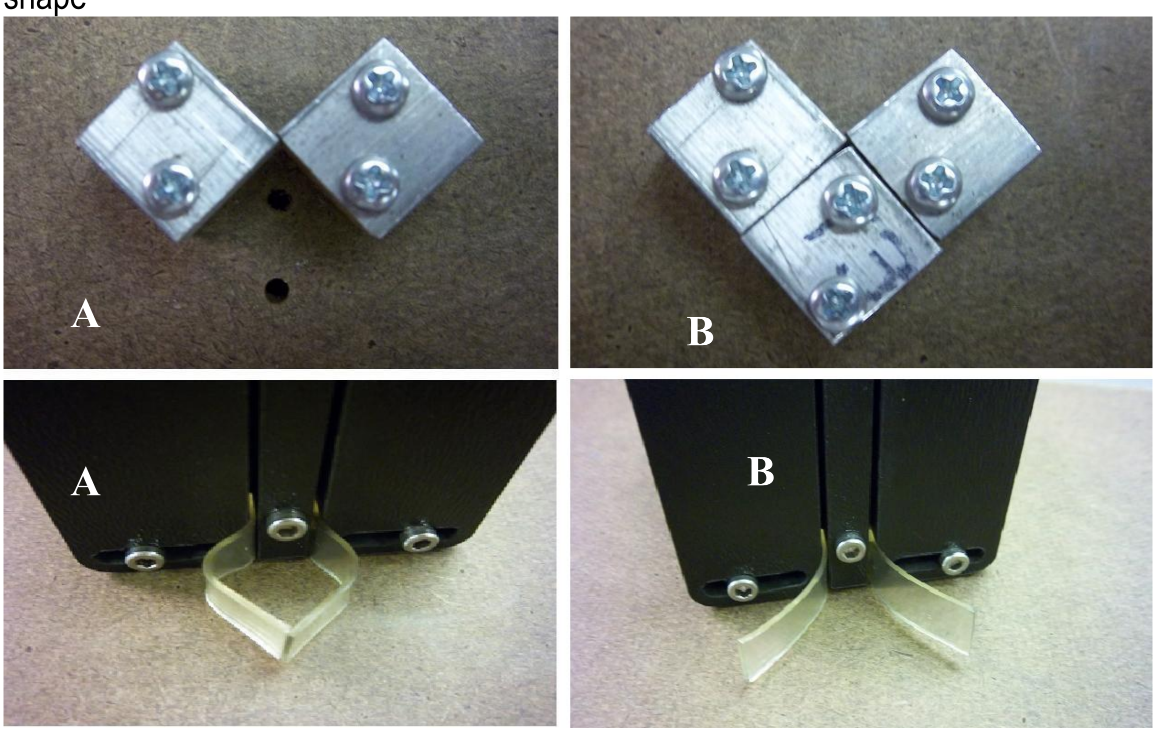

Figure 22: Two block configurations used to deform the SMP gripper to an open position. Both resulted in successful lifts.

For both of these configurations, ten attempts at picking up the same object were conducted, keeping conditions consistent. The SMPs on the gripper were heated for 45 seconds from 7 inches away with medium heat from the heat gun. Then the gripper was pressed into the configuration deforming the SMPs, and was allowed to cool for three minutes maintaining force against the configuration. Three minutes to cool was chosen because this was the minimum time that allowed the polymers to cool to a temperature that would guarantee they would maintain their current shape. The gripper was then positioned in place for picking up a small plastic tube connector, weighing one gram, and then the SMP's were heated again for 45 seconds from seven inches away. The SMP gripper's were allowed to cool for another three minutes before the gripper was picked up to test for successful lift of an object. A successful lift was considered lifting the blue plastic piece off the table top and maintaining grip on the object as the gripper's orientation was inverted. For both of the configurations used, nine out of ten lift attempts were successful. For this reason they are considered equally valuable methods of deforming the SMP, and each one could prove advantageous in picking up objects of varied shape. Also, since the configurations are the inverse of one another, it was decided that a platform be created that could mount either of these configurations

Once the platform was created, the SMP gripper was installed on the mini-PR2 robot, and the robots graphical user interface (GUI) was used to program the robot to use the smp gripper. The GUI allows the robot to memorize a sequence of positions to move between. The motion necessary to deform open the smp gripper, place the open gripper around an object and then lift and move the object were programmed. The mini-PR2 was then able to successfully use the SMP gripper to pick up the tube connector weighing one gram. Configuration B was used during the mini-PR2 demonstration because the open V shape gripper was more forgiving on alignment errors when approaching an object.

6. DISCUSSION AND CONCLUSIONS

Tensile testing conducted on the Instron Model 5544 Electromechanical Test System did not yield reliable results. It is possible that the clamps used to protect the shape memory polymer samples allowed for some slipping of the samples, giving inaccurate stress-strain results. However even when testing a tensile sample of ABS plastic without the metal clamps, data did not yield a modulus close to the known value of 2GPa. For this reason I suspect that there was some malfunction with the Instron's calibration or grip function. For meaningful stress-strain curves, tensile tests need to be repeated using another mechanical testing system.

It was found that 100% recovery could be observed for stored angles less than 90° at ambient recovery temperatures greater than 70.5°C. This indicates that for repeatable use of SMPs, an ambient temperature of at least 70.5°C must be reached during recovery.

Force testing and static friction tests predicted that the SMP samples used in this research could lift a maximum weight of 1.5 grams. A SMP gripper prototype and corresponding apparatus for deforming the gripper to an open position were manufactured, and successful lifts of an object weighing one gram were demonstrated. This prototype compatible with the existing modular robot PR2 in Dr. Mark Yim's laboratory at University of Pennsylvania, and the robot was programmed to successfully use the gripper. However more work must be conducted to make this gripper stronger, more autonomous and reversible.

The SMP components of this device are low cost and well suited for mass production. With the proper equipment, the components of the polymer could be melted and combined in large batches and then poured into large molds that could be cut into thousands of SMP pieces for the gripper. As opposed to traditional gripper material, this would be a much easier, lower cost, production method. In addition, since all plastic components of the device were cut from a laser cutter, this process could also be done on large scale fairly quickly and efficiently. Despite these possibilities there are still many hardware design improvements necessary before an entire module could feasibly be mass produced at low cost.

7. RECOMMENDATIONS

While the SMP gripper developed in this research was successful in picking up an object weighing one gram, there are several recommendations for future improvements on this device.

Additional effort must be taken in developing a method to heat up the SMPs autonomously. A proposed solution to this problem is circuitry with resistive wires that would heat up when current was applied across them. These wires could be formed around or even placed within the SMP. The effect of such additional wires on the SMP's percent recovery and force would need to be tested also. Another possible solution would be to mount a heat gun or similar heating element on the base of the PR2 robot that could be autonomously turned on and used to heat SMPs. It may be helpful in these efforts to manufacture a SMP with a lower glass transition temperature, as it would make reaching glass transition temperature easier.

Incorporation of any of the composite materials discussed in section 2.4 of this paper, including carbon black, Nickel, or short fibers, into the SMP samples used with this gripper could aid in autonomous heating of the SMPs. Addition of these types of materials can improve the polymer's conductivity. If the polymer was more conductive, it may be possible to apply a current directly across the polymer to heat it up, or speed up the heating process if a resistive wire still needed to be used.

In order for the SMP gripper to able to pick up a wider range of objects, the force and strength of the SMP samples used must be improved. The continuous fiber reinforced SMP composite developed by Lan et al [7] looks particularly promising in improving mechanical properties of SMPs and may work well with the SMP Gripper.

Finally, the current SMP gripper prototype is not reversible. In other words, there is no method of reopening the gripper once it has picked up an object besides deforming it again against the apparatus used to open it initially. However this means that an object could not be released and placed in a desired position. Future work will need to develop a method of making the SMP gripper reversible. This could be done by having an antagonistic actuator placed in opposition to the SMP grippers. A shape memory alloy could potentially be used as this antagonistic actuator.

8. ACKNOWLEDGEMENTS

I would like to thank Paul White, graduate student at the University of Pennsylvania, with whom I collaborated extensively with on this project. I would also like to thank Dr. Mark Yim, of the University of Pennsylvania, for allowing me to work as a part of his research team and for his help and guidance on this project throughout the summer. I would like to thank Chi-mon Chen, a graduate student in Material Sciences at the University of Pennsylvania, for providing me with training on fabricating the shape memory polymers. In addition, I would like to thank Dr. Jan Van der Spiegel of the University of Pennsylvania for his encouragement and support of myself and all the other SUNFEST Students. Finally I would like to thank the NSF for funding of the Summer Undergraduate Fellowship in Sensor Technologies, an excellent opportunity for undergraduates to gain research experience with interesting and challenging projects.

References

[1] Kasper Stoy, David Brandt, and David J. Christensen, *Self-Reconfigurable Robots - an Introduction.* Cambridge, Massachusetts: MIT Press, 2010.

[2] M. Yim, W. M. Shen, B. Salemi, D. Rus, M. Moll, H. Lipson, E. Klavins and G. S. Chirikjian, "Modular self-reconfigurable robot systems [grand challenges of robotics]," *IEEE Robotics & Automation Magazine,* vol. 14, pp. 43-52, 2007.

[3] P. J. White and M. Yim. Scalable modular self-reconfigurable robots using external actuation. Presented at Proceedings of IEEE/RSJ International Conference on Intelligent Robots and Systems.

[4] K. Ikuta, "Micro/miniature shape memory alloy actuator," in *1990 IEEE International Conference on Robotics and Automation, Cincinnati, OH,* 1990, pp. 2156-2161.

[5] G. Lim, K. Park, M. Sugihara, K. Minami and M. Esashi, "Future of active catheters," *Sensors and Actuators A: Physical,* vol. 56, pp. 113-121, 1996.

[6] T. Xie and I. A. Rousseau, "Facile tailoring of thermal transition temperatures of epoxy shape memory polymers," *Polymer,* vol. 50, pp. 1852-1856, 2009.

[7] X. Lan, Y. Liu, H. Lv, X. Wang, J. Leng and S. Du, "Fiber reinforced shape-memory polymer composite and its application in a deployable hinge," *Smart Mater. Struct.,* vol. 18, pp. 024002, 2009.

[8] H. Tobushi, S. Hayashi, Y. Sugimoto and K. Date, "Two-Way Bending Properties of Shape Memory Composite with SMA and SMP," *Materials,* vol. 2, .

[9] National Semiconductor Corporation. (2010, LM35 precision centigrade temperature sensor. *2010(6/10)* .

Advanced Teleoperation Control System for PR2 Humanoid Robot

NSF Summer Undergraduate Fellowship in Sensor Technologies
Carlos Torres Casiano (Electrical Engineering) - University of Puerto Rico at Mayagüez
Jason C. Carter (Industrial Engineering) – Morgan State University
Advisor: Dr. Camillo J. Taylor

Abstract

The ultimate achievement in robotics is to build a robot that can perform perform a range of tasks by human. One such robot that is getting closer to this ability is the PR2 humanoid robot, from Willow Garage. The PR2 has capabilities that allow the user to program different movements in order to achieve multiple assignments. Being an open source robot, the PR2 allows users to read previous codes and manipulate them in order to complete new tasks. The purpose of this research is to output what the PR2 sees to the Head Mounted Display (HMD) worn by the user, and control the PR2's head with a motion tracking system (Vicon). The Vicon system captures the movement of markers placed along the HMD, and outputs an array of numbers that will go through a Python code in order to retrieve the necessary coordinates. These coordinates are sent to the PR2 which will enable it to move the head to the specific point in space. With all the components working together the user is capable of manipulating the PR2's sight for his own use.

1. Introduction

In past decades robots have been developed for use in industry, war, and other areas to assist human needs. Robots are useful to society for completing tasks that are constantly repetitive or are dangerous for people. They can also help people who, because of disease or disability, are unable to perform some basic tasks. One such robot, the PR2, is a humanoid robot developed to complete simple tasks done by people.

The major aspect of this robot is the control system, ROS, used to implement and control the different sensors and cameras on the robot's body. These cameras and sensors let the user see what the robot is watching. Images captured by PR2 go through the ROS operating system and are sent to the computer. A recent addition to some control systems is a head-mounted display (HMD) worn by the operator. If an HMD is present, the input images of the computer output to the HMD. Continuous advancements in robotics have led to the need for newer and more powerful control systems. To improve the functionality of these new robots and give them more human-like abilities, more technology needs to be integrated into them. Typical robotic control uses a visual navigation system with a stationery camera. However, the user would then have to turn the whole robot to turn the camera. The goal of this research project is to build a device to allow a link between a user's head movement and the robot's head movement. Instead of using basic computer screens and panels to view what the robot sees, the user will wear an HMD and see what the robot sees in real time as well as control its motion.

In order to track the pan and tilt motion of the user wearing the HMD, a motion tracking system is required. This system would detect the pan and tilt motion of the HMD, and relay that information into a digital format so we can use it to control the robot's head. Previous studies by the University of Texas at Austin [1] have shown that a humanoid robot's body can be controlled with the use of a motion tracking system. Movement of a user's arms and legs will move the corresponding parts of the robot. Also, research completed at the University of Pennsylvania has shown the versatility and accuracy of using a motion tracking system [2] to control helicopters. For our research a series of cameras will pick up the motion of the HMD and relay its coordinates to a standby computer which will interpret the data for the ROS code.

Each of the following components will work together in a system to make this project possible. The HMD movements from the motion capture system will be mapped in the computer. When the user pans or tilts his head, a signal will be sent to the PR2 to move its head accordingly. The PR2 will interpret the data via an elaborate ROS code. Data images from the PR2 will be sent to the HMD worn by the user in real time.

2. Background

2.1 PR2

PR2 is a humanoid robot built and donated by Willow Garage to universities for research opportunities. Being a humanoid allows PR2 to accomplish small chores, and it can adapt to changes in its environment. The PR2 consists of a head, two arms with grippers, and a base. The head contains two stereo cameras with LED pattern projector, a 5MP camera, laser range finder and an inertial measurement unit (IMU). The forearms each contain an Ethernet-based, wide-angle camera, while the grippers have three-axis accelerometers and pressure sensor arrays on the fingertips and the base has a fixed laser range finder. The PR2 uses ROS, an open-source, meta-operating system in order to communicate with the computer.

PR2 is a ROS-based which allows it to be reprogrammable, able to complete different tasks like folding towels, plugging cables, playing pool and opening doors among other things. Using the ROS system, PR2 is able to employ complex algorithms, being capable of attacking a problem continuously until it can achieve the goal. For example trying to plug its power cable to an outlet, PR2 continues to calculate to reposition its arm until achieving the goal. It is also capable of using sensors to generate a 3D map of its surroundings, as well as promptly compute unexpected changes in the environment.

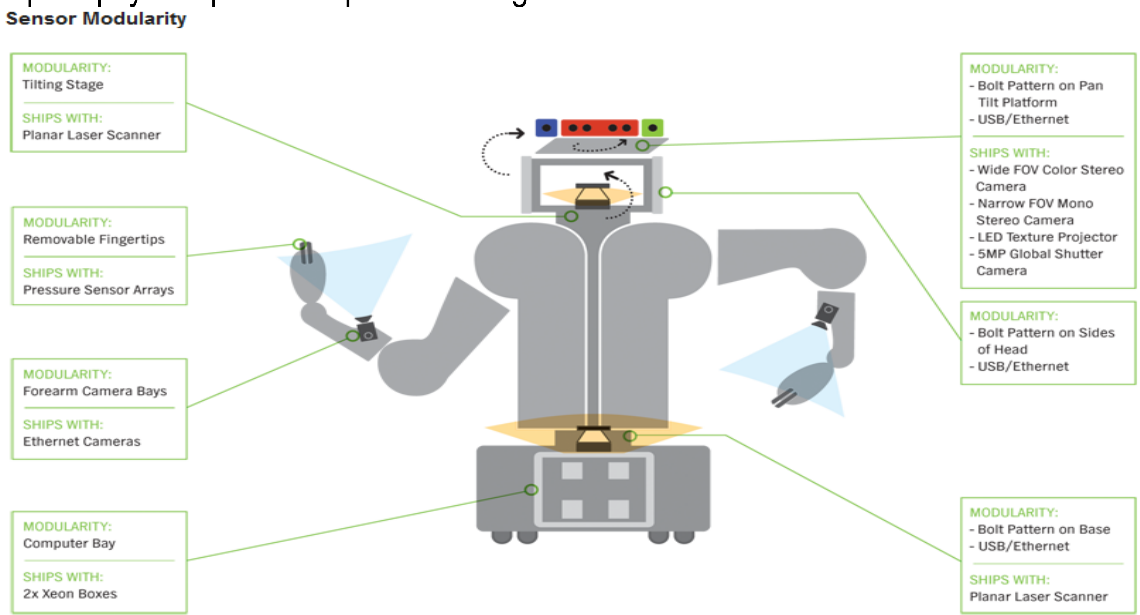

Figure 1: PR2 Sensor Modularity [3]

2.2 Motion Capture System

A motion capture camera, in this case Vicon, allows the user to record movement of people or objects and digitalized into a computer. This animation data is mapped to a 3D model to obtain the exact movement of the actor. Special markers that reflect infrared light are attached to the object by the user and then picked up using multiple cameras in the system, infrared light is then sent to the points attached and reflected to the cameras where they can map the form and position. This digital simulation can be used to draw a path for the programmable object, to study human movements, and to create movies, video games, etc.

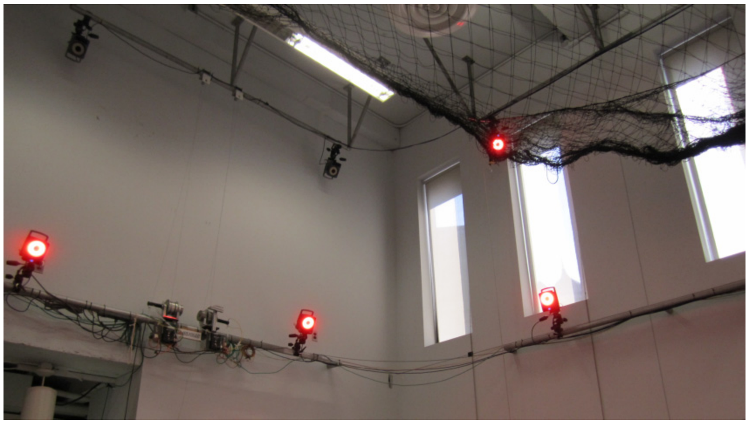

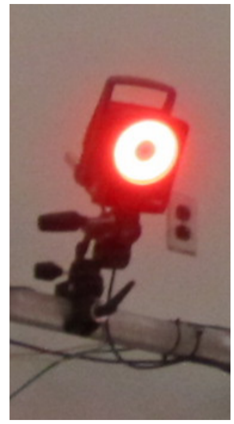

Vicon Motion Tracking System Infrared Camera

2.3 Head Mounted Display (HMD)

Using the Vuzix Wrap 920, an HMD with two displays in each lens, the user can see in real time the exact thing PR2 is watching. This is a key object in the research since the points of the Motion Caption System will be placed along the HMD.

Vuzix Wrap 920

3. Materials & Methods

All three major components in this project, PR2, HMD and Vicon Motion Capture System, are well synchronized to have the desired outcome. Each of these components communicate with one another through a series of computer code. The Vicon system receives the points of the HMD through its system, the points are then sent to the PR2 wirelessly through a computer, the PR2 sends its video output to the HMD.

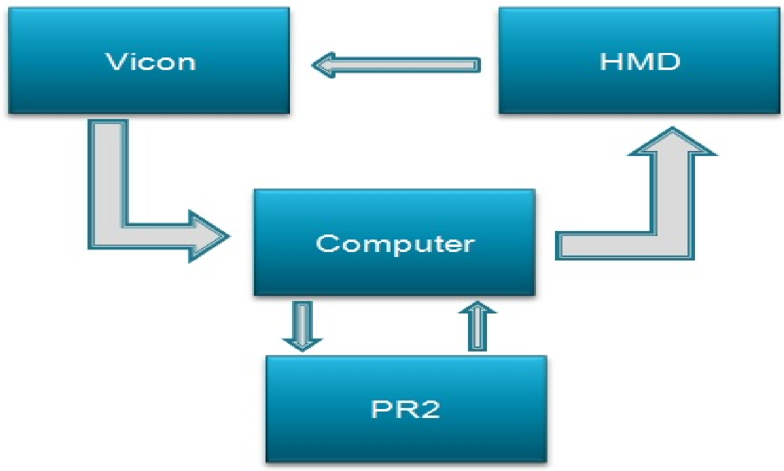

3.1 PR2

The PR2, a humanoid robot made by Willow Garage, has various functions and abilities. We are mainly focused on its head movement and the camera inside. Using an open source code for head movement (Fig. 2), we were able to manipulate the head so that we could input our own movements. In lines 19, 20, and 21, there are movements for the associated X, Y, and Z motions. The inputs for the code came from the Vicon System and were compiled on the code we made (FIG. 1), and the coordinates generated from that were imported into the ROS open source code for the PR2.

3.2 Vicon Motion Tracking System

The motion tracking system uses a series of infrared cameras that captures the position of sets of markers within its range. The HMD used for this project was aligned with markers along the frame, and the Vicon system picked up the markers and displayed a frame of the HMD on the computer's screen. Along with these points on the screen from the HMD, the Vicon system displayed a series of points where the glasses were in space. The system continuously displayed these points as the glasses moved through the Vicon system

3.3 Vuzix Wrap 920

In order to receive images from what the robot sees, we decided to use the Vuzix Wrap 920 as the head mounted display. The Vuzix Wrap supplies vision to both eyes of the user in a resolution of 680 x 480, and is equipped with USB and VGA connections. The PR2 is connected to a computer, and the PR2's head camera is shown on the computer. With the supplied connectors, the Vuzix is capable of displaying what is on the computer screen, like an external monitor. The user is then able to see what the robot sees through this manner.

3.4 Programming Code

A. Vicon

The first step for the programming code is to pull the values from the Vicon System. The system outputs a series of “tupled” data, and we only need to pull out a series of values from that data. This code connects the external computer to the Vicon System and pulls out the data that we need (Fig. 5). The data is a set of values that relate to the rotation of the HMD within the system. The values are displayed in radians from the center axis of the Vicon and the HMD (Fig 8).

B. Vicon to PR2

The pulled values then need to be converted into something the PR2 can understand. This code takes the pulled numbers, converts them to degree movements to the corresponding X, Y, or Z movement, and puts it into a ROS code for the PR2 (Fig. 6). As the HMD is rotated through its axis, pan motion, X and Y, and tilt motion, Y and Z, are relayed to the PR2.

C. PR2 to HMD

The PR2 has a camera inside of its head unit. Through one of the ROS codes we can communicate with the camera and display what the PR2 views onto the computer screen. This code allows for that communication and displays the images from the PR2 onto the fullscreen of the computer (Fig. 7). Since the HMD works as an external monitor connected to the computer, the fullscreen view gives the user a complete view from the PR2 and not just in a specified window.

4. DISCUSSION & RESULTS

The purpose of this research project was to create a way to control the head motion of a robot, the PR2, only by moving one’s head, as well as to see what the robot is seeing. The idea was to use a Head Mounted Display to see what the robot sees, and then use a motion tracking system to send the relative points of the user moving his head to the robot. This is an ongoing study that in the end, the idea is to be able to have a robotic avatar; to program the robot to essentially mimic the movements of the user. This setup was just the beginning with vision and controlling from the head. In order for full body movement, the next task would be to generate codes for arms and velocity directions for the robot, and still using the motion tracking system to receive points from the user’s body to input into the code.

Upon conclusion of this project, we were able to control the PR2’s head with basic pan and tilt motions of our head. While wearing the glasses we were able to locate objects around the PR2 while in a different location. The idea was to test the capabilities of the HMD and the PR2. The user would search the room that the PR2 was in and locate an object that was previously shown to him, and then describe where it was located. Another task was to read a small selection in front the PR2 that the viewer could see through the HMD he was wearing. These two tasks tested the capability of the completed project, how well it works, and how clearly the vision is at particular distances.

Results- Controlling the Head

Along the journey of completing this project there have been a few challenges. One of the biggest was connecting the entire system together. The PR2 and Vicon System needed to be connected on the same system in order to communicate the points in the code. A set of concurrent IP addresses needed to be made for the two components, and a computer connected to the Vicon system was used to integrate them together. A separate computer was also needed to connect the PR2 to the HMD and the problem was running Ethernet cables to the PR2 to both and having a dedicated network setup for everything to run on. Another challenge was the creation of the code that would take data from the Vicon system, compile it, and sent it to the PR2 for head moment. We first had to learn how the Python and Emacs programs work. Upon learning the scripts, we were able to generate a code that takes two different angle degrees, first for XY coordinate, second for YZ coordinate, as well as a height set for the height of the PR2, and then compiles the sets to determine where the PR2 would look.

The code that communicates the motions of the HMD worn by the user through the Vicon System to the PR2 does so through a series of steps. The Vicon generates a value of movement, the PR2 receives the value modified from the code, the PR2 then executes the motion, and this cycle is repeated continuously. The problem is that when a movement by the user does not coincide with the a movement that the PR2 can make, such as a complete ninety degree turn of the head up or down, the cycle is not complete and the PR2 "locks" and exits the code.

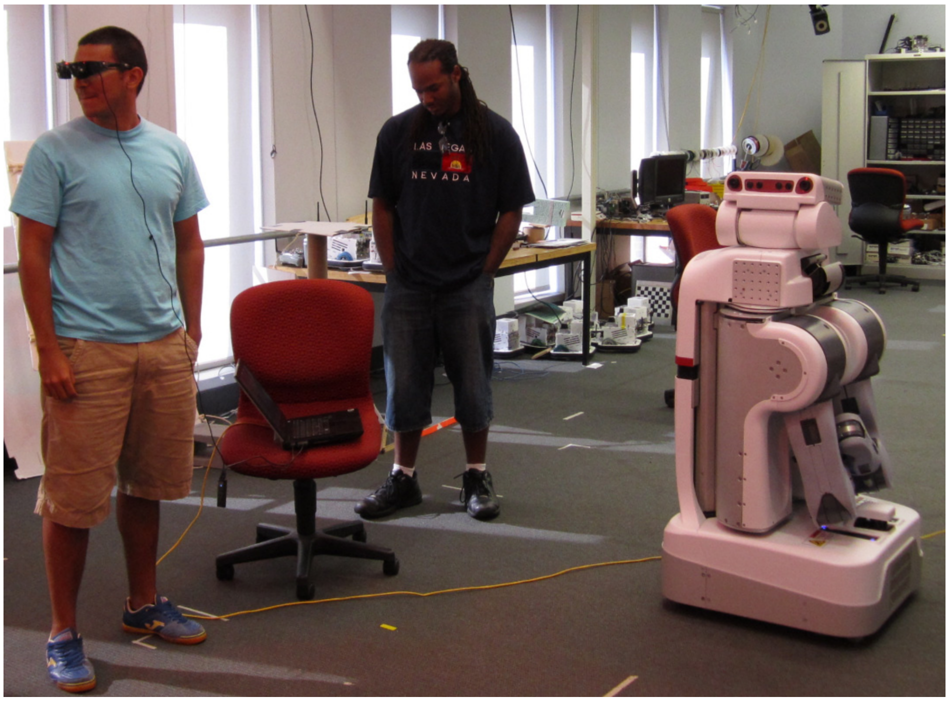

Controlling Head

5. Acknowledgments

We would like to recognize several people and organizations for making this all possible this summer. SUNFEST and Dr. Jan Van Der Spiegel made it possible for us to be here and participate in the research. As well as the Electrical Systems Engineering here at U Penn, for hosting the SUNFEST program. In addition to U Penn, we would like to thank the National Science Foundation for the grant funding the program as well as ARTSI too.

We would also like to thank Dr. C.J. Taylor who guided us through this whole endeavor, as well as his graduate student Anthony Cowley, who helped us learn the software that we needed in order to complete the tasks.

6. References

[1] Adam Setapen, Michael Quinlan, and Peter Stone, *MARIOnET: Motion Acquisition for Robots through Iterative Online Evaluative Training*. May 2010. University of Texas at Austin.

[2] D. Mellinger, “Quadrotor”, fling.seas.upenn.edu. June 11, 2010. [Online]. Available: http://fling.seas.upenn.edu/~dmel/wiki/index.php?n=Main.Quadrotor. [Accessed June 29, 2010]

[3] Willow Garage, “PR2 Overview”, willowgarage.com. Copyright © 2008-2010. [Online]. Available: http://www.willowgarage.com/pages/robots/pr2-overview. [Accessed June 29, 2010]

[4] ROS Wiki, “Documentation”, ros.org. Licensed under ‘Creative Commons Attribution 3.0’ [Online] Available: http://www.ros.org/wiki/. [Last Edited June 3, 2010]

7. Appendix

Code to find x, y, z coordinates from angle inputs:

```
from math import *
def locate(az, el, height):
    pan = radians(az)
    tilt = radians(el)
    Y = cos(tilt) * cos(pan)
    X = -cos(tilt) * sin(pan)
    Z = sin(tilt) + height

    print ' X: '+ str(X) + '\n Y: ' + str(Y) + '\n Z: ' +
str(Z)
    return (X,Y,Z)
```

FIG 1. 3D CODE; DEGREES à COORDINATE

ROS code to control the head of PR2:

```
#! /usr/bin/python
import roslib
roslib.load_manifest('mm_teleop')

import rospy
import actionlib
from actionlib_msgs.msg import *
from pr2_controllers_msgs.msg import *
from geometry_msgs.msg import *

rospy.init_node('move_the_head', anonymous=True)

client = actionlib.SimpleActionClient(
    '/head_traj_controller/point_head_action',
PointHeadAction)
client.wait_for_server()

g = PointHeadGoal()
g.target.header.frame_id = 'base_link'
```

```
19 g.target.point.x = 1.0
20 g.target.point.y = 0.0
21 g.target.point.z = 1.0
22 g.min_duration = rospy.Duration(1.0)
23   24 client.send_goal(g)
25 client.wait_for_result()
26
27 if client.get_state() == GoalStatus.SUCCEEDED:
28     print "Succeeded"
29 else:
30     print "Failed"
```

FIG 2 ROS CODE (We still need to edit to add links for lines 19, 20, 21)

Vicon Code

```
#include <string>
#include <vector>
#include <ros/ros.h>

#include <vicon/Names.h>
#include <vicon/Values.h>
#include "ViconDriver.h"

ros::Publisher pub_names;
vicon::Names names_msg;

void names_callback(const ros::TimerEvent& e)
{
  pub_names.publish(names_msg);
}

int main(int argc, char** argv)
{
  ros::init(argc, argv, "vicon");

  ros::NodeHandle n("~");

  pub_names = n.advertise<vicon::Names>("names", 100, true);

  ros::Publisher pub_values
    = n.advertise<vicon::Values>("values", 100);

  vicon::Values values_msg;
  n.param("frame_id", values_msg.header.frame_id,
          string("vicon"));
  const int buff_len = 1024;
  const int num_buff = 10;
```

```
const bool stream = true;
ViconDriver vd(buff_len, num_buff, stream);

vector<double> values;
vector<string> names;

string server;
n.param("server", server, string("alkaline"));
int port;
n.param("port", port, 800);

// Connect
if (vd.ConnectTCP(server.c_str(), port))
  {
    ROS_FATAL("%s: failed to connect to %s:%i",
              ros::this_node::getName().c_str(),
              server.c_str(), port);
    return -1;
  }

// Start device
if (vd.StartDevice() != 0)
  {
    ROS_FATAL("%s: could not start device",
              ros::this_node::getName().c_str());
    return -1;
  }

//get names (buffered in the driver)
if (vd.GetNames(names) != 0)
  {
    ROS_ERROR("%s: could not get names",
              ros::this_node::getName().c_str());
    return -1;
  }

names_msg.names.resize(names.size());
std::copy(names.begin(), names.end(),
          names_msg.names.begin());

values_msg.values.resize(names.size());

ros::Timer timer = n.createTimer(ros::Duration(1),
                                 names_callback);

while (n.ok())
  {
```

```
      //get values
      if (vd.GetValues(values) != 0)
        {
          ROS_INFO("%s: could not get values",
                   ros::this_node::getName().c_str());
          continue;
        }

      if (names.size() != values.size())
        {
          ROS_INFO("%s: names size does not match values size",
                   ros::this_node::getName().c_str());
          continue;
        }

      std::copy(values.begin(), values.end(),
                values_msg.values.begin());

      values_msg.header.stamp = ros::Time::now();

      pub_values.publish(values_msg);

      ros::spinOnce();
    }

  if (vd.StopDevice() != 0)
    {
      ROS_FATAL("%s: could not stop device",
                ros::this_node::getName().c_str());
      return -1;
    }

  if (vd.Disconnect())
    {
      ROS_FATAL("%s: failed to disconnect",
                ros::this_node::getName().c_str());
    }

  return 0;
}
```

Fig. 5 Vicon Code

Vicon to PR2 Code

```
#!/usr/bin/env python
import roslib;
```

```
roslib.load_manifest('vicon_hmd')

from vicon.msg import Values
import rospy
from math import *

import actionlib
from actionlib_msgs.msg import *
from pr2_controllers_msgs.msg import *
from geometry_msgs.msg import *

# Global Constants

# Robot height - should be gleaned from robot
HEIGHT = 1.36

# Filtering constant
ALPHA = 0.5

# Maximum motion in degrees per command period
MAX_DELTA = 10

def rad2deg(rad):
    return ((rad/pi)*180.0)

def deg2rad(deg):
    return ((deg/180.0)*pi)

def clip (x, clip):
    if (x > clip):
        return clip
    elif (x < -clip):
        return -clip
    else:
        return x

# Filtered version of angles returned by Vicon - global
variables
ax_f, ay_f, az_f = 0.0, 0.0, 0.0

def callback(data):
    global ax_f, ay_f, az_f

    # Get current values of angles and update filter
    ax_f = ALPHA*ax_f + (1-ALPHA)*(data.values[-6])
    ay_f = ALPHA*ay_f + (1-ALPHA)*(data.values[-5])
    az_f = ALPHA*az_f + (1-ALPHA)*(data.values[-4])
```

```
def listener():
    rospy.init_node('vicon_hmd_listener')
    rospy.Subscriber("/vicon/values", Values, callback)

    # Robots azimuth and elevation angles
    az, el = 0.0, 0.0

    client = actionlib.SimpleActionClient(
        '/head_traj_controller/point_head_action',
PointHeadAction)
    client.wait_for_server()

    g = PointHeadGoal()
    # g.target.header.frame_id = 'head_plate_frame'
    g.target.header.frame_id = 'base_link'
    g.min_duration = rospy.Duration(0.1)

    while not rospy.is_shutdown():
        # Main loop that sends commands to the robot

        # Come up with target azimuth and elevation
        delta_az = clip(az_f - az, deg2rad(MAX_DELTA))
        az = clip (az+delta_az, deg2rad(90))

        delta_el = clip(ax_f - el, deg2rad(MAX_DELTA))
        el = clip(el+delta_el, deg2rad(45))

        # Send the command to the PR2

        g.target.point.x = cos(el)*cos(az)
        g.target.point.y = cos(el)*sin(az)
        g.target.point.z = sin(el) + HEIGHT

        client.send_goal(g)
        client.wait_for_result()

        # Changing the sleep time changes the rate at which
commands are sent
        rospy.sleep (0.1)

if __name__ == '__main__':
    listener()
```

Fig. 6 Vicon to PR2

PR2 to HMD Code

```
#!/usr/bin/env python
import roslib; roslib.load_manifest('FullScreen')
import rospy
from sensor_msgs.msg import CompressedImage
import pygame

# The PyGame screen object
screen = None

# Screen reoslution
screen_size = (0,0)

# Flag to indicate when the user has requested we shutdown
running = True

def save_image(msg):
    """Save an image to disk. Return the file name."""
    if msg.format == "jpeg":
        tmp_name = "/tmp/pr2cam.jpeg"
    else:
        tmp_name = "/tmp/pr2cam.png"

    tmp_file = open(tmp_name,'wb')
    tmp_file.write(msg.data)
    tmp_file.close()
    return tmp_name

def show_image(msg):
    """Show an image fullscreen using PyGame."""
    global screen, screen_size, running

    # Save the image to a temporary file
    tmp_name = save_image(msg)

    # Load the temporary image into PyGame
    try:
        frame = pygame.image.load(tmp_name).convert()
        pygame.transform.scale(frame, screen_size, screen)
        pygame.display.update()
    except Exception as e:
        if running:
            raise e
```

```
def init_pygame():
    """Initialize PyGame and get screen resolution."""
    global screen, screen_size
    pygame.init()
    screen = pygame.display.set_mode(screen_size,
                                     pygame.HWSURFACE |
                                     pygame.DOUBLEBUF |
                                     pygame.FULLSCREEN)
    screen_size = screen.get_size()

def handle_events():
    """Return False when the user hits the escape key."""
    for event in pygame.event.get():
        if event.type == pygame.KEYDOWN and event.key ==
pygame.K_ESCAPE:
            return False
        elif event.type == pygame.QUIT:
            return False
    return True

if __name__ == '__main__':
    try:
        init_pygame()
        rospy.init_node('FullScreen')
        default_topic =
'/wide_stereo/right/image_rect_color/compressed'
        cam_topic = rospy.get_param('~cam', default_topic)
        rospy.Subscriber(cam_topic, CompressedImage, show_image)

        while handle_events() and not rospy.is_shutdown():
            rospy.sleep(0.5)

        running = False
        pygame.quit()

    except rospy.ROSInterruptException:
        pass
```

Fig. 7 Fullscreen HMD Code from PR2

Characterization and Design of Organic Field-Effect Transistor Circuits for Sensing Bioelectromagnetism

NSF Summer Undergraduate Fellowship in Sensor Technologies
Brian, Helfer (Electical Engineering) – University of Connecticut
Advisor: Cherie Kagan

ABSTRACT

Current scanning technology for the brain and heart requires electrodes to be placed on the surface, with a wire connected to each electrode. Because the electrodes are large, it is impossible to achieve a high sampling resolution of the signals from the tissue being scanned. Silicon based structures are not very suitable for this application. They have a rigid planar surface which prevents them from capturing a high degree of information from the three dimensional structure of the brain or the heart. However, an organic transistor, fabricated on flexible plastics, should be able to conform to and output a high degree of information from a three-dimensional structure. To test the ability of organic transistors to read data, an organic field-effect transistor was placed in a common source configuration. This configuration, when used with an organic transistor, allows the electrodes to conform to the structure, appear in higher density, and cover a larger area. A 50µm channel length transistor was able to operate with a low frequency gain of 0.97V/V and with a cutoff frequency of 91Hz. Organic field-effect transistors fabricated into circuits that are more complex were analyzed so that they could be considered for amplification purposes. A 6µm channel length inverter showed a low frequency gain of 3.2V/V and a cutoff frequency of 145Hz. A 10µm channel length cascode showed a low frequency gain of 2V/V with a cutoff frequency of 220Hz. These results suggest that organic field-effect transistors have the ability to measure and amplify a small signal and become an effective tool for mapping high-density signals of the brain and the heart.

Table of Contents

1. INTRODUCTION

Organic field-effect transistors (OFETs) are relatively new devices that have not yet been optimized and employed in a large variety of electronics. However, OFETs show great potential and could emerge as a dominant presence in electronic applications. OFETs, through low cost fabrication, have the potential to become an inexpensive source of electronics [1], [2]. OFETs can be mounted on plastic substrates providing a new area of functionality that current transistor technology does not possess. The new functionality in OFETs is largely due to the flexibility that this structure provides. The flexible plastic substrate employed allows for a sensor that uses flexible electrodes. These electrodes have potential to conform to and then more effectively map the electrical signals produced by an organ. They should also be able to apply voltages to stimulate nerves in that area.

One possible use of OFETs is to characterize disorders of the brain. The current approach to mapping the electric fields of the brain uses large electrodes in an array whose size is on the order of square millimeters with a wire connected to each electrode. The size of these electrodes along with the need to have a wire connected to each one prevents them from forming a high-density array of electrodes that can sample the signals with high spatial resolution. The OFET circuit should be capable of mapping brain signals more easily and safely than currently possible. The flexible electrodes would be able to conform to the shape of the brain, appear in higher density, and cover a larger area of the brain than possible with current electrodes. In order to realize this utility an OFET must be able to function in a circuit with low input reference noise to deal with small signals of approximately 30μV in amplitude and enough range to deal with large spikes up to 2mV in amplitude. This requirement is necessary because normal brain waves are on the microvolt scale while neural spikes are measured in millivolts. The circuit must have higher input impedance than the electrical tissue interface in order to prevent the signal from being compromised and it must block DC offsets in order to prevent saturation of the circuit [3].

2. BACKGROUND

2.1 Field-effect transistors

A field-effect transistor (FET) has terminals that are identified as the drain, the source, and the gate. The fabrication of an FET is accomplished by depositing layers of different materials. The first layer deposited is the gate. The gate controls the flow of electrons between the source and the drain. In an n-type FET, (positive) current enters through the drain and leaves through the source. In a p-type FET, (positive) current enters through the source and leaves through the drain. All FETs are made up of some basic components including a semiconductor layer, electrodes for the source and drain, a dielectric layer and a metal gate. These layers are fabricated onto a substrate as seen in Figure 1. An important characteristic of a transistor is its *mobility*. The mobility of a transistor is its ability to transport charge. This value is proportional to the current through the drain of the transistor. The drain current of a transistor is important because the transconductance of the transistor is proportional to the square root of the drain current while in saturation. The transconductance of a circuit controls the gain so a high transconductance is important for the creation of an amplifier circuit.

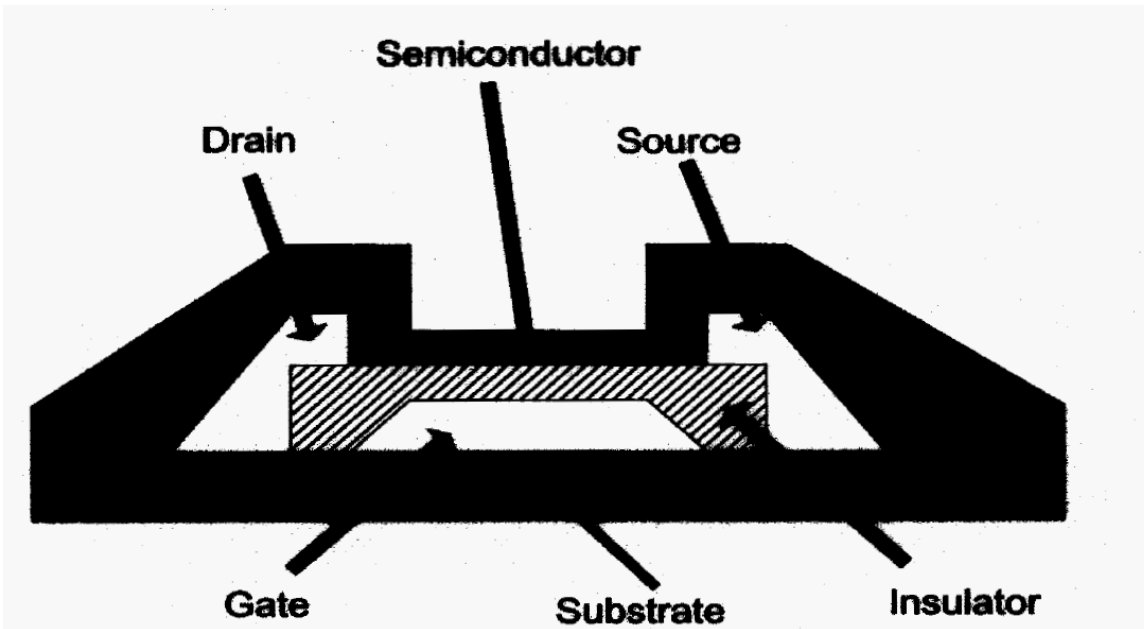

Figure 1: Transistor Diagram [4]

2.1.1 Organic field-effect transistors

Organic field-effect transistors differ from normal FETs in that they use an organic semiconductor. They also have the ability to be fabricated on plastic substrates, which imparts a characteristic flexibility that is not seen in other FETs.

In order for the OFETs to be placed in an intracranial circuit, they need to be both stable and non-harmful in the environmental conditions created within the skull. Kagan, Afzali, and Graham have demonstrated that reduced power and limited air exposure could create the necessary stability to integrate OFETs into electronic circuits [5].

2.2 Circuits for small signal amplification testing

Like other transistors, OFETs can be used for amplification. One type of OFET amplifier circuit is the common source. This configuration has the source connected to ground, with a resistor connected between a DC voltage and the drain, and a signal supplied to the gate. The output of this circuit is taken between the drain and the resistor. The gain of this circuit is controlled by the transconductance and the drain resistor. This makes it necessary to use large resistors when the transconductance is small. Another important characteristic of this circuit is its frequency response. The cutoff frequency for the circuit is inversely proportional to the product of the dominant capacitance and output resistance of the circuit.

Another circuit that can be used for amplification is the inverter. A diode inverter with a diode-connected load consists of two transistors with the source of the first connected to the drain of the second when one type of transistor is used. The first transistor has its drain connected to the gate, which causes it to act like a resistor. This allows this circuit to operate in a similar manner to the common-source configuration. The gain for this circuit is related to the ratio of the transconductance of the two transistors. Assuming the two transistors have similar mobility values this expression can be simplified to the ratio of the W/L values, as each transistor will have the same current flowing through it. An inverter outputs a large voltage for a small input voltage and outputs a small voltage for large input voltages.

An important circuit for measuring signals is the source-follower. Source-followers use two transistors similar to the inverter. However, unlike the inverter, the source-follower has the gate of the second transistor connected to its source. This configuration functions like a unity-gain buffer. It provides a gain of approximately 1V/V while converting high impedance to low impedance. This allows readings to be taken without changing the output resistance of the circuit.

A cascode is a more complex circuit used for the amplification of signals. The cascode used consists of three transistors. The first transistor has its drain connected to the gate and functions as a resistor. The second transistor has its drain connected to the source of the previous transistor. The output of the circuit is taken at this point. The gate of the second transistor is supplied a bias voltage and its source is connected to the next transistor. The final transistor has its drain connected to the source of the previous transistor and receives an input signal at the gate. The source of this transistor is connected to ground. An important characteristic of the cascode is its increased frequency response. This is due to its elimination of the Miller effect, which means that the capacitance between the input and the output is not increased.

A ring oscillator is a circuit that consists of an odd number of inverters connected without the input of an inverter coming from the output of the previous inverter. If the output from the previous stage was a high voltage, the next inverter will convert it to a low voltage and if the output of the previous inverter was a high voltage, the next inverter will switch it to a low voltage. This characteristic causes the output of the ring oscillator to look like a sine wave.

2.2.1 Noise in Circuit Design

Noise is a substantial issue when dealing with circuits that receive small input signals. If noise is not properly filtered, it causes distortion and prevents an accurate measurement of the signal being read. One source of noise is the 60 Hz AC noise found in the United States and 50 Hz found in other countries. In order to filter this noise a notch filter is often used. A notch filter allows all the components of a signal to pass except for those falling in a specific frequency range. In the case where only the data from a specific frequency range is relevant, high-pass and low-pass filters can be added to further filter out noise. A high-pass filter allows signals at high frequencies to continue through the circuit, while signals at frequencies below the chosen cutoff frequency are reduced. A low-pass filter works based on the same concept as a high-pass filter but it attenuates high frequencies above the cutoff frequency and allows low frequency signals to pass through the circuit.

2.3 Neurological Signal Sensing

2.3.1 Electroencephalography (EEG)

Electroencephalography, also known as EEG, is defined by C. E. M. van Beijsterveldt and D. I. Boomsma to be “a recording, from the scalp, of the electrical activity of the brain over a short period of time”[6]. Typical brain waves studied by an EEG occur within the range of less than 1 Hz to 100 Hz. The brain signals are divided according to the frequencies they occur at and then classified as alpha waves, beta waves, gamma waves, delta waves, or theta waves. Waves occurring between 8 and 13 Hz are considered alpha waves. Alpha waves are responsible for taking in and amplifying information sent to the brain. Waves occurring between 12 and 30 Hz are considered beta waves. Continuing in this pattern, gamma waves have a frequency between 30 and 100 Hz, delta waves have a frequency up to 4 Hz and theta waves have a frequency between 4 and 7 Hz. An EEG can be used to detect an abnormality within the brain by displaying the brain signals. This information allows for the successful diagnosis of brain disorders.

2.3.2. Electrocorticography (ECoG)

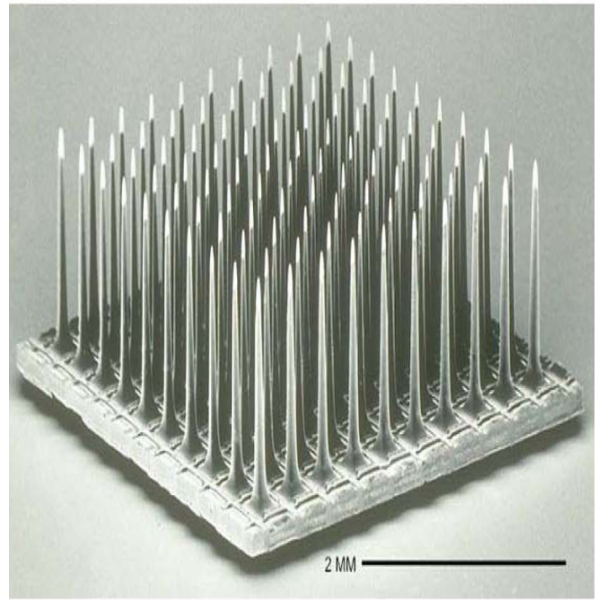

Figure 2: Utah Electrode Array [3]

Electrocorticography is similar to electroencephalography in that it is used to measure brain signals; however, in place of measurements being taken from the skull, they are taken intracranially. Electrocorticography is used to determine a specific area of the brain where an abnormal signal originates before surgery is performed. This can be done on seizure patients before the abnormal tissue is removed. Electrocorticography can also be used to provide a stimulus to an area of the brain. The current approach for an ECoG is to use a device called the Utah Electrode Array as seen in Figure 2. The Utah electrode array consists of a 10 x 10 array of platinum tipped silicon electrodes with 4 x 4 x 1.5 mm^3 dimensions [3]. These dimensions limit the density of the signal and the amount of brain surface area that can be covered.

2.4 Electrocardiography (ECG)

Electrocardiography is an important tool for studying heart arrhythmias and disorders. An electrocardiogram is performed by placing electrodes on the chest. It is used to measure the electrical activity of the heart over time. An electrocardiogram should have a bandwidth of 100 Hz and be able to measure signals as small as 20μV [7]. The signal must also show little error to ensure that there is no cause for misdiagnosis. The signal from an ECG consists of a P wave, a QRS complex and a T wave. The P wave is the result of the depolarization, which occurs from the sinoatrial node to the atrioventricular node. The QRS complex corresponds to the depolarization of the right and left ventricles. The T wave represents the repolarization of the ventricles.

3. MATERIALS AND METHODS

3.1 Organic Device Characterization

All measurements of organic transistors and organic transistor circuits were performed with devices kept in a controlled nitrogen environment. The transistors used throughout the experiments use pentacene as the organic semiconductor with each transistor being fabricated on a Kapton substrate. Throughout the experiments, measurements were taken with a Keithley 2420 source meter, an Agilent E3620A voltage supply, an Agilent 4156C parameter analyzer, an Agilent 3320A function generator, and a Tektronix TDS2014B oscilloscope.

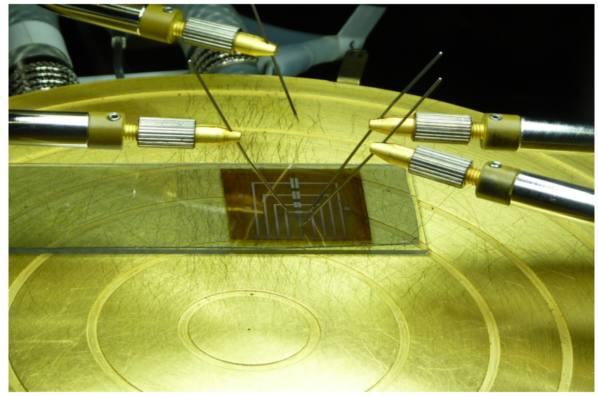

Figure 3:Probe Connections from within the glove box

In order to connect the circuit to our electrical supplies as well as other circuit components, we made connections directly in the glove box using probe tips as seen in Figure 3. These probe tips were connected to BNC connector cables through a feed-through, which allowed the stages of the circuit to be connected.

When working with the basic organic transistors we began by measuring the drain current against the voltage between the drain and the source. We measured this curve for varying values of the gate voltage as seen in Figure 4. These gate values ranged between -50V and 0V and increased with a step size of 10V. This graph shows the voltage necessary for the transistor to be operating in the saturation region where it will have consistent current levels. It was necessary to push the transistor into the saturation region so that it would have consistent gain throughout the experiments. The drain current was also measured against the voltage between the gate and the source as seen in Figure 4. This was done for a voltage of -50V between the drain and the source. From this data, we extracted the transconductance of the transistor, which was taken as the slope of the linear portion of the graph. These characteristics were run at the beginning and end of every experiment to monitor the stability of the organic transistors.

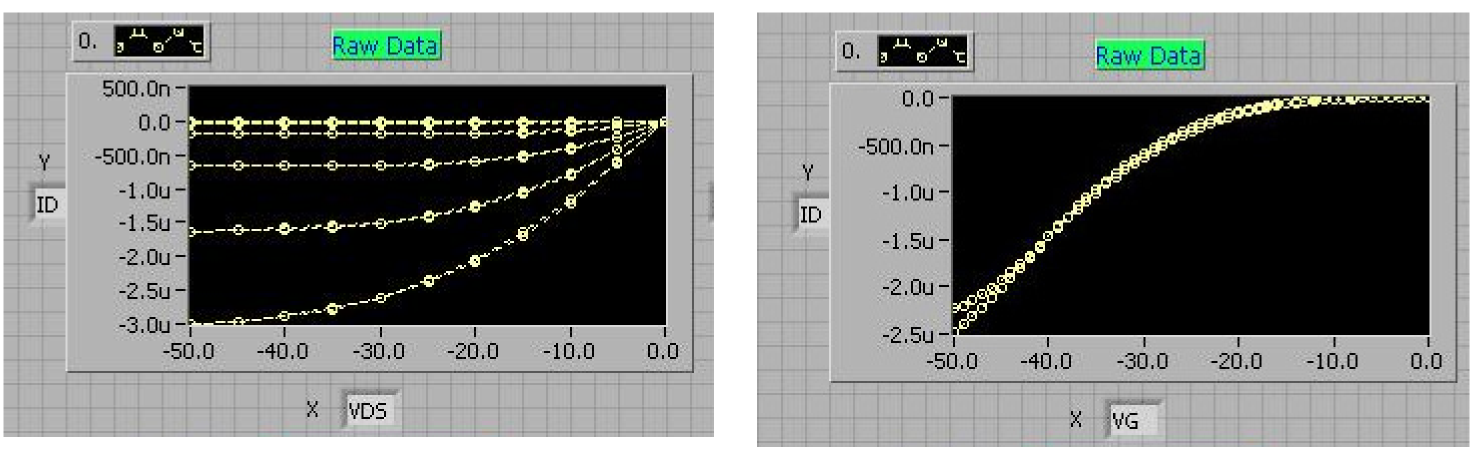

Figure 4:50um DC Characteristics: W/L = 750um/50um

3.2 Cardiac and Neurological Sensor Design

With this data taken, the organic transistor could be connected to other electrical components. A multi-staged circuit was designed in order to read and output biological signals. The first stage of the circuit utilized a 50µm channel length organic transistor in a common source configuration. For this configuration, a resistor of value 10MΩ was connected between the drain of the transistor and a voltage source, V_{DD}. The source of the transistor was connected to another voltage source to help create a voltage difference between drain and source that would allow the transistor to operate in the saturation region. The signal was simulated by a function generator, that was connected to the gate of the transistor.

The output of this stage was taken between the drain and the resistor. This output was then connected to an op amp configured as a unity gain buffer. Throughout the experiments, only op amps with impedance greater than 10^{12} were used. The unity gain buffer consisted of the output from the last stage going into the non-inverting end of an op amp while the inverting end was connected directly to the output. This stage reduced the impedance before the next stage of the circuit, which utilized an inverting op amp. The final stage of the circuit connected the output of the unity gain buffer to a resistor, which was connected to the inverting end of another op amp. The inverting end of the op amp was then connected to the output through a resistor. The non-inverting end of this op amp was connected directly to ground. The full circuit can be seen in Figure 5.

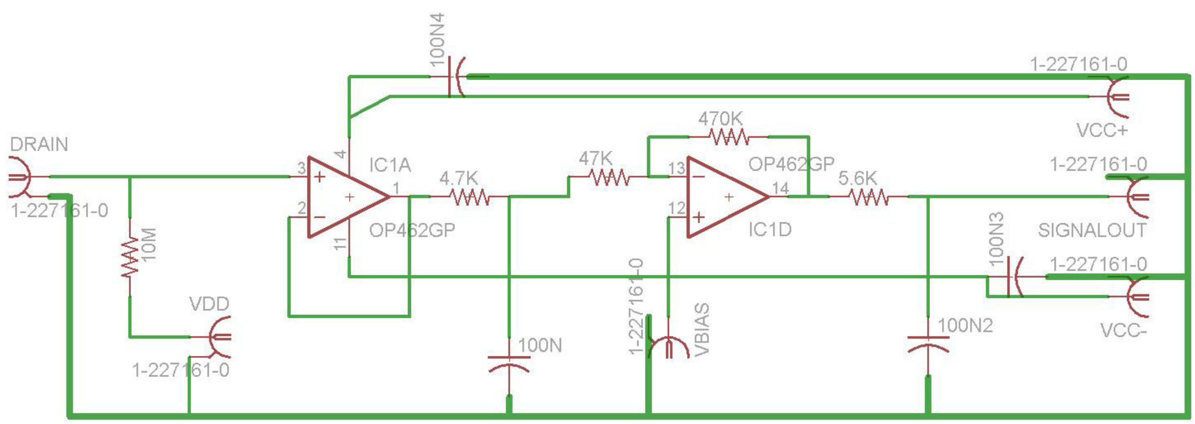

Figure 5: Circuit Schematic

This circuit to analyze biological signals was first tested using a breadboard. The organic transistor was maintained in the nitrogen environment while the electrical equipment, breadboard, resistors, and op amps were left outside in an ambient air environment. The drain, source, and gate of the organic transistor were connected to the electrical devices outside of the glove box using BNC cables connected to the feed-through of the glove box. The drain and the source of the transistor were connected to voltage supplies while the gate was directly connected to a function generator. The function generator was setup to create a sine wave at different frequencies and amplitudes. The op amp supply-voltages were provided by the parameter analyzer that was setup to generate a constant DC voltage. The output of the circuit was taken from the output of the op amp in the third stage using a digital oscilloscope.

After testing the completed circuit, low-pass filters were added after the unity gain buffer and after the inverting amplifier. The low-pass filter used was designed as a series combination of a resistor and a capacitor with the output taken between the capacitor and ground. The values of the resistor and capacitor were chosen so that the cutoff frequency created by the filter would be higher than the cutoff frequency of the first stage common source circuit. The capacitors used both had a value of 100nF. The resistor used for the first low-pass filter had a value 4.7kΩ, which corresponds to a cutoff frequency at 339Hz. The resistor used for the second low-pass filter had a value of 5.6kΩ, which corresponds to a cutoff frequency at 284Hz.

After analyzing the circuit on the breadboard, a printed circuit board (PCB) was fabricated in an attempt to reduce the effects of noise on the circuit. The design of the PCB was accomplished using the software Eagle. The PCB design used 90º BNC connectors for all of the inputs and outputs. The schematic of the board the board was made identical to the circuit on the breadboard and the board layout was designed with the goal of minimizing space. After designing the board layout, the file was sent to 4PCB.com for fabrication. The completed board layout along with the fabricated PCB can be seen in Figure 6.

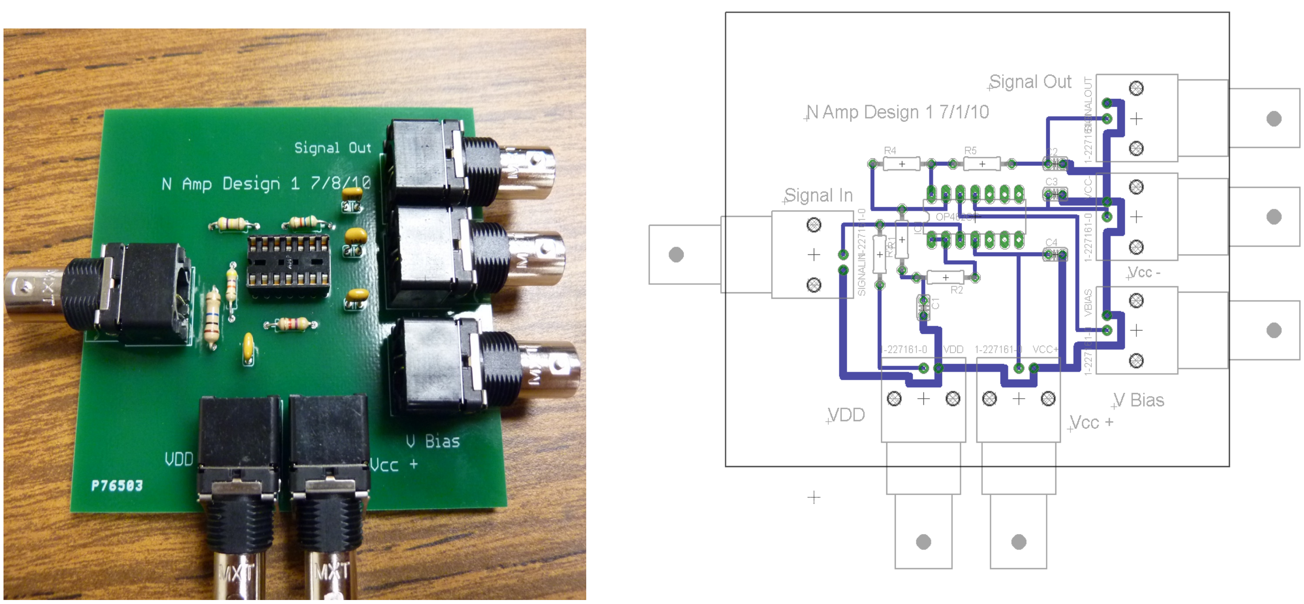

Figure 6: Board layout and fabricated PCB

The PCB was tested, like the breadboard, by connecting the voltage sources to the circuit and reading the output from the digital oscilloscope. The peak-to-peak output voltage was taken for sine waves created from the output of the circuit. The input sine wave was varied by amplitude and by frequency. This output voltage was graphed as a function of frequency to measure the trend in gain and the cutoff frequency for this circuit configuration. It was then found that a BNC cable connected to the output with AC coupling severely reduced the gain. Readings were then retaken with the oscilloscope set to DC coupling.

The PCB was also tested from within the glove box. For these measurements, the probe cable for the drain was connected directly to the PCB. The source and gate probe cables as well as BNC cables for V_{CC}+, V_{CC}-, V_{Bias}, V_{DD}, and the output were connected to the feed-through of the glove box

3.3 Organic Transistor Circuit Analysis

Completed organic circuits fabricated on a plastic substrate were also analyzed. These fabricated circuits were treated with thiophenol to lower their contact resistance. The circuits included single transistors, inverters, source followers, cascodes and ring oscillators. The circuits were kept in a nitrogen environment glove box and connections were made with probe tips.

3.3.1 Single Transistor Analysis

The single transistors treated for contact resistance were analyzed in a similar manner to the previous set of transistors. A DC scan was first run to measure the drain current against the voltage between the drain and the source. The drain current was then measured against the voltage between the gate and the source. After this was done, the single transistors were connected to the PCB. This used the single transistors in a common source configuration and sent the output to the unity gain buffer, followed by a low-pass filter, an inverting amplifier, and another low-pass filter.

3.3.2 Inverter Analysis

A series of inverters were also analyzed. The inverters each had a different channel length. The channel lengths tested included 2μm, 4μm, 6μm, 8μm, 10μm and 30μm. Figure 7 shows the glove box probe tips connected to the 6μm channel-length inverter.

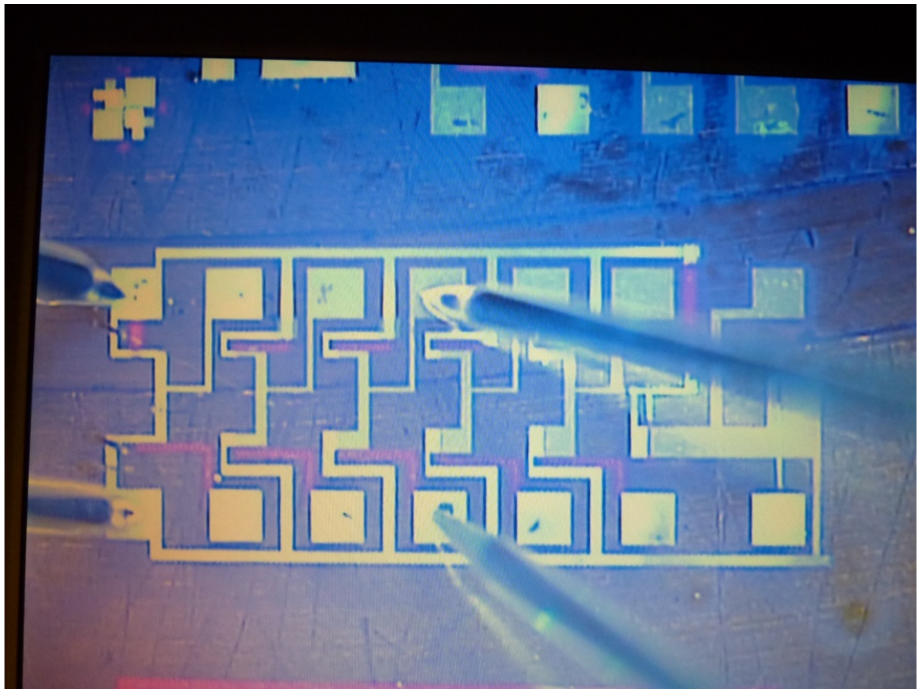

Figure 7:Inverter probe connections

The top left probe supplies a voltage, V_{DD} to the drain of the inverter. The bottom left probe is connected to the ground for the inverter circuit. The bottom right probe supplies the input signal for the inverter while the top right probe is used to measure the output of the inverter. The inverter was tested using the parameter analyzer. The parameter analyzer was setup to supply a constant V_{DD} value and to provide a common ground for the circuit. This inverter was analyzed for both a V_{DD} of -80V and -100V. The input signal was varied from 0V to -100V with a step size of -1V and the output voltage was taken at each point.

AC analysis was then completed on the inverters. For the AC analysis, V_{DD} and V_S were both connected to voltage sources. The sources were used to supply a voltage between the drain and the source that would cause the transistor to operate in the saturation region. V_S was chosen to provide the necessary offset to the input signal and then V_{DD} was selected as the value to create the necessary V_{DS} value. V_S was chosen as a value that would offset the input signal allowing the circuit to be biased in the linear region where the gain would be the highest. After selecting an experimental value, the values for V_{DD} and V_S were adjusted through testing different values and monitoring the gain. The optimal value for V_{DD} was found to be -84V while the optimal value for V_S was found to be 16V. The input was connected to a function generator through a BNC cable and the output was connected to a PCB with a unity gain buffer through another BNC cable. To reduce the effect of noise a 1V peak-to-peak input signal was used. The output was read from a digital oscilloscope with the oscilloscope probe set to 10x attenuation. The connections from the inverter to the PCB were all made inside the nitrogen environment glove box.

3.3.3 Source Follower Analysis

DC analysis was run for the source follower. For this analysis, five probes were used. Two probes were connected with a T-connector and then connected to a feed-through. These both provided the same value, V_S. The remaining three probes were each connected to an individual feed-through. The four feed-through were connected to the parameter analyzer. V_S was set to a common ground. V_{DD} was set to a constant voltage. For our experiments we used V_{DD} at -60V, -80V, and -100V. V_{In} was setup to vary between 0V and -100V with a step of -1V. The fourth channel was used to measure the output from the source follower.

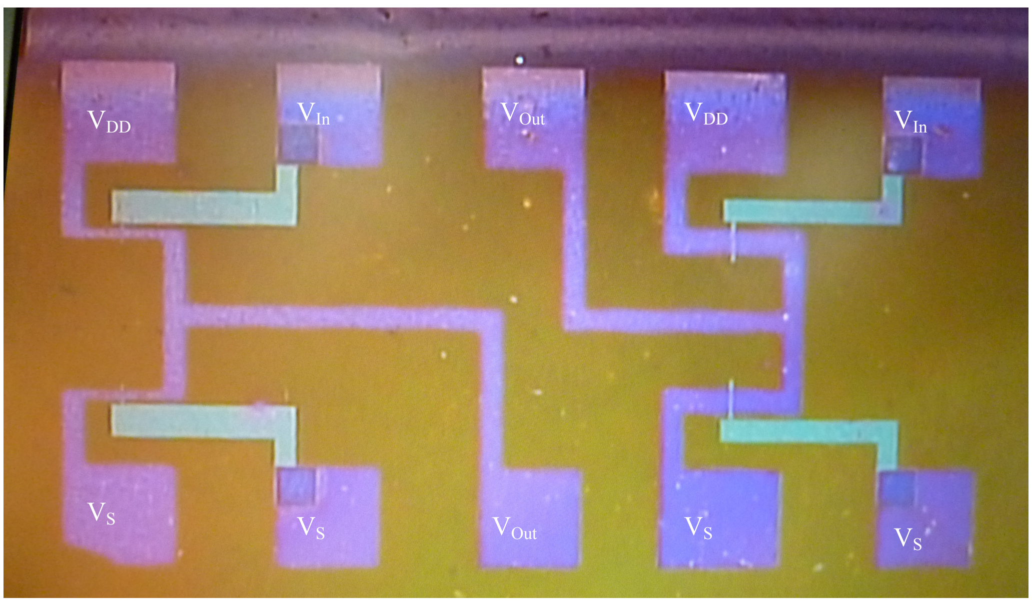

Figure 8:Fabricated source-follower

3.3.4 Cascode Analysis

In order to test the cascode, five different probes were needed to make connections to the pads. In order to run DC analysis the probes connected to V_{Out}, V_{DD}, V_{In}, and V_S were connected to the parameter analyzer. The probe connected to V_{Bias} was connected to a voltage source. A scan was setup using the parameter analyzer with a constant voltage supplied to V_{DD}. For our analysis, we used a V_{DD} of -100V. The input voltage, V_{In}, was varied from 0V to -100V in a step of -1V. V_{Bias} was set to different values for each scan with a voltage source. V_{Bias} was tested at -30V, -40V, -50V and -60V.

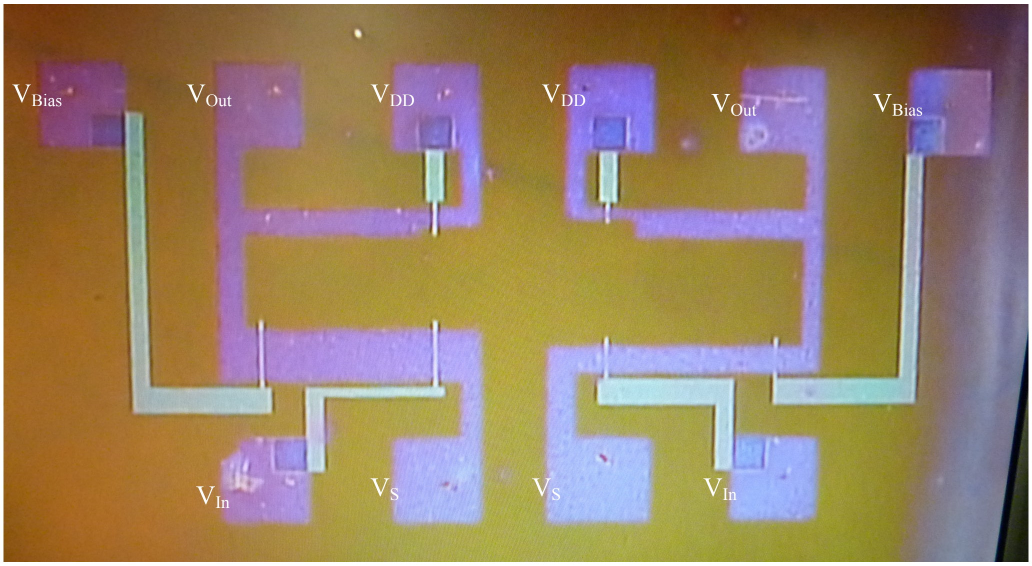

Figure 9:Fabricated cascode

AC measurements of the cascode were then taken. For the AC analysis V_{DD} and V_S were each connected to a voltage source. The voltage between the drain and the source was chosen to allow the transistors to operate in the saturation region and the source voltage was chosen to offset the input signal into the linear region of the circuit. V_{DD} was set to -83V and V_S was set to 17.18V throughout the experiment. V_{Bias} was chosen as -50V after examining the DC characteristics of the circuit. A 1V peak-to-peak input was supplied by the function generator and the output was connected to a PCB containing a unity-gain buffer. The output was measured by a digital oscilloscope using a probe set to 10x attenuation directly connected to the output of the unity gain buffer.

3.3.5 Ring Oscillator Analysis

A ring oscillator consisting of five inverters was tested. For these tests a voltage of -100V was supplied as V_{DD} to all the inverters and the ground was kept as 0V. The output was connected to a unity gain buffer that was fabricated onto a PCB and the signal was read using a digital oscilloscope. Figure 10 shows the structure of the ring oscillator. The triggering transistor was bypassed for the measurements that were taken.

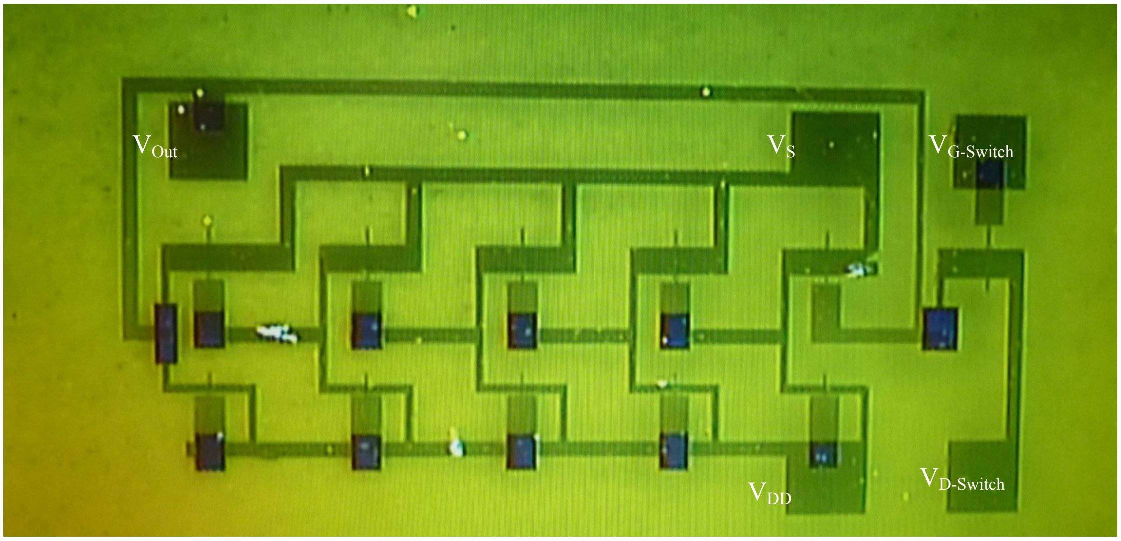

Figure 10:Fabricated ring oscillator

4. RESULTS

4.1 Neural and Cardiac Circuit

The third stage of the circuit was isolated and tested by using a function generator to provide an input to the unity gain buffer and bypass the common source stage. The amplifier has shown a gain of approximately 8.8V/V. The third stage also has a cutoff frequency of 180Hz. This differs from the expected cutoff frequency of 300Hz. This is likely a result of the two low-pass filter poles around 300Hz. These poles run together and cause the cutoff frequency to be much lower than expected.

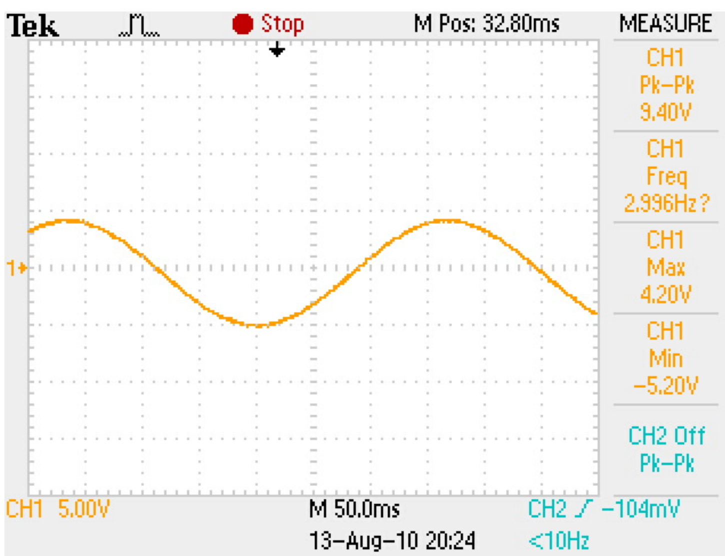

Figure 11: Output signal taken from 3rd stage of circuit; the transistor had a W/L= 750um/50um

Figure 11 shows the output of the third stage of the circuit connected outside of the glove box with an input signal of 1V peak-to-peak at a frequency of 3Hz. This corresponds to a gain of approximately 9.4V/V. This gain is produced by the amplifier stage multiplied by the common-source stage.

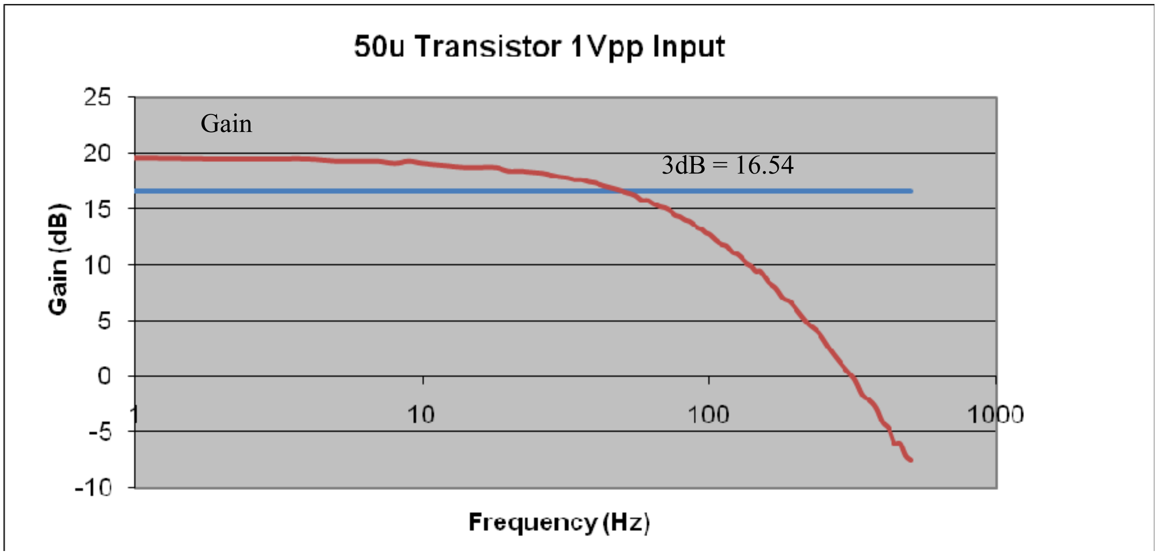

Figure 12:50µm common-source configuration outside glove box

Figure 12 shows the gain from the third stage of the PCB plotted against frequency with a 1V peak-to-peak input signal. At low frequencies the circuit shows a gain between 9.5V/V and 9V/V. However, the circuit reaches its cutoff frequency by 52Hz. This is a result of the extra capacitance supplied to the output by the BNC cables.

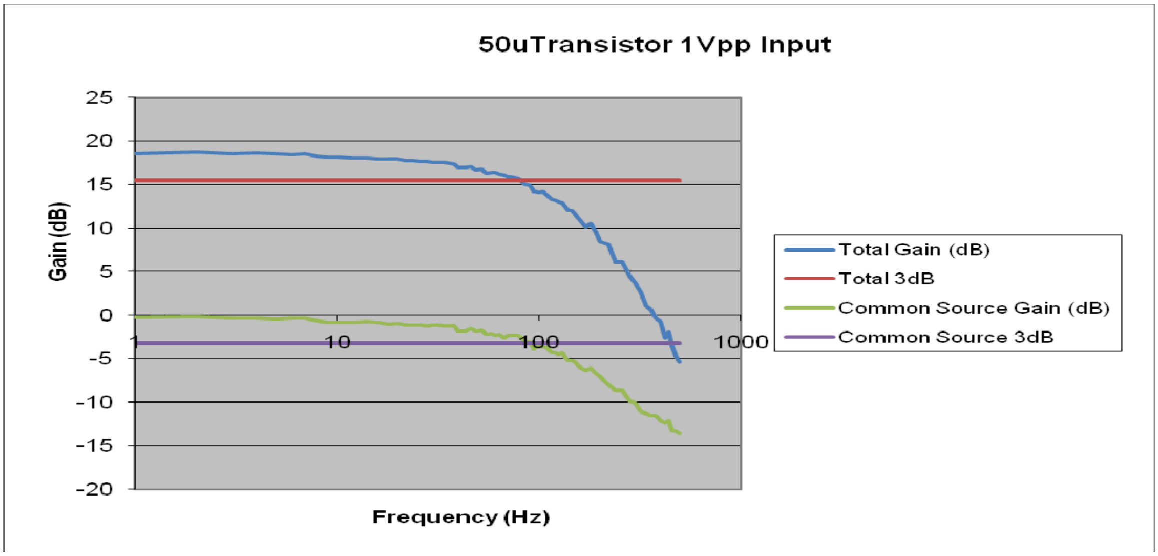

Figure 13:50µm common-source configuration inside glove box

Figure 13 shows a plot of gain versus frequency for the same transistor with all connections made inside the glove box. This allowed shorter BNC cables to be used. For this setup the output from the final stage of the PCB and the output directly after the unity gain buffer were both read. At low frequencies, the unity gain buffer shows that the common-source configuration is creating a gain between 0.9V/V and 0.984V/V. The final output from the PCB is showing a gain between 7.92V/V and 8.64V/V. This gain matches the theoretical gain of the common-source stage multiplied by the amplifier's gain of 8.88V/V. The common source stage shows a cutoff frequency of approximately 91Hz while the total circuit has a cutoff frequency of approximately 82Hz. By connecting the PCB within the glove box, the cutoff frequency was increased from 52Hz to 82Hz. This indicates that the long BNC cables used to make connections outside of the glove box provided the dominant output capacitance. By changing the length of the cables used it was possible to increase the frequency response. The lower cutoff frequency of the total circuit can be explained by the closeness of the poles lowering the overall cutoff frequency.

4.2 Organic Transistor Circuit Analysis

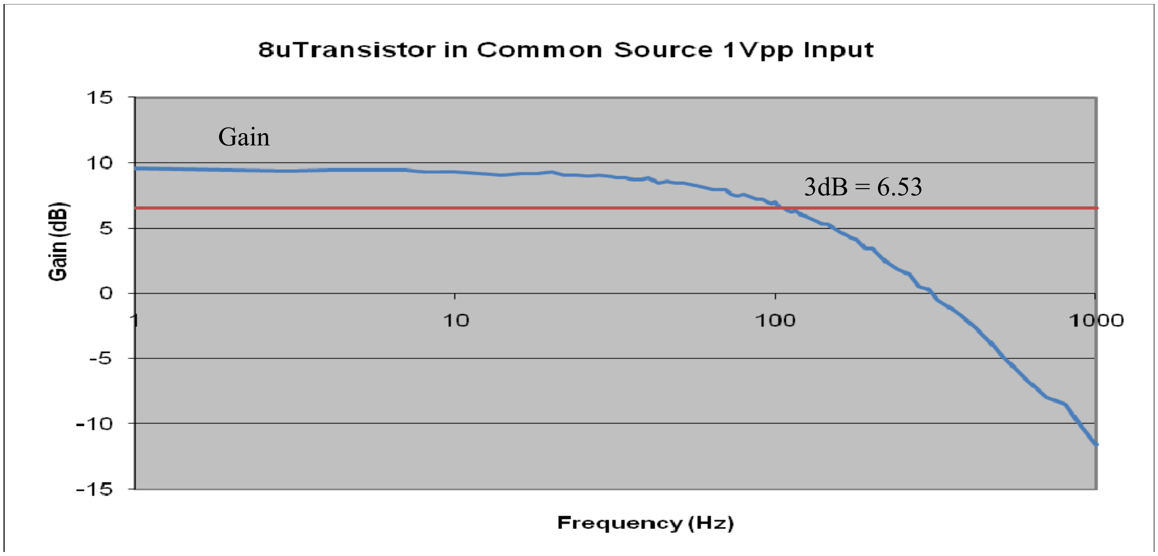

Figure 14:8μm common-source configuration inside glove box

Figure 14 shows the gain of the 8μm single transistor configured in a common-source configuration. This value is taken after the unity-gain buffer and before any additional filtering or amplification is done. At low frequencies, this configuration shows a gain between 2.92V/V and 3V/V. The cutoff frequency for this stage appears at 106Hz.

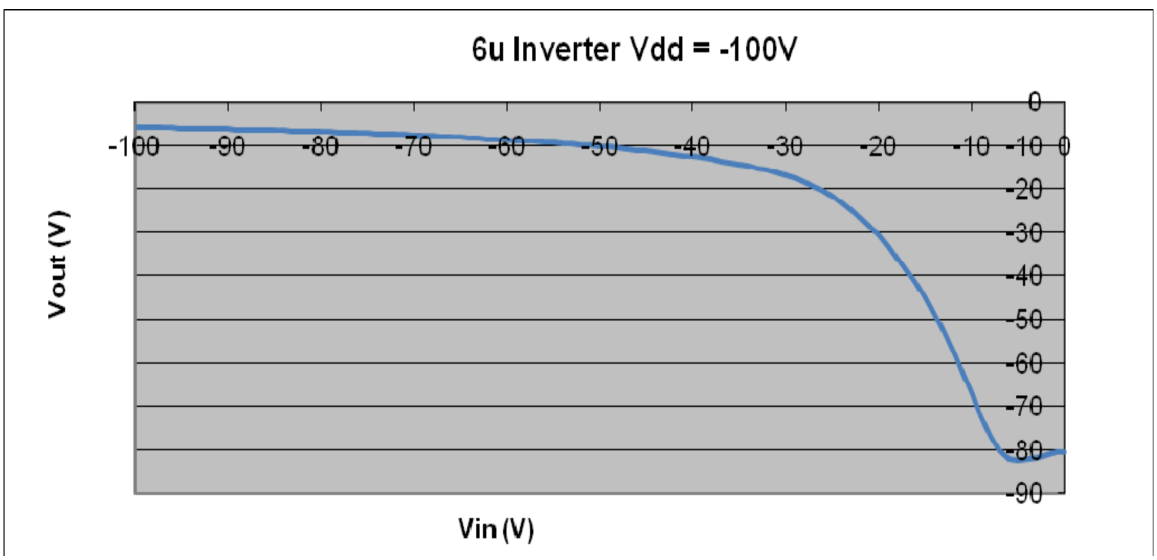

Figure 15: DC response of 6μm inverter

The magnitude of the ideal gain for this inverter is 3V/V. This value was approximated using the W/L values for the transistors involved in the circuit. The inverter is showing an actual gain of 3.2V/V when biased in the linear region. This was found by taking the slope of the linear region.

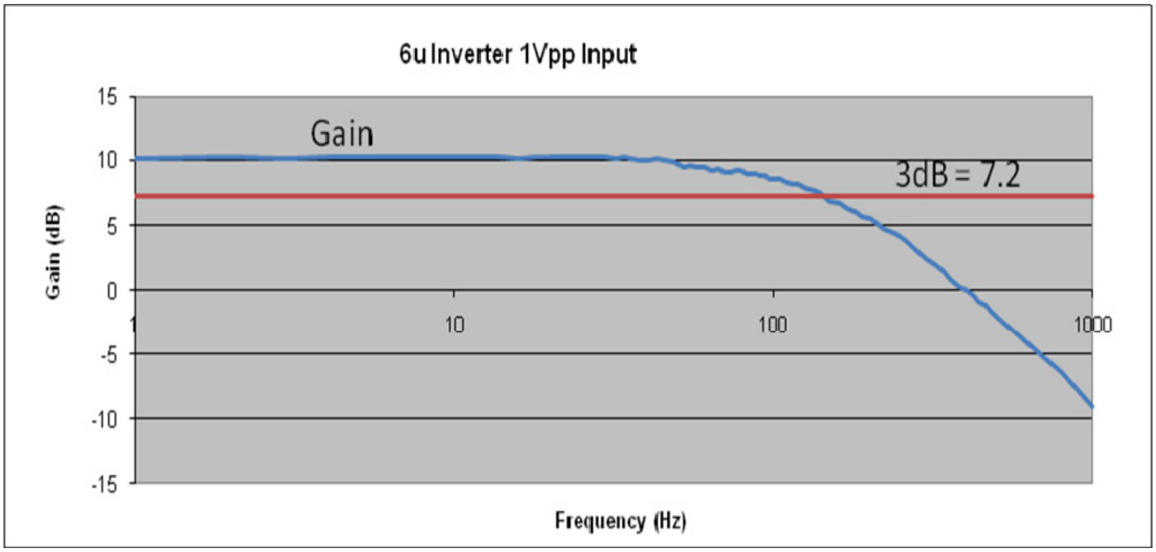

Figure 16: AC response of 6µm inverter

Figure 16 shows the gain for the 6µm channel length inverter plotted against the frequency of the input signal. At low frequencies, the inverter shows a gain of 3.2 V/V. The cutoff frequency for this circuit is approximately 145Hz.

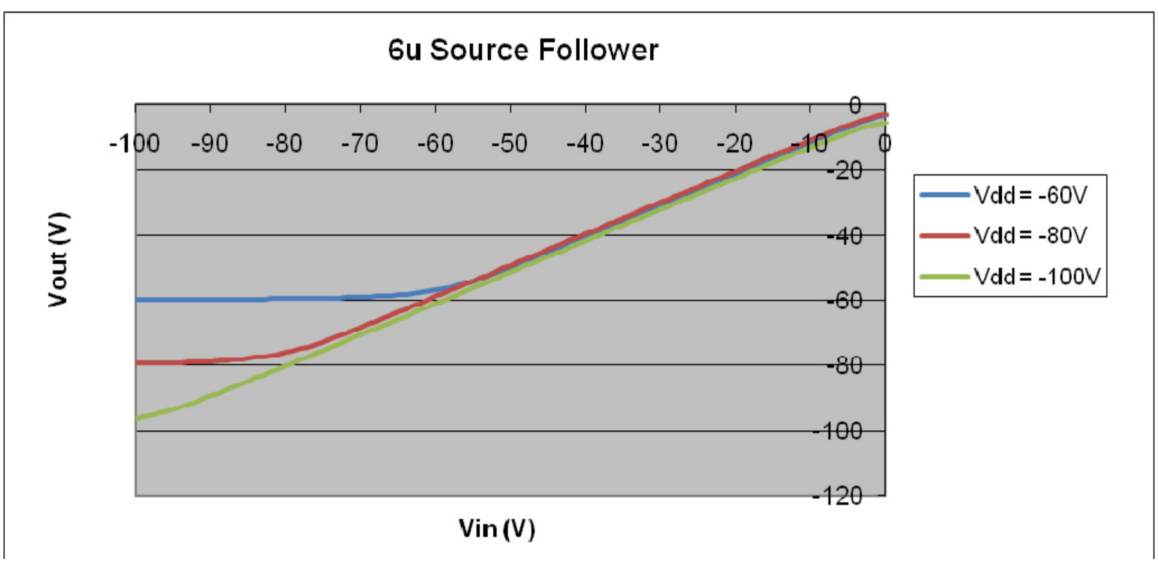

Figure 17: DC Characteristics of 6µm source follower

The source-follower circuit configuration has an ideal gain of one. The fabricated devices showed an average gain of 0.94V/V in the linear region. As the V_{DD} used in the source-follower is increased, the linear region of operation is also increased.

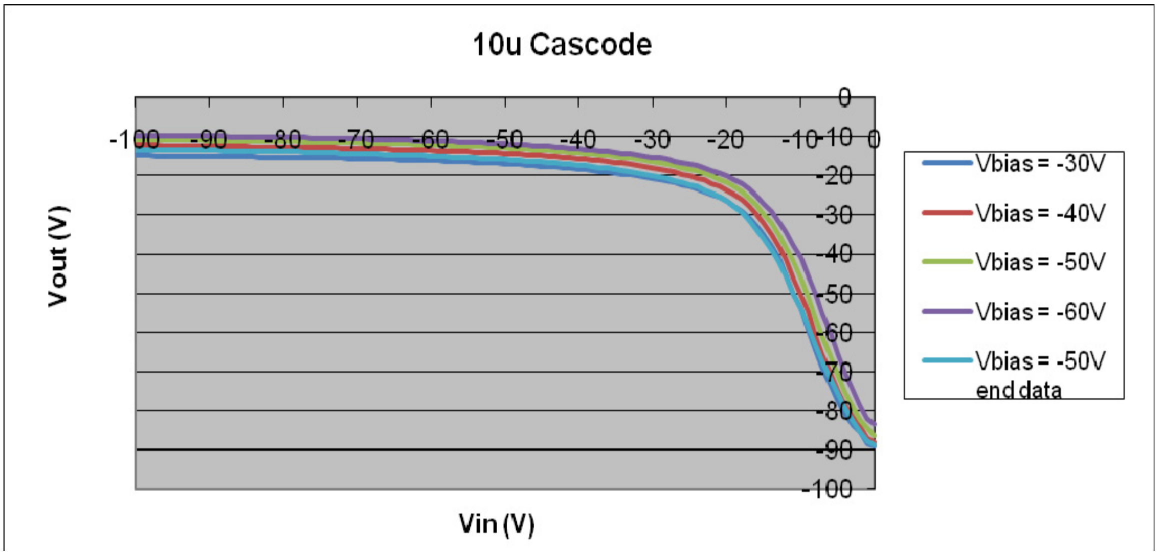

Figure 18: DC Characteristics of 10µ cascode

The cascode was analyzed for an input signal that varied between 0 V and -100 V. The output was tested with the bias set to -30V, -40V, -50V and -60V. The cascode showed a gain in the linear region of approximately 2V/V.

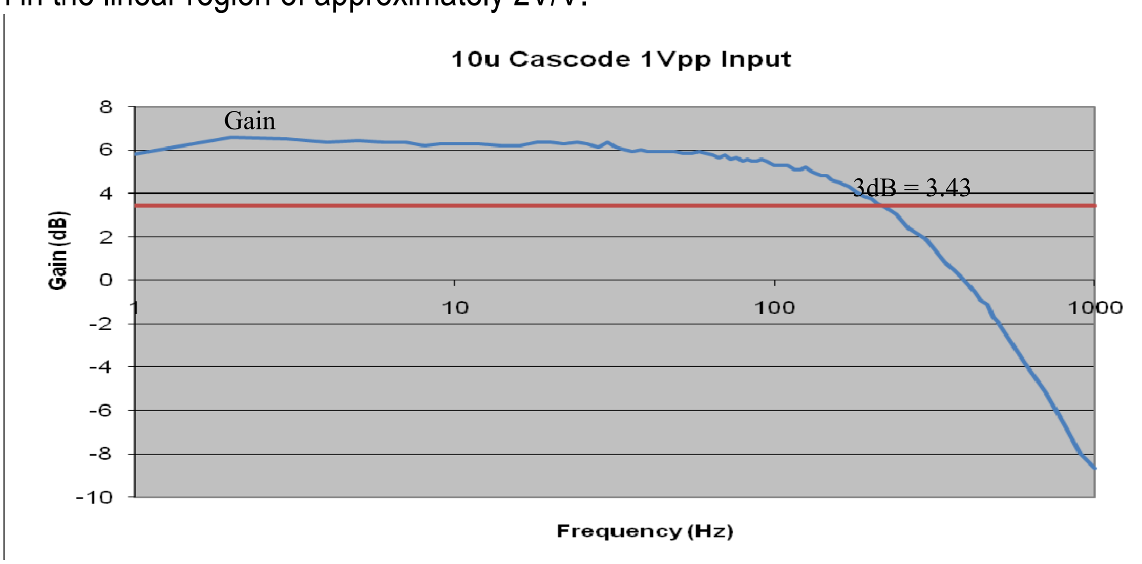

Figure 19: AC response of 10µ cascode

Figure 19 shows the AC response of the cascode with the 10µm channel length load. At low frequencies the cascode has a gain between 2V/V and 2.14V/V. The cascode shows a cutoff frequency at aprroximately 220Hz.

Figure 20: Output from ring oscillator

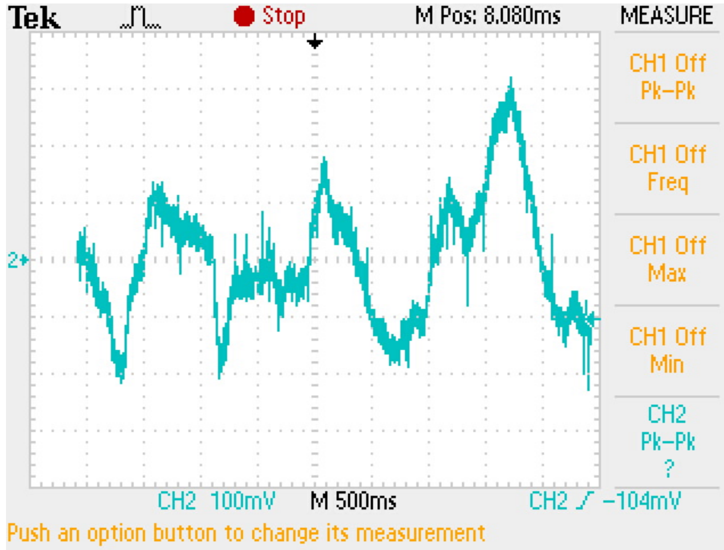

Figure 20 shows the output of the ring oscillator. This circuit is producing oscillations; however, the wave is inconsistent and varies in amplitude and shape.

5. DISCUSSION

In this study, we were able to employ OFETs as amplifiers through fabrication and circuit techniques. The circuit-configurations used were designed to test if OFETs could be used to read and amplify a small signal without heavily compromising the circuit bandwidth. The three-stage circuit designed with a 50µm channel-length transistor in a common-source configuration shows a low-frequency voltage gain of approximately 8V/V. With all connections made outside of the glove box, the final stage shows a bandwidth of approximately 52Hz. When connections are made within the glove box the final stage shows a bandwidth of 82Hz. This improvement in bandwidth is due to the lower output capacitance made possible by the shorter BNC cables used to make connections from within the glove box. The common-source stage alone shows a gain of approximately 0.95V/V. The common-source stage has a bandwidth of 67Hz when connections are made outside of the glove box and a bandwidth of 91Hz when connections are made within the glove box. The fact that the bandwidth is higher in the first stage than the total circuit indicates that the poles created in the later stages could be decreasing the frequency response. Through use of the common-source stage and the unity-gain buffer alone, there should be sufficient bandwidth for the analysis of the local field potentials of the brain and the electrical signals passed through the heart.

The more complex transistor circuits also show promise for the amplification of signals from the brain. The 8μm channel-length transistor, inverter, and cascode all show a higher gain than the 50μm channel-length transistor. Because of the elimination of the Miller effect, the cascode is also able to produce a greater bandwidth than possible with the single transistors or the inverters. The ring oscillator still does not show a consistent sine wave. This is likely due to the lack of uniformity between the inverters in the ring oscillator and insufficient time to invert the signal from the previous stage.

The use of a PCB was important for the reliability of the data. When data was taken from the circuit-configuration built on a breadboard there was a high degree of noise. This noise makes it impossible to distinguish the true peak-to-peak voltage of the output signal and prevents the accurate analysis of the gain and cutoff frequency. This noise was caused by the nature of the breadboard. In order to make connections on a breadboard wires needed to be employed. These wires become an issue because they can act as antennas and pick-up the noise generated by the components and the surrounding electronics. If this noise were left unfiltered, the output signal generated would be too unreliable to make any diagnostic decisions. By using a PCB, all wires were eliminated and the amount of noise was greatly reduced.

6. RECOMMENDATIONS

The first thing that needs to be done is to ensure that the OFET circuits can accurately output brain signals. In order to do this an electrode should be inserted into the brain and connected to the circuit through a wire. The output from the circuit should be connected to a unity gain buffer and be measured so that it can be compared to an output that is taken directly from an electrode. This test should be done with the common-source, inverter, and cascode being used for amplification. If the source-follower shows that it can function properly as a unity-gain buffer then it should be possible to fabricate a complete circuit for reading signals from the brain and heart without additional components needed.

For neurological and cardiac applications of OFETs, the next step is to ensure that the materials used are safe and non-toxic while interacting with living tissue. The circuit would also become safer if the dielectric were to be scaled so that the transistor can operate at lower voltages. Once these two precautions are covered, an OFET with electrodes that come in direct contact with the brain should be tested.

The next step after improving the ability of OFETs to sense signals of the brain and heart would be to be able to generate a stimulus under certain pre-defined conditions. This could create a circuit that more easily conforms to tissue and serves diverse roles including being used as a pacemaker for the heart.

7. ACKNOWLEDGMENTS

I would like to thank Dr. Cherie Kagan and Dr. Jan Van der Spiegel for their knowledge and insight, which has been a major factor in my progress throughout the summer. I would also like to thank Shang Wei, Yuming Lai, and Sangam Saudari for the many hours they spent working with me. I would also like to thank the National Science Foundation for the funding that has allowed me to participate in the SUNFEST program.

8. REFERENCES

[1] D. Knipp, R. A. Street, A. Völkel and J. Ho, "Pentacene thin film transistors on inorganic dielectrics: Morphology, structural properties, and electronic transport," *J. Appl. Phys.,* vol. 93, pp. 347, 2003.

[2] J. T. Mabeck and G. G. Malliaras, "Chemical and biological sensors based on organic thin-film transistors," *Analytical and Bioanalytical Chemistry,* vol. 384, pp. 343-353, 2006.

[3] R. R. Harrison, "The design of integrated circuits to observe brain activity," *Proc IEEE,* vol. 96, pp. 1203-1216, 2008.

[4] D. M. Binkley, N. Verma, R. L. Crawford, E. Brandon and T. N. Jackson, "Design of an auto-zeroed, differential, organic thin-film field-effect transistor amplifier for sensor applications," in *Society of Photo-Optical Instrumentation Engineers (SPIE) Conference Series,* 2004, pp. 41-52.

[5] C. R. Kagan, A. Afzali and T. O. Graham, "Operational and environmental stability of pentacene thin-film transistors," *Appl. Phys. Lett.,* vol. 86, pp. 193505, 2005.

[6] C. E. M. Beijsterveldt and D. I. Boomsma, "Genetics of the human electroencephalogram (EEG) and event-related brain potentials (ERPs): a review," *Hum. Genet.,* vol. 94, pp. 319-330, 1994.

[7] J. J. Bailey, A. S. Berson, A. Garson Jr, L. G. Horan, P. W. Macfarlane, D. W. Mortara and C. Zywietz, "Recommendations for standardization and specifications in automated electrocardiography: bandwidth and digital signal processing. A report for health professionals by an ad hoc writing group of the Committee on Electrocardiography and Cardiac Electrophysiology of the Council on Clinical Cardiology, American Heart Association," *Circulation,* vol. 81, pp. 730, 1990.